REVIEW

ADVANCED
MATERIALS

www.advmat.d

Check for
updates

Structural-Phase Catalytic Redox Reactions in Energy and Environmental Applications

Nasir Uddin, Huayang Zhang, Yaping Du,* Guohua Jia, Shaobin Wang,* and Zongyou Yin*

The structure–property engineering of phase-based materials for redox-reactive energy conversion and environmental decontamination nanosystems, which are crucial for achieving feasible and sustainable energy and environment treatment technology, is discussed. An exhaustive overview of redox reaction processes, including electrocatalysis, photocatalysis, and photoelectrocatalysis, is given. Through examples of applications of these redox reactions, how structural phase engineering (SPE) strategies can influence the catalytic activity, selectivity, and stability is constructively reviewed and discussed. As observed, to date, much progress has been made in SPE to improve catalytic redox reactions. However, a number of highly intriguing, unresolved issues remain to be discussed, including solar photon-to-exciton conversion efficiency, exciton dissociation into active reductive/oxidative electrons/holes, dual- and multiphase junctions, selective adsorption/desorption, performance stability, sustainability, etc. To conclude, key challenges and prospects with SPE-assisted redox reaction systems are highlighted, where further development for the advanced engineering of phase-based materials will accelerate the sustainable (active, reliable, and scalable) production of valuable chemicals and energy, as well as facilitate environmental treatment.

1. Introduction

Materials' properties are dependent on their chemical stoichiometry. However, the performance of materials is significantly related to their crystalline structure. Nano-to-atomic structural phase engineering (SPE) is emerging as a new research interest in the development of new function-oriented phase materials for energy and environmental applications. Concurrently, pressing global energy and environmental issues have driven the scientific community to identify active, reliable and scalable energy technologies that produce minimal environmental contamination. Beyond fossil fuel-based energy technologies, which have environmental issues, redox-reaction-based energy conversion from water splitting and carbon dioxide reduction will play a significant role in sustainable energy and clean environments. With both academic and industrial interests in redox reactions for energy and environmental technologies, it is crucial that ideal catalysts for target redox reactions have superior sustainability, selectivity, reactivity, and endurability.

SPE is becoming a well-known approach for tuning and architecting the physical and chemical properties of materials of interest at the atomic level.[1,2] As efforts have continued in materials science fields, the studies of SPE have shown increasing prospects in the hope of capitalizing on the innate catalytic activities of materials due to changes in the electronic configuration. We have known for a long time that there are many compounds that show various phase(s) based on structural differences and are especially promising in terms of increasing their activity and efficiency for particular systems of interest.[1,3] The variation in crystal structure is known as polymorphism/phases. The different phases give these materials extra flexibility in tuning their functional properties with respect to their size, shape, and composition.[4] By doing so, one can design a material with improved electronic, optoelectronic, and catalytic properties.[5] Much of that role is likely to be filled by SPE techniques, which could help potentially realize improved electrocatalytic,[6] photoelectrocatalytic,[7,8] photocatalytic,[8,9] and environmental degradation[10] performance in the context of desired products. Additionally, SPE techniques appear to have facilitated a much more fundamental understanding, especially in energy conversion, from

N. Uddin, Dr. Z. Yin
Research School of Chemistry
Australian National University
Canberra, ACT 2601, Australia
E-mail: zongyou.yin@anu.edu.au
Dr. H. Zhang, Prof. S. Wang
School of Chemical Engineering
The University of Adelaide
Adelaide, SA 5005, Australia
E-mail: shaobin.wang@adelaide.edu.au
Prof. Y. Du
School of Materials Science and Engineering
National Institute for Advanced Materials
Center for Rare Earth and Inorganic Functional Materials
Nankai University
Tianjin 300350, China
E-mail: ypdu@nankai.edu.cn
Dr. G. Jia
Curtin Institute of Functional Molecules and Interfaces
School of Molecular and Life Sciences
Curtin University
Perth, WA 6845, Australia

The ORCID identification number(s) for the author(s) of this article can be found under https://doi.org/10.1002/adma.201905739.

water splitting to carbon dioxide reduction to environmental pollutant treatments. Regarding these energy conversion processes, a number of redox reactions such as electrocatalysis-based hydrogen evolution reactions (EC-HERs), oxygen reduction reactions (EC-ORRs), oxygen evolution reactions (EC-OERs), and overall water-splitting reactions (EC-OWS); photocatalysis-based HER (PC-HER) and overall water splitting reactions (PC-OWS); photoelectrocatalytic overall water splitting (PEC-OWS); and electrocatalytic/photocatalytic CO_2 reduction reactions (EC/PC-CRRs) have been observed for many years.[11,12]

Apart from energy conversion and storage, SPE holds important applications in environmental remediation to realize a sustainable future.[13] Removing persistent organic pollutants in wastewater, which has posed a serious threat to the well-being of humankind and wildlife, serves as a primary branch of environmental science.[14] Considering the diverse features of contaminants, various treatment technologies have been explored, such as incineration, chemical oxidation, adsorption, and bioenvironmental processes.[15] There are limited reports about optimizing the efficiency of these kinds of treatment methods through phase engineering. Alternatively, most organic pollutants can be removed via a unique class of oxygenolysis techniques known as advanced oxidation processes (AOPs).[16] Based on the driving force for the production of ROS (reactive oxygen species) during the above processes, AOPs can be divided into the following categories: photochemical AOPs (PC-AOPs), electrochemical AOPs (EC-AOPs), photoelectrochemical AOPs (PEC-AOPs) and Fenton-like AOPs (FAOPs). All of these AOP techniques constitute encouraging, practical and environmentally friendly means to remove persistent organic pollutants from water.

Herein, we aim to review the SPE of materials that are likely to be involved in redox reactions, including EC-HER, EC-ORR, EC-OER, EC-OWS, PC-HER, PC-OWS, PEC-OWS, PC-CRR, EC-AOPs, PC-AOPs, PEC-AOPs, FAOPs, etc., and how these materials perform in terms of redox reactivity, selectivity, and stability under the effects of single or multiple factors, including crystallization, defects, bandgaps, excitation photons, neutral excitons, charge carriers (e^-/h^+), carrier mobility, interfacial band alignment, redox species, redox potential, etc. To improve the redox reaction dynamics, phase-based materials have been employed; however, the synergistic relationship between SPE materials and redox reactivity remains elusive. A systematic and in-depth understanding is needed to fully exploit the advantages of SPE for redox reactions to influence the overall efficiency of energy processes. Additionally, such understanding would also be beneficial in the development of highly active catalytic nanomaterials for redox reactions such as the nitrogen reduction reaction (NRR) because they have the potential to produce value-added chemicals and fuels in a sustainable manner. SPE offers a versatile and efficient way to improve catalytic materials with facile characteristics, representing the linchpin for modern energy technologies.

Md Nasir Uddin is a Ph.D. student at Australian National University. He obtained his B.S. in chemical engineering from ShahJalal University of Science and Technology, Sylhet, Bangladesh, and he obtained his M.S. in the same subject from University of New Mexico, USA. His research interests focus on the development of new 2D materials for electrocatalysis and photocatalysis in hydrogen and CO_2 reduction for fuel production.

Shaobin Wang obtained his B.Sc. and M.Sc. from Peking University (China) and his Ph.D. from the University of Queensland (Australia). He was previously a John Curtin Distinguished Professor in the Department of Chemical Engineering of Curtin University and is now a professor in the School of Chemical Engineering and Advanced Materials, University of Adelaide. His research interests focus on synthesis and application of nanomaterials for carbon dioxide utilization, energy conversion, and environmental remediation.
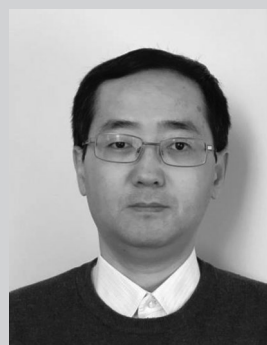
Zongyou Yin obtained his B.S. and M.S. degrees at Jilin University in China, and completed his Ph.D. at Nanyang Technological University (NTU) in Singapore in 2008. He then started his postdoc career at NTU/Singapore, IMRE/Singapore, followed by MIT and then Harvard University. He started his own Research Group at Australian National University (ANU) in 2017. His group's research is interdisciplinary, encompassing chemistry and physics of nano-to-atomic materials, the fundamental relationships among materials–structures–devices, and synergistic integration of multifunctions for sustainable energy and wearable applications.

2. SPE for Redox Processes

The occurrence of redox reactions during electrocatalytic, photocatalytic, photo-electrocatalytic, and environmental treatment processes is obvious, and these processes are of great importance. Depending on the chosen processes and experimental conditions, a number of redox reactions such as EC-HER, EC-ORR, EC-OER, EC-OWS, PC-HER, PC-OWS, PEC-OWS, PC-CRR, EC-AOPs, PC-AOPs, PEC-AOPs, and FAOPs have been developed, and these reactions have become the central subjects

of interest, particularly when evaluating the effectiveness of these processes. Of these reactions, EC-HER and EC-OER have received much attention in recent years with respect to energy processes. Limitations associated with EC-HER and EC-OER are sluggish kinetics and overall energy loss phenomena, thereby influencing the overall efficiency of these processes.[17,18] The combination of these two half reactions leads to the EC-OWS reaction, another highly energy-intensive process that has recently been on the front line of energy conversion-related discussions.[19] In the backwards direction, these two half reactions are often known as EC-HOR and EC-ORR since the overall reaction happens in close proximity on catalytic surfaces and/or interfaces; however, consideration should be given to the nature and selectivity of the reaction.[20] In addition to these two half reactions, PC-CRR is recognized to be a more promising and fascinating pathway in producing value-added chemical compounds because the process mimics the natural photosynthesis process. Undoubtedly, energy conversion from environmental pollutants such as CO_2 in the presence of light not only provides an extra benefit to that photocatalytic process but also reduces the dependence on fossil fuels, which is a major benefit in achieving effective energy-producing processes. Indeed, PC-CRR for manufacturing fuels, including methane, methanol, ethanol, and so on, has been studied for many years, and remarkable advancements have allowed them to be investigated further, even though the process itself involves complex multielectron reduction pathways. Unlike energy processes, environmental treatment has employed AOPs as water treatment processes conducted under mild conditions (room temperature and standard pressure) and based on the in situ formation of a series of highly ROS at an adequate concentration to efficiently remove contaminants.[21] AOPs over phase materials have been gaining interest very recently, while significant advancements in this field are yet to be found.

From a surface reactivity perspective, all of these redox reactions suffer from low efficiency because of the dynamics of the reactions and the synergistic interplay at the catalyst surface. In electrocatalytic processes, for example, the EC-HER is highly sensitive to the catalytic surface in basic environments, but its insensitivity toward the catalytic surface in acidic media is not easily understandable.[17] Additionally, the EC-OER faces overpotential issues and is insufficient in alleviating the energy loss for that process. In parallel with these unsatisfying catalytic surface activities, the PC-CRR on the catalyst surface or interfaces is highly complex since such a process involves more reductive/oxidative electrons/holes, more intermediate redox species and hence more hydrogenation/oxygenation steps, in addition to the common generation-recombination issues from photoinduced electron–hole pairs for other redox processes. Regardless, previous studies have indicated that the process performance can be improved by tuning the structure of the catalysts, which inherently serves as the source of catalytic active sites for reactant molecules.[22] Degradation of major pollutants from water is a key research topic in phase materials, while an understanding of how phase engineering affects the activity of catalysts for pollutant degradation is still complicated. Specifically, the dynamics of ROS activation occurring at the solid/liquid interface of various phases is unclear. To achieve highly active and long-lived catalysts, one can consider

that structural engineering at the atomic scale could open new vistas in attaining high performance and efficiency because such phase engineering approaches not only change the electronic structure but also impart improved physical, optoelectronic and, hence, catalytic properties.

Motivated by the abovementioned capabilities of these phase-based materials for redox energy conversion and environmental treatments, herein, we provide an overview of structural phase engineering at nano-to-atomic-scale regimes and how this SPE could influence the respective energy conversion processes. Readers should note that we do not summarize here many other excellent published articles, simply because of our scope and purpose here.[23,24] In line with this, we divide our review into a number of sections, where a comprehensive overview of phase materials and their activity is covered in Section 2, the SPE of electrochemical redox reactions is covered in Section 3.1, the photocatalysis and photoelectrocatalysis of water is highlighted in Section 3.2, the photocatalysis of CO_2 is covered in Section 3.3 and environmental treatment is emphasized in Section 4. Finally, we speculate some key gaps that need to be investigated further to improve the catalytic efficiency for energy conversion and environmental treatment processes.

2.1. Library for Various Types of Structural Phases

There are many materials in nature that have more than one crystalline structure, known as polymorphism/phases. Phase transition can be caused by different synthetic methods: ion intercalation,[25] doping/alloying,[26] thermal activation,[27] strain engineering,[28] defect engineering,[29] electrostatic gating,[30] charging,[31] and pressure-induced treatment.[32] Each of these techniques has its own merits and potential in changing the phase from one to another. Nevertheless, to date, the transition metal dichalcogenides (TMDs), noble metals (e.g., Pt, Rh, Ag, Au, Ir, and Ru), SnS_2, SnS, GaAs, and InAs, have been reported to exhibit different phases.[33,34] Generally, most of the pure metals in the periodic table may adopt one of the three possible structures: fcc, hcp, or bcc structures. With increasing atomic number in the transition metal series, the elements show the structural sequence of hcp → bcc → hcp → fcc.[35] This conclusion is supported by the relative stability of these phases in metals, which is fundamentally determined by the total energy of these phases. When the structure of the metals is changed, the degree of orbital overlap between d orbitals is also changed, which actually controls the electronic band structure, density of states (DOS) shape, and total energy of the metals, and such properties also differ for different phases.[35] It is important to keep in mind that the phase transition from a stable bulk phase to another is highly dependent on the temperature–pressure relationship for the corresponding reactions. It has been reported that several metals such as Fe, Au, Ag, and Ru can show phases different from their stable bulk phase. For example, Fe has ferromagnetic bcc structures, while its transformative phase is a nonmagnetic fcc structure. Bulk Ru has a hcp structure, while both bulk Au and Ag have an fcc structure.[35] Noble metals show hexagonal, tetragonal, and cubic phases; of these phases, the less thermodynamically stable phases exhibit unusual physical features and excellent catalytic properties.[36,37]

Other than the above categories, the phases of NbSe$_2$, TaSe$_2$, TaS$_2$, and TiS$_2$ are also highlighted; those are prone to show either the 2H or 1T phase[33] while ReS$_2$ shows a distorted 1T phase.[38] TMDs are a paradigm of 2H (hexagonal), 1H (trigonal prismatic), 1T (octahedral), 1T′ (monoclinic), T$_d$ (orthorhombic) and 3R (rhombohedral) phases[3] while SnS$_2$ and SnS reveal cubic, trigonal, hexagonal, and orthorhombic structures along with phase-dependent electronic band structures and dopant types.[33] TiO$_2$ is one of the most frequently studied photoactive materials and possesses three polymorphs, anatase, rutile, and brookite, with different electronic band structures.[39] Another oxide material, BiVO$_4$, shows monoclinic and tetragonal phases with differences in lattice structures,[40] while CdS can present cubic and hexagonal phases.[41] TMD materials are well-studied materials regarding their ability to display different phases; among them, MoS$_2$ and WS$_2$ are two of the most well-known materials, while consideration has been equally given to other TMD materials including MoSe$_2$, MoTe$_2$, WTe$_2$, WSe$_2$, ReS$_2$, Pd$_2$Se$_3$, NbS$_2$, etc., which have emerged as a new class of layered materials for photocatalytic and electrochemical reactions.[42–44] Since there are many phase materials, each phase can play a different role in the respective reactions. Therefore, we do not cover all possible phases for all elements here inclusively; rather, we present a library of phase materials where at least one phase is examined in any of the above redox reactions. To present an overview to the reader, we have tried to tabulate the different crystal phase materials, as shown in **Figure 1**, which we believe is up to date, and no report like this has been published yet.

2.2. Catalytic Activities Induced by SPE

Many materials have different polymorphs or phases in nature. The variation in phases for a given material arises from the change in electronic structure, which is also the primary reason for the different performance of each phase. Taking MoS$_2$ as an example, it shows three different phases, where the 1T phase is believed to be more conductive for hydrogen production than its 2H phase.[50] Chou and co-workers[51] have demonstrated that for the HER system, the 1T′-MoS$_2$ phase is more active than the 2H phase because the active sites are spread over both edges and basal planes for the former, while the distribution of active sites is only on the edges for the latter phase. Another example in this regard is TiO$_2$, which has anatase, rutile and brookite phases. Among these phases, the brookite phase is reported to provide the highest efficiency in terms of product formation during PC-CRR.[52] This observation verifies the importance of different phases on the reactions as well as on the process efficiency. To achieve increased activity over catalytic materials, it is therefore crucial to design and architect such phases structurally at the atomic scale.

Working with phase engineering involves taking advantage of innate properties for the desired processes. Du and co-workers[53] have pointed out that photocatalytic hydrogen evolution under visible-light irradiation could increase by a factor of 35 with an optimized 1T-MoS$_2$/CdS NR hybrid system compared with the pure CdS NR system. Such an improvement was attributed to the variation of the 1T-MoS$_2$ nanosheets. In parallel, Enyashin and co-workers[54] have fabricated the 1T-MoS$_2$

phase within WS$_2$ nanotubes along with rhenium (Re) doping, leading to stabilization of the 1T phase more profoundly than that of alkali intercalation into the lattice of the compound. Indeed, alkali intercalation has deleterious effects on phase transition since the transferred electrons from alkali metals could possibly enhance the electron density of the transition metal d-orbital, leading to destabilization of the 2H phase and its conversion to either the metallic 1T or distorted 1T′ phase.[55]

The metallic 1T/1T′ phase displays superior HER activity compared to that of the 2H phase, while the thermodynamically driven reverse phase transition into the 2H phase causes nondurability during HER. To further understand how durability can increase the HER performance, Liu and co-workers[56] have synthesized the 1T′ phase mixed with 2H-WS$_2$ phase (1T′-D WS$_2$) and pure 2H-WS$_2$ phase via a facile and effective one-pot colloidal method. The HER activity is far superior for 1T′-D WS$_2$ samples compared to 2H-WS$_2$ samples, showing an overpotential of 200 mV at 10 mA cm^{-2} along with a Tafel slope of 50.4 mV dec^{-1}. In acidic medium, the stability test indicates that the endurance half-life is ≈46 d under a constant overpotential of 0.3 V at 41 mA cm^{-2}, and vigorous erosion arises from continuous hydrogen bubbling, which put excess capillary stresses on the atomic sheets.

Of the few reports establishing that the functional characteristics of noble metal nanostructures can also be tuned through variation in their crystal phase, shape, composition and size, 4H-phase Ag materials were shown to have 100-fold higher in-plane resistivity and improved visible-light absorption capacity compared to those of fcc (face-centered cubic)-phase Ag films.[57] Through phase conversion from fcc to fct (face-centered tetragonal), FePt nanoparticles display a transitional phenomenon from superparamagnetic to strongly ferromagnetic.[58] In a similar approach, by using solution-phase epitaxial growth under ambient conditions, unusual 4H hexagonal Ir, Rh, Os, Ru, and Cu nanostructures were coupled with 4H Au nanoribbons (NRBs), and the 4H Au NRBs transformed from 4H to fcc phase.[59,60]

Gao and co-workers[61] have studied the phase transition of single-layer MoS$_2$ from bulk 2H to metallic 1T and then to 1T′ phases and showed how this transition impacts HER activity from the viewpoint of density functional theory. The phase transition starts by the transfer of S atoms from one pyramidal position to the other pyramidal position of the unit cell. **Figure 2** depicts the phase transition of 2H to 1T under charge states from 0e$^-$ to 4e$^-$ in each MoS$_2$ unit. The relative energies of the neutral state (0.8 eV) and the 1e$^-$ charge state (0.31 eV) decrease from positive to negative for the 2e$^-$ (−0.05 eV), 3e$^-$ (−0.10 eV), and 4e$^-$ (−0.3 eV) charge states. This effect implies that charge injection could stabilize the 1T-MoS$_2$ phase, especially in the case where more than 1e$^-$ is involved, and then, 1T-MoS$_2$ becomes is more stable than its bulk counterparts. The phase transformation energy barrier also decreases to 1.11, 0.71, 0.54, and 0.27 eV in the 1e$^-$, 2e$^-$, 3e$^-$, and 4e$^-$ charge states, respectively, from 1.59 eV in the neutral state. More precisely, the negative charge easily induces the conversion of 2H-MoS$_2$ into 1T-MoS$_2$. The HER involves two major reactions, namely, the Volmer and Heyrovsky reactions (we will discuss them in the next section). Based on the Gibbs free energy calculations shown in Figure 2, it is emphasized that 1T′-MoS$_2$ shows superior catalytic activity.
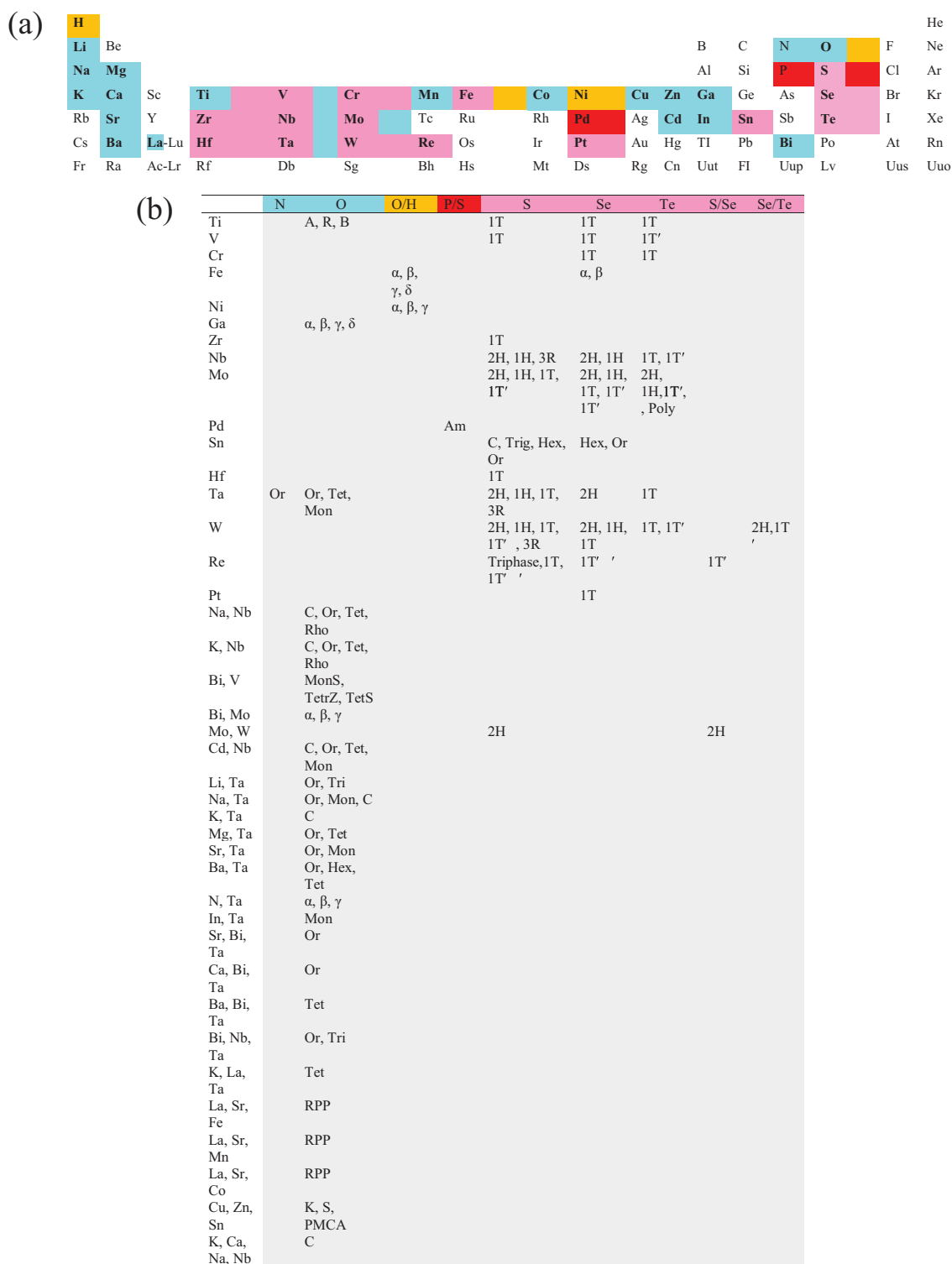
Figure 1. Representation of phase-materials library for redox reactions in energy conversion. a) The elements (colored) in the periodic table create phases when they coordinate by the oxygen, nitrogen, hydrogen, chalcogen, and the based dual elements. The chalcogen and oxygen make most of the significant SPE materials for redox reactions while others also show potential promise as well. b) Summary of SPE materials for redox reactions. Many materials have different polymorphs/phases where one phase works differently with respect to others. Note: anatase (A), rutile (R), brookite (B), amorphous (Am), polymorphic (Poly), cubic (C), trigonal (Trig), hexagonal (Hex), orthorhombic (Or), tetragonal (Tet), rhombohedral (Rho), monoclinic scheelite (MonS), tetragonal zircon (TetZ), tetragonal Scheelite (TetS), monoclinic (Mon), triclinic (Tri), Ruddlesden–Popper phases (RPP), kesterite (K), stannite (S), and primitive mixed CuAu (PMCA). Data for (b) have been collected from published articles to date.[2,45–49] and we include the phase(s) for the periodic elements that show at least one phase for the above redox reactions.
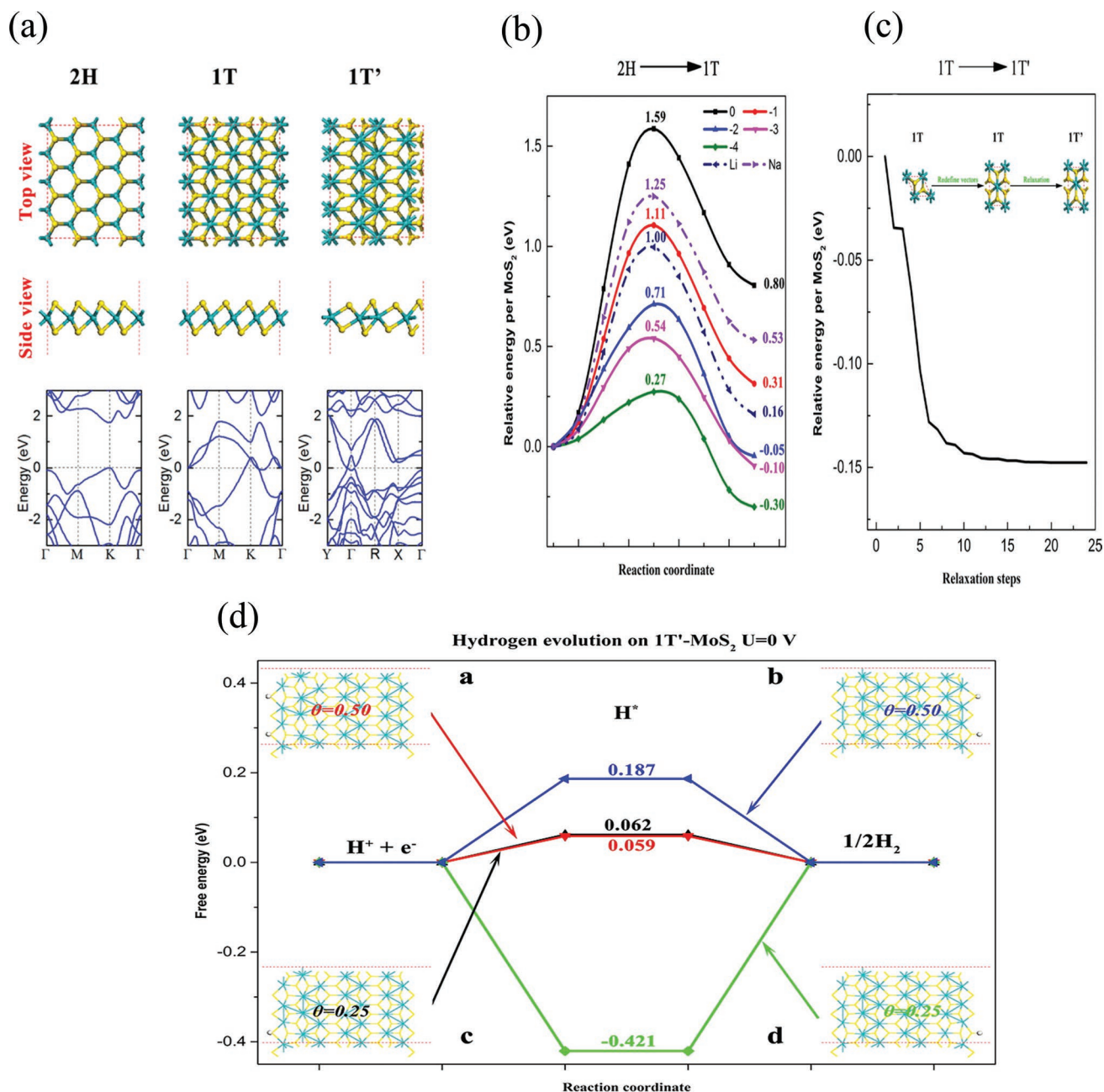
ADVANCED
SCIENCE NEWS
www.advancedsciencenews.com

ADVANCED
MATERIALS
www.advmat.de

Figure 2. a) Schematic of top view and side view of 2H, 1T and 1T′ MoS₂ and their band profiles. b) Minimum-energy pathways of the phase transition from 2H to 1T in different charge states or with ion intercalated. All the energies are relative to the total energy of 2H-MoS₂ in corresponding charge states or with corresponding ion intercalated. c) Spontaneous atom relaxation from 1T to new 1T′ phase. d) Free energy diagram of HER processing over 1T′-MoS₂ under different coverage at equilibrium potential. a–d) Adapted with permission.[61] Copyright 2015, American Chemical Society.

It is suggested that SPE influences the reaction activity, performance, and efficiency of organic pollutant degradation. Metal oxides with low OER activity, such as tin dioxide (SnO₂) and lead dioxide (PbO₂), are generally suited to act as effective catalysts or substrates for electrochemical pollution oxidation, where the OER side reaction is suppressed. Many techniques, such as anodic or cathodic deposition, have been implemented to obtain different phases of metal oxides.[62] Abaci and co-workers have investigated the performance of different phases of PbO₂ toward electrochemical phenol

degradation.[63] By changing the precursor concentration and deposition current density, films of pure α-PbO₂ and β-PbO₂ were obtained. Consequently, the higher conductivity, superior stability, and unique porous structure of β-PbO₂ enabled higher HO• flux and faster oxygen-atom transfer, resulting in better performance than that of α-PbO₂ in phenol degradation. The feasibility of different phases in nontoxic metal oxides (e.g., MnO₂, WO₃) has also been explored for environmental electrocatalysis. MnO₂, which is abundantly available, has been broadly used as an electrode material for

electrochemical applications. Devaraj and Munichandraiah[64] investigated the specific electrochemical capacitance of three MnO_2 phases, which followed the order α-MnO_2 > γ-MnO_2 > β-MnO_2, suggesting that they possess different electrocatalytic activities.

3. SPE for Energy Conversion and Environmental Treatment

Energy conversion processes such as electrocatalysis, photocatalysis, and photoelectrocatalysis have been studied for many years to identify reliable and scalable energy carriers such as hydrogen or other valuable chemicals. Neither a single process nor their combination can produce industrial grade energy fuels yet, even though much remarkable advancement and progress over these processes has been reported.[23] These energy processes need to be translated into productive means by utilizing less expensive and more environmentally benign resources. One of the characteristics of these energy processes is the involvement of either oxidation or reduction reactions or a combination of multielectron processes. These redox reactions are apparently kinetically slow reactions that require much energy input to be driven.[28] Historically, in such a case, we have seen that materials from the noble metal group are likely able to decrease the energy barrier and hence accelerate the redox reaction in the direction of the target products.[23] Owing to their high cost and scarcity, however, it is not viable to use these metals in large-scale applications. Therefore, there is an opportunity to use other materials, but to be competitive in those redox reactions, they should possess an extended electronic structure and optoelectronic properties. As we have shown in the previous section, there are a number of such materials that possess alternating lattice structures and are thus able to form various atomic arrangements in the nanoregime, that is, phases or polymorphs.

Very recently, many research groups have examined different phase-based materials in energy production using redox reactions, such as EC-HER, EC-OER, EC-OWS, and PC-CRR. Taking orthorhombic and cubic phases of $CoSe_2$ electrocatalysts as an example, it was shown that the cubic phase outperformed the orthorhombic phase because of the increased electron mobility, promoting the intrinsic catalytic activity of that phase for HER processes.[65] Another example is the 1T-MoS_2 phase materials, which are believed to possess reactive sites at both the basal plane and edges, making them excellent candidates compared to other phases (2H-MoS_2) in HER systems. The presence of a large number of active sites can extend the electron mobility to lower the energy barrier for the redox HER system. Despite the increasingly prevalent studies of single phases for electrocatalytic HER systems, the construction of multiple phases such as 1T/2H-MoS_2 could be more effective in achieving higher electrocatalytic performance. Among many reasons for such improvement in electrocatalysis, interfacial charge transfer can increase the electron mobility faster because of the intimate contact between the materials.

The application of phase materials in both photocatalytic and photo-electrocatalytic processes has been reported over the decades, and both of them provide great advantages in the context of using abundant, less expensive, and environmentally friendly resources such as solar energy while producing a substantial volume of end products. However, both processes suffer from complications arising from reaction kinetics and dynamics.[66,67] The overall water-splitting process with the aid of light illumination is considered one of the potential approaches in evaluating both HER and OER processes simultaneously. For example, many research groups employed phase junctions of α-Ga_2O_3 and β-Ga_2O_3 and found that the photocatalytic performance was higher than that for other phase junctions such as γ-Ga_2O_3 and β-Ga_2O_3. Another classic photocatalytic process is the reduction of CO_2 into valuable chemical fuels, which has been scrutinized over different crystal phase materials, including TiO_2. TiO_2 has three distinguishing phases, anatase, rutile, and brookite, which are believed to be effective for different redox reactions.[68] Nevertheless, we can say that in the search of scalable and reproduceable energy processes, it would be very fascinating to use different phase materials since they have alternating electronic band structures.

There are limited reports about optimizing the efficiency of pollutant treatment processes through phase engineering. For example, Cao et al. introduced a concept of structural design for the synthesis of hierarchical core–shell MnO_2 ellipsoids comprising multiple phases.[69] The porous γ-MnO_2 core coupled with the active edges exposed on the irregularly shaped, upright-standing nanoflakes of the α-MnO_2 shell resulted in a high adsorption capacity for methylene blue. Karunakaran et al.[10] quantified and compared the antibacterial activity of functionalized 2H- and 1T-MoS_2. 2H-MoS_2 demonstrated better antibacterial activity than did 1T-MoS_2. Moreover, the semiconducting 2H-MoS_2 possess improved ROS production. In addition, the unique synergistic effect of the 2H phase and the functionalized ligands was responsible for the membrane damage and hence resulted in enhanced activity. Although these traditional methods show robust efficiency, they cannot degrade pollutants selectively or can cause secondary pollution if the processing conditions are not well controlled.[70]

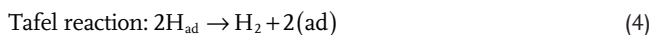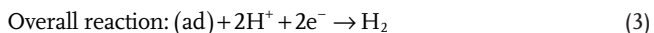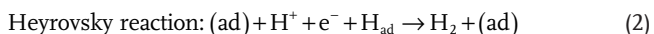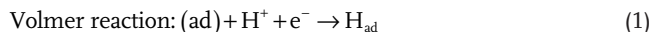### 3.1. SPE for Electrocatalytic Water Splitting

Electrocatalytic water splitting has been thought to be a viable pathway for producing hydrogen as well as oxygen. There is a growing interest in developing promising phase-based electrocatalytic materials for cost-effective water-splitting processes, and the research in this field has been intensified over the last decades. One of the benefits of using SPE in water splitting is to regulate the adsorption energies of atomic hydrogen or OER intermediates such as OH*, O*, and OOH* onto the surface of the phase materials, thereby improving HER or OER activity.[23] A possible reason is the alteration in the electronic structure of the phases, which play a key role in providing the reactive sites for the reactant molecules. In the following section, we will cover various phase materials in a water-splitting system that are believed to be effective and applicable for the respective redox reactions. In addition, we will speculate more about structural phase-based engineered materials for electrocatalytically driven HER, while at the end of this section, we summarize (**Table 1**) some recent literature results in that research arena.

**ADVANCED
SCIENCE NEWS**

www.advancedsciencenews.com

**ADVANCED
MATERIALS**

www.advmat.de

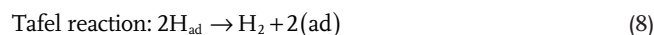**Table 1.** Summary of Phase based electrocatalytic materials for HER system.

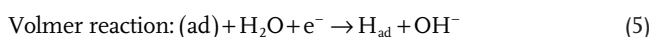| Electrocatalysts	Synthesis method	Reaction agent	Overpotential [mV@10 mA cm^{-2}]	Tafel slope [mV dec^{-1}]	Refs.
1T–2H MoS$_2$ nanosheets	Graphene-oxide-assisted two-step hydrothermal method	0.5 M H$_2$SO$_4$	126	35	[95]
1T′-phase ReSe$_2$ and 1T′-phase ReSSe$_2$ nanodots	CVT and Li-intercalation	0.5 M H$_2$SO$_4$	123 and 84	50.8 and 50.1	[96]
2D 1T-MoS$_2$ quantum dots	Electrochemical lithiation	0.5 M H$_2$SO$_4$	92	44	[97]
1T-MoS$_2$ hybrids	Hydrothermal method	0.5 M H$_2$SO$_4$	425	45	[98]
Na-intercalted/1T-MoS$_2$	n-butyl lithiation method	0.5 M H$_2$SO$_4$	183	45	[99]
1T-MoSe$_2$ nanosheets	Solvothermal	0.5 M H$_2$SO$_4$	179	78	[100]
1T-MoSSe nanodots; and 1T-MoS$_2$ nanodots	Ball milling and chemical lithium intercalation	0.5 M H$_2$SO$_4$	140 and 173	40 and 53	[101]
1T-MoSe$_2$ nanosheets	Hydrothermal	0.5 M H$_2$SO$_4$	152	52	[44]
1T-WS$_2$ nanosheets	Electrochemical exfoliation	0.5 M H$_2$SO$_4$		154	[102]
1T-MoSe$_2$/Mo core–shell 3D hierarchical nanoscrews	Plasma-assisted selenization	0.5 M H$_2$SO$_4$	166	34.7	[103]
Ultrasmall 2H MoS$_2$ nanoparticles	Ultrahigh vacuum method	0.5 M H$_2$SO$_4$	200	55–60	[104]
1T-MoS$_2$ flower like nanostructure	n-butyllithium intercalation	0.5 M H$_2$SO$_4$	187	43	[77]
1T′-WS$_2$ nanosheets	n-butyllithium intercalation	0.5 M H$_2$SO$_4$	80–100	30–60	[12]
1T-MoS$_2$ nanosheets	n-butyllithium intercalation	0.5 M H$_2$SO$_4$	187	40	
1T′-ReS$_2$ nanosheets	Lithium intercalation	0.5 M H$_2$SO$_4$	100	75	[105]
1T–2H MoSe$_2$ nanosheets	Hydrothermal method	0.5 M H$_2$SO$_4$	152	52	[44]

3.1.1. SPE for Electrocatalytic HER (EC-HER)

Hydrogen production from electrochemical water splitting is considered an ideal ecofriendly approach.[17] HER occurs at an electrode on one side, while OER occurs on the other side. These distinctively different reactions have thermodynamic importance in optimizing the desired outcomes. However, the key contributions to HER come from an effective electrode that works as an electrocatalyst, which has the ability to convert a pair of protons and electrons into H$_2$. The classic HER involves multistep reactions including adsorption, reduction, and desorption processes. In acidic environments, the elementary steps and overall reaction pathways are as follows:[71]

$$\text{Volmer reaction: } (ad) + H^+ + e^- \rightarrow H_{ad} \tag{1}$$

$$\text{Heyrovsky reaction: } (ad) + H^+ + e^- + H_{ad} \rightarrow H_2 + (ad) \tag{2}$$

$$\text{Overall reaction: } (ad) + 2H^+ + 2e^- \rightarrow H_2 \tag{3}$$

$$\text{Tafel reaction: } 2H_{ad} \rightarrow H_2 + 2(ad) \tag{4}$$

For a basic environment, we can express them as:

$$\text{Volmer reaction: } (ad) + H_2O + e^- \rightarrow H_{ad} + OH^- \tag{5}$$

$$\text{Heyrovsky reaction: } (ad) + H_2O + e^- + H_{ad} \rightarrow H_2 + OH^- + (ad) \tag{6}$$

$$\text{Overall reaction: } (ad) + 2H_2O + 2e^- \rightarrow H_2 + 2OH^- \tag{7}$$

$$\text{Tafel reaction: } 2H_{ad} \rightarrow H_2 + 2(ad) \tag{8}$$
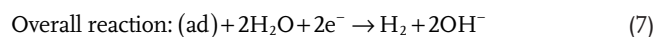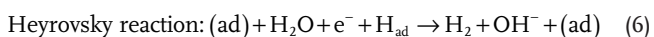
The Tafel slope for Volmer, Heyrovsky, and Tafel in both media would be 120, 40, and 30 mV dec^{-1}, respectively.

In an acidic environment, the adsorbed hydrogen comes from hydronium ions, while in an alkaline environment, it is related to water molecule dissociation. Regardless of the experimental conditions, this step is referred to as the Volmer step. The conjugation of the adsorbed hydrogen (H$_{ad}$) to form molecular hydrogen is realized through either a Heyrovsky or Tafel step. The performance of HER electrocatalysts is largely dependent on the inherent chemical and electronic properties of the electrode surface, and the performance evaluation of HER involves understanding the kinetics and reaction rates of these electrocatalysts. To obtain such information, one can use Tafel slopes, which are directly linked with reaction steps. Setting the rate-limiting rules, one should identify whether the reaction is controlled by the Volmer step (in this case, the hydrogen adsorption energy is too weak) or the Heyrovsky or Tafel step (the hydrogen adsorption energy is too strong). However, interpreting the HER performance based on that rate-limiting concept could lead to poor apparent activity, which therefore necessitates the use of a volcano plot to evaluate the true HER activity—a quantitative relationship between the thermodynamic overpotential and the free energy of hydrogen adsorption energy.[72,73] By using a volcano plot, it is easy to understand what an ideal catalyst would look like because at

ADVANCED
SCIENCE NEWS
www.advancedsciencenews.com

ADVANCED
MATERIALS
www.advmat.de

zero Gibbs free energy, it would give the highest exchange current density, that is, an ideal catalyst binds reaction intermediates neither too strongly nor too weakly. In determining HER activities, however, alkaline conditions are more complicated than those of acidic media because of the evolution of both H and OH species due to water dissociation processes.[74] Therefore, careful assessment is of significant importance for HER by considering the solution pH, solvation effects, electrode potential, and electric double-layer effects.[75] These identifying parameters help to evaluate the activity and performance of the catalysts for HER, though other parameter evaluations deserve to be investigated as well.

EC-HER on Single Phases: As a great way to increase the abundance of catalytic active sites and enhance the intrinsic activity for HER, SPE can reveal the true activity of either basal planes or exposed edge sites or their coupling contributions to HER under a systematic experimental setup. Once the preferential active sites have been exposed, the performance of the HER can be optimized. MoS_2, a classic example of a 2D material, shows phases 1T and 2H, among many others. Switching between the 2H and 1T phases of MoS_2 materials might seem counterintuitive in the design and fabrication of catalytically active materials because these phase structures are the key to their intrinsic properties. Let us take the 1T-MoS_2 phase as an example, which is expected to be 10^7-fold more conductive than the 2H phase

and more likely to show better performance in producing hydrogen.[50] The HER activity is found to be interlinked with the hydrogen adsorption free energy, which is much higher for the 2H-MoS_2 phase than for the 1T-MoS_2 phase and is also an illustration of the kinetic energy barrier for HER.[12] In the case of the 1T-MoS_2 phase, the energy needed for H to bind to the S sites is largely dependent on the quantity of H coverage.[76] Synthetic approaches, however, have a much more discrete effect in realizing the SPE strategy, involving the combination of preferred phase(s) with preferred nanostructures, which can lead to improved HER performance. With intercalation of lithium ions into the van der Waals gap of MoS_2, a phase transformation from the semiconducting 2H phase to the metallic 1T phase was observed, while a vertically aligned MoS_2 electrocatalytic nanofilm was believed to be the reason for the enhanced catalytic performance (**Figure 3**).[6] Lithium intercalation potential plays a vital role in expanding the van der Waals gap until exfoliation is complete, where the potential is driven from high to low in MoS_2 nanofilms.

SPE with chemical exfoliation in MoS_2 can convert the 2H phase to the 1T phase because the electrons move to the MoS_2 nanosheets from the alkali atoms, filling the lower-lying MoS_2 orbital to stabilize the 1T phase and destabilize the 2H phase.[77] Applied characterization techniques and electrochemical studies confirmed that the 1T-MoS_2 nanosheets showed
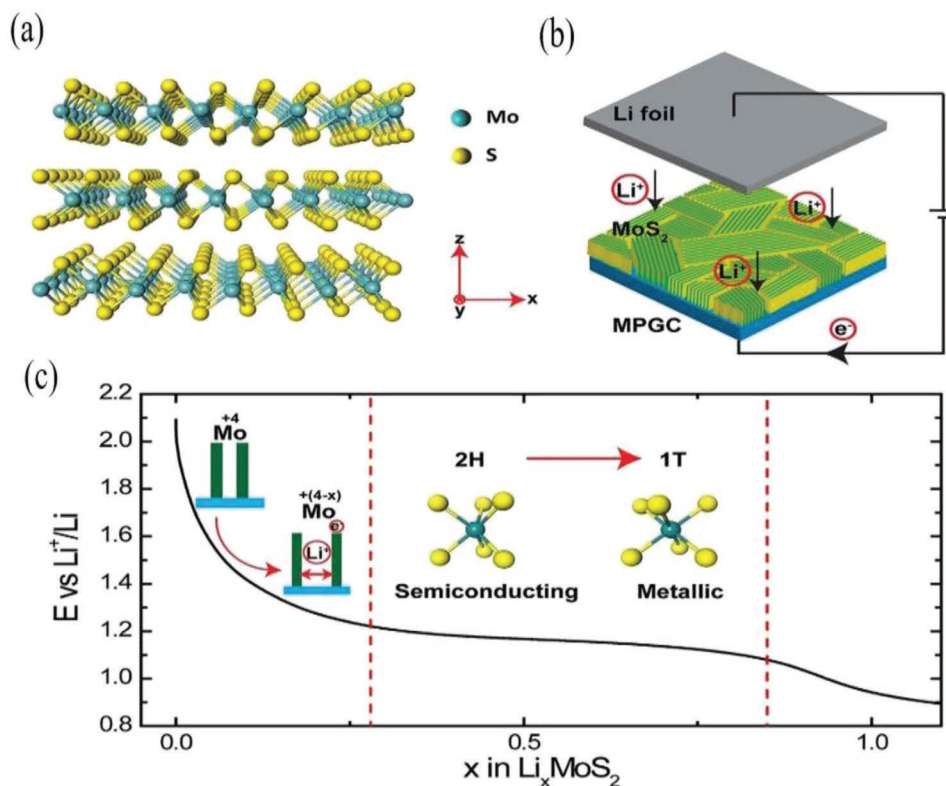

Figure 3. Representation of galvanostatic discharge curve of lithium intercalation on MoS_2 nanofilms. a) Structure of 2H MoS_2 phase. b) Battery testing system. The cathode is MoS_2 nanofilm with molecular layers perpendicular to the substrate, where the green and yellow colors represent the edge sites and the terrace sites, respectively. The anode is the Li foil. c) Galvanostatic discharge curve representing the lithiation process. Li intercalates into the van der Waals gaps of MoS_2 to donate electrons to the slabs and expand the layer spacing. The voltage monotonically drops to 1.2 V versus Li^+/Li to reach a Li content of 0.28, after which the system undergoes a 2H to 1T MoS_2 first-order phase transition. The atomic structure is changed from trigonal prismatic to octahedral, along with the electronic semiconducting to metallic transition. a–c) Adapted with permission.[6] Copyright 2013, National Academy of Sciences.

**ADVANCED
SCIENCE NEWS**

www.advancedsciencenews.com

**ADVANCED
MATERIALS**

www.advmat.de

facile electrode kinetics, improved electron transport, and an increased density of catalytic active sites, increasing both the intrinsic catalytic activity and overall catalytic performance. The estimated overpotential and Tafel slope were found to be −187 mV at 10 mA cm^{-2} and 43 mV dec^{-1}, respectively, with the as-prepared 1T-MoS$_2$ nanostructure, while the unexfoliated MoS$_2$ exhibited an overpotential of −320 mV at 10 mA cm^{-2} and a Tafel slope of 110 mV dec^{-1}. The authors argued that activating the basal plane of 1T-MoS$_2$ for inherent catalytic activity is needed more than creating active edge sites for the catalytic activity of 2H-MoS$_2$ because the basal plane has more exposed surface area. The volume of the 1T phase in MoS$_2$ is important here because the HER activity is related to the content of that phase.[78] Compared with chemical exfoliation in solution utilizing n-butyllithium, lithium borohydride exfoliation gives a high content of the 1T phase (80%), while the former results in a 50% content of the 1T phase. A low overpotential of 100 mV at 10 mA cm^{-2} and a small Tafel slope of 40 mV dec^{-1} were reported over the glassy carbon-supported 1T-MoS$_2$ phase. The authors also highlighted that the oxidation of edge sites of 2H-MoS$_2$ noticeably decreases the electrochemical activity, whereas the oxidation of 1T-MoS$_2$ does not lower the HER performance. This result implies that the phase transition from the 2H to the 1T phase could enhance the number of active sites on the basal plane along with the edge sites to potentially accelerate HER activity. This study infers that the catalytic active sites of 1T-MoS$_2$ could be found on both edge sites and the basal plane, which could be different in the case of the 2H-MoS$_2$ phase. The chemical exfoliation process, however, for transforming the phase and tuning the electronic structure is currently not the only way because there are more novel and facile methods currently being investigated.

Structurally, the 1T phase stacked in-plane on the 2H phase is known to have outstanding HER activity, though SPE of other active sites can be a prominent approach to enhance the HER performance. To this end, the vertical growth of the 1T phase on the 2H phase was reported to show higher electrochemical activity for HER.[79] The calculated Tafel slope of 42 mV dec^{-1} along with a relatively low overpotential of 116 mV at 10 mA cm^{-2} was reported. Here, the basal plane of MoS$_2$ is presumably catalytically inactive, whereas the exposed fractal-shaped single-layer MoS$_2$ can increase the electrocatalytic HER activity because it has a unique electronic structure and local stoichiometry, which enhances the edge-to-substrate ratio—a desired characteristic for improved HER performance. Additionally, d-band theory implies that the electron supply to the catalytic active sites increases due to the tensile strain in MoS$_2$, which thus boosts the electrocatalytic HER activity.[80] Likewise, Wan and co-workers[81] have prepared fractally shaped single-layer MoS$_2$ with a large tensile strain on fused silica via a chemical vapor deposition (CVD) route and reported that the as-synthesized MoS$_2$ has a large quantity of exposed edge sites, which is beneficial for superior HER activity compared with triangle-shaped MoS$_2$ on a SiO$_2$ substrate. A low overpotential of 185 mV at a current density of 10 mA cm^{-2}, a Tafel slope of 45 mV dec^{-1} and an exchange current density of 50.9 μA cm^{-2} was obtained with fractal-shaped single-layer MoS$_2$ electrocatalysts, which correlates to an edge-to-substrate ratio of ≈0.33 μm^{-1}. It is likely that the electron supply to the

catalytic active sites was rapid due to the large tensile strain. One disadvantage of this approach is that the formation of catalytically active edge sites is thermodynamically unfavorable compared to that for the basal plane. Being identical to 1T-MoS$_2$, the 1T-WS$_2$ nanosheets were predicted to have improved HER catalytic activity.[12] The 1T-WS$_2$ nanosheets can be synthesized with the aid of CVD-grown 2H-WS$_2$ nanoflakes by means of a microwave-assisted n-butyllithium intercalation method[12] or from commercial 2H-WS$_2$ particles. The concomitant transformation and exfoliation of the 2H-WS$_2$ phase into 1T-WS$_2$ nanosheets show improved electrical mass transport, facile electrode dynamics, and enhancement in catalytic active sites.[12] The different initial 2H-WS$_2$ samples used in these two studies could reasonably result in significant differences in terms of catalytic HER performance.[12] Compared with bulk WS$_2$, the CVD-assisted WS$_2$ nanoflakes exhibit a high density of sulfur vacancies, resulting in a higher performance for HER.

Theoretical analyses indicated that the sulfur defects and more exposed edge sites on the 1T-MoS$_2$ phase could enhance the electrocatalytic performance. Based on these ideas, Yin and co-workers[82] have prepared multiphasic MoS$_2$ that contains many sulfur defects and active sites and showed that both sulfur defects and exposed sites significantly increase the electron conductivity, thereby leading to high HER activity. Since sulfur vacancies are catalytically active, the authors could effectively fine-tune the hydrogen adsorption free energy and catalytic activity of MoS$_2$ by means of manipulating the proportion of sulfur vacancies and strain sites. In brief, they prepared mesoporous 1T-phase MoS$_2$ nanosheets (P-1T-MoS$_2$) with the aid of liquid ammonia lithiation to evaluate the effects of the crystal structure, edges, and S vacancies on the HER catalytic activity. For concise evaluation of the calculated values, four other samples were chosen, namely, mesoporous 2H-phase MoS$_2$ (P-2H-MoS$_2$), mesoporous 2H-phase MoS$_2$ after sulfur compensation (P-2H-MoS$_2$+S), 1T-phase MoS$_2$ (1T-MoS$_2$), and 2H-phase MoS$_2$ (2H-MoS$_2$) (**Figure 4**). The key findings include: a) the superior HER catalytic activity of 1T-MoS$_2$ and P-1T-MoS$_2$ compared with that of the 2H-phase material, and b) the enhanced catalytic performance of P-1T-MoS$_2$ and P-2H-MoS$_2$ compared to that of the bulk materials because of the abundance of edge-terminated features in those samples, ensuring isotropic electron transport. The P-1T-MoS$_2$ sample has more edges than the conventional 1T-MoS$_2$ sample, exhibiting better performance, and the S vacancies have a significant effect on HER catalysis, as evidenced by the low overpotential of P-2H-MoS$_2$+S compared to that of P-2H-MoS$_2$. In addition, the characterization studies of those samples reveal that the synergistic effects of crystal phase, edges, and S vacancies result in high intrinsic HER activity over porous 1T-MoS$_2$ nanosheets, with an overpotential of 153 mV at 10 mA cm^{-2} and a Tafel slope of 43 mV dec^{-1}. Similarly, the introduction of cracks in the 1T-MoS$_2$ nanostructure is an alternative route to obtain an optimal number of internal active sites, which is supposed to be necessary to achieve high performance in HER as well as high stability.[83] To answer stability questions regarding the 1T phase, qualitative and quantitative insights into the nanostructure array are crucial, and in this sense, Sun and co-workers[22] have experimentally investigated the structural evolution of different amounts of 1T phase, for example, 16.4%, 69.4%, and 90.2% of 1T phase, using a bottom-up hydrothermal approach with urea as a starting material. The authors pointed
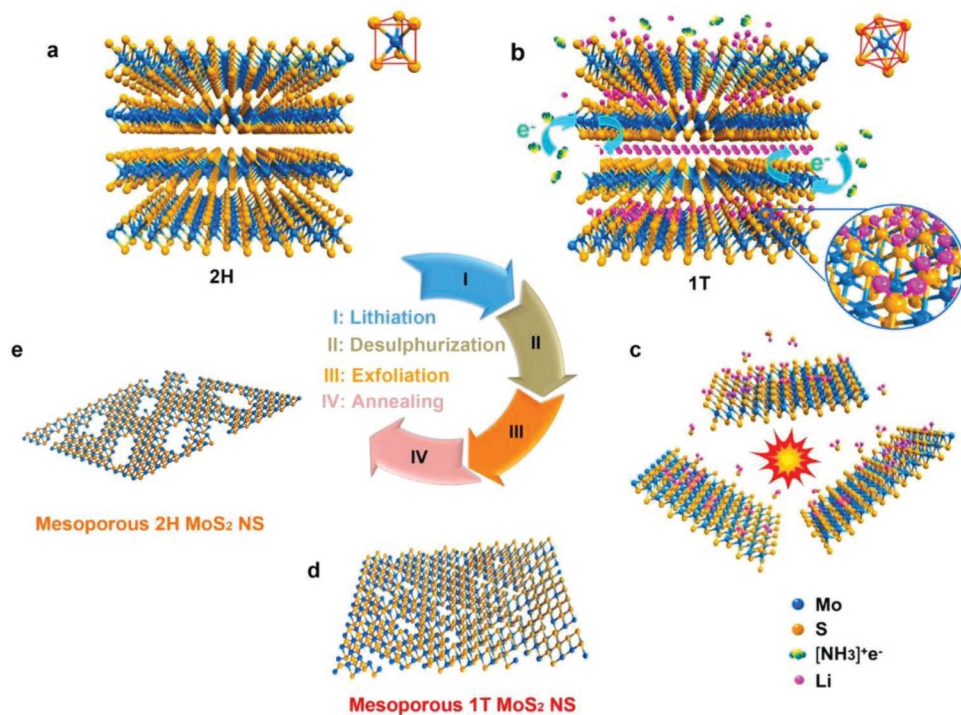
Figure 4. Schematic representation of the synthesized mesoporous 1T phase MoS_2 nanosheets (P-1T-MoS_2) (d) from bulk MoS_2 (a) by a liquid ammonium assisted lithiation (LAAL) process, including lithiation, desulfurization, and exfoliation (steps I, II, and III). Mesoporous 2H phase MoS_2 nanosheets (P-2H-MoS_2) (e) can be obtained by a simple thermal annealing process from P-1T-MoS_2 (step IV) formation of charged 1T phase MoS_2 due to Li^+ (lithium ion) intercalation between the interlayers (b), and formation of neutral MoS_2 materials with intercalated metallic Li (c). Adapted with permission.[82] Copyright 2016, American Chemical Society.

out that the growth of 1T-phase MoS_2 depends on the ammonia-assisted assembly, recrystallization, and stabilization processes. An overpotential of 76 mV at 10 mA cm^{-2} was noted for hydrogen evolution in acidic media, and the catalyst showed durability up to 15 h. Unsurprisingly, the unique array structure and high-purity 1T-phase MoS_2 nanosheets were believed to be the reasons for the electrocatalytic HER activity. However, phase engineering by means of hydrothermal methods remains less understood because of the introduction of guest molecules or ions that progressively affect the long-term stability of 1T-MoS_2. While making stable 1T-MoS_2 is the basic criterion for improved HER activity, the inclusion of small molecules or ions to engineer 1T-phase MoS_2 along with high purity and controlled electronic properties may be an alternative option.[22] Lai and co-workers[84] have synthesized a series of 1T′-phase $ReS_{2x}Se_{2(1-x)}$ ($x = 0–1$) nanodots to produce hydrogen from electrochemical water splitting in an acidic environment. Among the synthesized products, the 1T′-phase ReSSe nanodots show the best hydrogen evolution performance along with a Tafel slope of 50.1 mV dec^{-1} and a low overpotential of 84 mV at a current density of 10 mA cm^{-2}. The asymmetric sulfur vacancy in the highly asymmetric 1T′ crystal structure promotes the optimal hydrogen adsorption energy of active sites, which results in excellent hydrogen evolution activity and excellent long-term durability.

Theoretical and experimental studies have suggested that the natural semiconducting 2H phase could be electrocatalytically active since it has unsaturated X-edges and has almost zero Gibbs free energy for H adsorption.[85] Accordingly, such findings have become the motivation for the development of many

nanostructured electrocatalytic materials, in which the edge sites are intentionally exposed to promote improved HER electrocatalytic activity. By engineering and designing single- and/or few-layered 2D heterostructures, Najafi and co-workers[85] synthesized single- and/or few-layer $MoSe_2$ flakes over graphene or single-wall carbon nanotubes via a solution method that increases the number of electrocatalytic sites. To activate the basal plane of the 2D materials, the authors used thermally induced texturization by annealing the $MoSe_2$ flakes in a hydrogen environment, while a chemical bath with an organolithium compound could change the phase of $MoSe_2$ from 2H to 1T. A cathodic current density of 10 mA cm^{-2} at an overpotential of 100 mV, an exchange current density of 0.203 μA cm^{-2} and a Tafel slope of 63 mV dec^{-1} were reported for the $MoSe_2$ flakes and their electrode assembly for a given mass loading. However, a 4.8-fold enhancement of the exchange current density and a reduction in the Tafel slope of 54 mV dec^{-1} were observed for the as-engineered electrodes. The phase conversion of $MoSe_2$ flakes is attributed to enhanced electron conductivity and increased surface performance of the basal plane for atomic H binding, which may favor the Volmer reaction pathway to accelerate the subsequent Heyrovsky reaction.

Nevertheless, chemical exfoliation by means of lithium intercalation could induce a phase transition between the bulk 2H phase to the metallic 1T phase, which is very important for electron transport from the electrode to the active edges. Revealing such properties of TMD materials for enhanced electrocatalytic HER activity, Ambrosi and co-workers[86] have prepared

**ADVANCED
SCIENCE NEWS**

www.advancedsciencenews.com

**ADVANCED
MATERIALS**

www.advmat.de

1T-phase MoS_2, $MoSe_2$, WS_2, and WSe_2 nanosheets using a chemical exfoliation method and compared their hydrogen evolution rates with those of the corresponding 2H-phase materials. The authors showed that the HER activity and degree of exfoliation are dependent on various organolithium compounds utilized for intercalation; for instance, compared to methyllithium compounds, the tert-butyllithium and n-butyllithium have more capacity to provide better HER catalytic activity and degree of exfoliation. However, an overpotential of -0.8 V at 10 mA cm^{-2} was reported for WSe_2, while the value was -0.55 V for MoS_2. Furthermore, WS_2 and $MoSe_2$ show better performance for hydrogen evolution than do MoS_2 and WSe_2, which is because the former contain a larger content of the 1T phase. The kinetics for these four 1T-phase-based TMD materials are subject to both Volmer and Heyrovsky reactions, which control the HER rate. The calculated Tafel values of WS_2, $MoSe_2$, MoS_2, and WSe_2 are 85, 82, 99, and 4240 mV dec^{-1}, respectively, showing the superior performance of the 1T phase of WS_2 and $MoSe_2$ for hydrogen evolution over the corresponding 2H phases. In another study, Gao and co-workers[61] showed that the kinetic energy barrier for 2H-to-1T phase transformation could be lowered due to the presence of negative charges in the 1T-MoS_2 phase, while spontaneous phase transformation into the 1T′ phase (distorted monolayer structure) from the 1T phase might occur. The rapid charge transfer dynamics assist in achieving superior HER performance with the 1T′-MoS_2 phase, while its catalytic activity is comparable with that of the 2H phase.

EC-HER on Heterophases: Coupling different phases is an effective route to increase the electrical conductivity and increase the effective catalytically active surface area, thereby improving the HER catalytic performance. Kwak and co-workers[87] have prepared 1T′-phase-based MoS_2 nanostructures by means of ammonium (A) and methylammonium (MA) intercalation synthetic methods and evaluated the HER catalytic efficiency of the materials. The authors observed both higher catalytic activity and excellent stability with the MA intercalated 1T′-MoS_2 nanostructures compared with A-intercalated 1T′-MoS_2. With increasing concentrations of either A or MA, the phase conversion from 2H to 1T′ increased, which could be further accelerated by increasing the number of S vacancies, according to first-principles calculations. Such calculations help to corroborate the higher durability of MA-intercalated 1T′-MoS_2 nanostructures, suggesting that the repulsion between the positively charged MA moieties decreased. However, questions remain unanswered regarding the phase conversion of 1T and 1T′-MoS_2 nanostructures using one-step hydrothermal protocols with the aid of MA because of the underlying issue of stability, as we discussed in the previous section. Conversely, the stability of MA-intercalated 1T′-MoS_2 nanostructures was reported to be ≈ 6 months under ambient conditions, while the A-intercalated 1T′-MoS_2 nanostructures converted to the 2H phase very fast. The overpotential and Tafel slope of MA- and A-intercalated 1T′-MoS_2 nanostructures at 10 mA cm^{-2} were 0.17 V and 38 mV dec^{-1} and 0.2 V and 45 mV dec^{-1}, respectively. The kinetic evaluation of the 1T′-MoS_2 nanostructures exhibited upward slopes regarding HER activity, while the Tafel slope indicated the two-step mechanism for HER to be the Volmer reaction and Heyrovsky reaction.

In another study, Kwak and co-workers[46] have synthesized nitrogen (N)-doped 1T′-MoS_2 layered nanostructures using various alkyl amines, namely, MA, ethylenediamine (EDA), diethylenetriamine (DETA), and triethylenetetramine (TETA), as intercalants that correspond to 1–4 N atoms. With the intercalation of amine molecules at 10 at%, the lattice constant expands by up to 160%. The concentration of doped N atoms increases with increasing number of N atoms in the amine, improving the catalytic HER performance. The calculated data show that all the amine-intercalated N-doped MoS_2 samples display excellent HER performance in the order of TETA > DETA > EDA > MA. The intercalation with TETA yields a Tafel slope of 36 mV dec^{-1} and an overpotential of -160 mV (vs RHE) at 10 mA cm^{-2}. Theoretical analysis indicates that the N doping and amine intercalation enhance the density of states near the Fermi level in a narrow range, showing an effective overlap of the d_{z2} (Mo), p_z (S), and p_z (N) orbitals. The combination of these factors increases the electron concentration at the surface and hence the mobility for enhanced HER. It is also noted that most of the catalytic active sites are S vacancies. The authors argued that the HER performance could be increased by controlling the amine intercalation in the MoS_2 samples. Likewise, Wang and co-workers[88] have engineered multiphasic 1T/2H-MoS_2 nanostructures by means of a hydrothermal approach with the introduction of ammonium bicarbonate. A plethora of exfoliated MoS_2 phases are observed because the preparation process involves many ions and small molecules that originate from decomposition of the starting materials. The synthesis variables, such as temperature, could influence the 1T-phase content in the desired polytype. As reported, the highest 1T-phase content was achieved at an optimum temperature of 200 °C. However, the performance of HER decreased with increased synthesis temperature. This phenomenon is attributed to the thermodynamically metastable character of the 1T phase. With the highest 1T-phase content, the as-prepared polytype reached a Tafel slope of 46 mV dec^{-1}, suggesting that these multiphasic 1T/2H-MoS_2 nanostructures pave the way for improved electrocatalytic performance. Liu and co-workers[89] have prepared 4H/fcc-Au@MoX_2 (X = Se and S) nanocomposites for electrocatalytic HER in an acidic environment and reported excellent activities with a low overpotential of 178 mV at 10 mA cm^{-2} and a small Tafel slope of 43.3 mV dec^{-1}. The excellent activities were attributed to high concentrations of the 1T′ phase in the prepared $MoSe_2$ and MoS_2 monolayers. It is suggested that different crystal phases of noble multimetallic nanomaterials could boost the catalytic properties and be beneficial for HER in acidic medium. Similarly, Fan et al.[90] have prepared three different multimetallic nanomaterials, 4H/fcc trimetallic Au@PdAg core–shell, 4H/fcc trimetallic Au@PtAg and tetrametallic Au@ PtPdAg core–shell nanoribbons (NRBs), using 4H/fcc Au@Ag NRBs as seeds by means of a galvanic reaction method under ambient conditions. Among those materials, the prepared 4H/fcc Au@ PdAg NRBs show promising performance for HER with longer durability. The authors reported that the overpotential of that nanocomposite was ≈ 26.2 mV, and the Tafel slope was 30 mV dec^{-1}, which is comparable to that of Pt black. The synergistic interplay among their dendritic surface morphology, the effects of multiple

**ADVANCED
SCIENCE NEWS**

www.advancedsciencenews.com

**ADVANCED
MATERIALS**

www.advmat.de

components, and the unique crystal structure were the major reasons for the superior electrocatalytic performance of 4H/fcc Au@ PdAg NRBs. In a similar study, Zhang and co-workers[91] have prepared well-crystalline lotus-thalamus-shaped Pt–Ni anisotropic superstructures (Pt–Ni ASs) with a spatial heterogeneity of the crystal structures and compositional elements. The superstructures are composed of one fcc-phase Ni-rich "core," several hcp-phase Ni-rich "arms" protruding from the core, and facet-selectively grown fcc-phase Pt-rich "lotus seeds" on the ends of the "arms." The intrinsic anisotropic feature of this material enables superior electrocatalytic activity and stability for HER under alkaline conditions compared to that of commercial Pt/C and other reported electrocatalysts.[91]

EC-HER on Multiphases: The heterostructure matrix with different phases enables tuning of the electronic structures, thereby promoting the electrochemical activity for enhanced HER performance. Great efforts have been made so far by fabricating 1T-MoS_2 catalysts along with other phase(s) on supported catalysts to increase the number of catalytic active sites as well as the stability. Developing effective HER electrocatalyst hybrids with such phase(s) should establish a balance between good conductivity and abundant active sites, which significantly boosts the HER rate for practical applications. Regarding optimization to attain such electrocatalysts for HER, we often see these materials coupled with graphene or carbon nanotubes or doped with other compounds to give preferable structural properties, for example, high specific surface area and electrical conductivity and synergistic electrical effects. Red phosphorous possesses the ability to expand the interspace between S-Mo-S layers of bulk 2H-MoS_2, which can further exfoliate the bulk MoS_2 into thin flakes. Red phosphorous not only embeds into the S-Mo-S atomic plane but also induces the glide of S atomic planes around the P-doped areas, allowing in-plane heterostructures originating from 2H- and 1T-MoS_2 domains. Based on this assumption, Wang et al.[43] have implemented one-step annealing treatment methods following an ultrasonication process to fabricate and engineer such in-plane 1T–2H-MoS_2 heterostructures to evaluate the electrocatalytic HER performance. The resultant in-plane 1T–2H-MoS_2 heterostructures show significant improvement in electrical conductivity, highly exposed active sites, and long-term durability. The estimated electrical conductivity of 8620 S m^{-1} was noted to be 500-fold greater than that of 2H-MoS_2 (16.1 S m^{-1}), while its Tafel slope of 65 mV dec^{-1}, high electrochemical surface active area of 60.3 cm^2, hydrogen turnover frequency of 13.14 s^{-1} at 250 mV and stability performance of 500 d at room temperature for HER in a 1 M KOH electrolyte were reported. Additionally, the authors emphasized that the as-prepared in-plane 1T–2H-MoS_2 heterostructures may act as potential electrocatalysts in an environment where simultaneous HER and OER can be observed in a one-cell system. However, they proposed a different Volmer-Heyrovsky reaction mechanism for HER over the in-plane 1T–2H-MoS_2 heterostructures, rather than the conventional Volmer mechanism for 2H-MoS_2. There are several factors that are responsible for this excellent activity, for example, more exposed active sites in the plane of the 1T–2H-MoS_2 heterostructures than in the basal plane of 2H-MoS_2, rapid electron transfer for accelerating the HER activit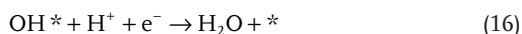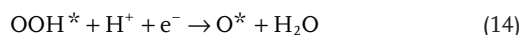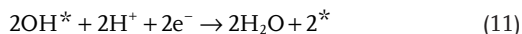y due to the improved electrical conductivity, and the hydrophilic nature of the in-plane 1T–2H-MoS_2 heterostructures.[43]

Application of the 1T-MoS_2 phase as a cocatalyst with semiconductors may also improve the electrochemical activity of HER. To confirm this hypothesis, He[92] attempted to fabricate composite nanostructures together with a metallic 1T-MoS_2 phase with the most common TiO_2 nanotube semiconductors and Si-doped TiO_2 nanotubes, which showed excellent electrochemical activity for HER. Unlike chemically exfoliated in-plane multiphasic MoS_2 electrocatalysts, which show a Tafel slope of 43 mV dec^{-1}, the 1T-MoS_2 phase/TiO_2 nanotube heterojunction exhibited a Tafel slope of 42 mV dec^{-1}. Moreover, addition of the 1T-MoS_2 phase to the Si-doped TiO_2 nanotubes led to a relatively low Tafel slope of 42 mV dec^{-1}, indicating that this designed heterojunction may be able to provide good performance in the context of HER activity. Optimization of abundant active sites along with increased conductivity could be a promising approach to improve the HER activity. Based on this observation, Shi and co-workers[93] have fabricated 1T–2H-MoS_2 phase nanosheets on carbon by incorporating the 1T phase in primitive 2H-MoS_2 nanosheets via two-step hydrothermal methods. Electrochemical experiments show that the composite materials have excellent electrochemical activity compared to that of the primitive 2H phase. A calculated overpotential of 64 mV in 0.5 M H_2SO_4 at 10 mA cm^{-2} and a Tafel slope of 49 mV dec^{-1} were reported, which greatly surpassed the activity of previous MoS_2 catalysts. The superior HER activity as well as the good stability of the composite nanosheet materials is likely because of the alteration of the electronic structure. The reasons for such good performance include the abundance of unsaturated sulfur atoms from the distorted structure, which function as active sites for HER, and the extent of disorder, which gives quasi-periodic nanodomain arrangements that partially maintain the 2D electron heterojunction, resulting in rapid interdomain electron transport. It is also assumed that the incorporation of the metal 1T phase in the primitive 2H-MoS_2 matrix increases the intrinsic conductivity of the nanodomains and accelerates the conjugation between the positive protons and catalysts. Likewise, Liu and co-workers[94] have prepared 1T/2H-MoS_2 polymorphs via a facile one-step hydrothermal route utilizing thiourea and sodium molybdate dehydrate as the precursors for four hours at 180 °C with the assistance of propionic acid. The as-synthesized electrocatalysts show reasonable activities, wherein the overpotential and Tafel slope were approximately 220 mV at 10 mA cm^{-2} and 61 mV dec^{-1}, respectively. The evaluated electrocatalytic performance is relatively lower than that for exfoliated MoS_2, while its preparation protocols can be applied to other TMD-based materials for improved HER activity.

The formation of 1T-$MoSe_2$ nanosheets and NiSe nanowire array heterostructures can improve the HER efficiency in a basic medium. A number of potential advantages can emerge from such heterostructures: a) the 1T-phase $MoSe_2$ exhibits the intrinsic catalytic activity, and NiSe can promote water dissociation, while merging these two features can result in higher HER activity; b) multidimensional activities such as accelerating electron transfer along the axial dimension, efficient mass transport through solid–liquid–gas three-phase interfaces and

ADVANCED
SCIENCE NEWS
www.advancedsciencenews.com

ADVANCED
MATERIALS
www.advmat.de

facile gas escape to release active sites can be done with NiSe nanowire cores; and (c) 1T-MoSe$_2$/NiSe nanosheet/nanowire (NS/NW) arrays supply accessible active reaction sites at three-phase interfaces. Taking advantage of such features, Zhang and co-workers[106] have prepared 1T-MoSe$_2$/NiSe nanosheet/nanowire (NS/NW) arrays for electrochemical water splitting, finding that the in situ electron injection from NiSe to MoSe$_2$ induces the phase transition from the 2H phase to metallic 1T phase. With this heterostructure, a low overpotential of 200 mV at a current density of 50 mA cm^{-2} was achieved along with excellent durability in a basic environment.

SPE for Electrocatalytic ORR (EC-ORR) on Single Phases: An active electrocatalyst has not yet been shown to have true potential for the ORR—a well-known reaction scheme—which has been reported to be due to sluggish kinetics that require a four-electron transfer mechanism; understandably, this process is much more complicated than the HER. In acidic conditions, the four-electron process reduces O$_2$ directly in H$_2$O or OH$^-$ in basic solution (see below). The four-electron process can proceed through multistep mechanisms. Depending on the oxygen dissociation energy barrier on the catalyst surface, either a dissociative or associative mechanism has been suggested for the direct four-electron pathway.[107] Apart from a direct mechanism, a two-electron transfer step first leads to hydrogen peroxide formation, followed by further reduction to water, a so-called indirect mechanism.[107] The involvement of varied intermediates is the main distinguishing filter between these two mechanisms, which changes the framework of the free energy pathway.

$$\text{Dissociative: } O_2 + 2* \rightarrow 2O^* \tag{9}$$

$$2O^* + 2H^+ + 2e^- \rightarrow 2OH^* \tag{10}$$

$$2OH^* + 2H^+ + 2e^- \rightarrow 2H_2O + 2^* \tag{11}$$

$$\text{Associative: } O_2 + * \rightarrow O_2^* \tag{12}$$

$$O_2^* + H^+ + e^- \rightarrow OOH^* \tag{13}$$

$$OOH^* + H^+ + e^- \rightarrow O^* + H_2O \tag{14}$$

$$O^* + H^+ + e^- \rightarrow OH^* \tag{15}$$

$$OH^* + H^+ + e^- \rightarrow H_2O + * \tag{16}$$

The thermodynamic free energies of all the above intermediates were determined for a variety of close-packed metal surfaces, and a volcano framework was designed relating the theoretical ORR activity and their oxygen binding energy, where Pt is near the volcano peak.[23] If the metal binds oxygen too strongly, then the ORR activity involves proton–electron transfer to either O* or OH*, while if the binding is too weak, then the ORR activity is limited to proton–electron transfer to O$_2$* or cleavage of the O—O bond in O$_2$, depending on the applied

potential.[23] The former is the associative mechanism, and the latter is the dissociative mechanism. While the benchmark ORR catalyst in terms of efficiency is Pt, its scarcity and stability issues (Pt agglomeration, dissolution, sintering, detachment, and corrosion of carbon support materials) prevent its potential application. In an attempt to alleviate this problem, many studies have been performed on the rational design and fabrication of novel ORR electrocatalysts with activity comparable to or even superior to that of Pt-based electrocatalysts.[108,109] Very recently, it was recognized that phase-based electrocatalytic materials such as MoS$_2$, WS$_2$, and TaS$_2$ have potential in improving the ORR activity. Among these materials, layered TaS$_2$ materials show three basic phases, namely, 2H, 1T, and 3R, while suitable synthetic methods generate only 2H and 1T phases because 3R generally includes a mixture of other phases.[108] The application of 1T-MoS$_2$ in HER motivates the usage of different phases of TaS$_2$ in ORR as well for HER since the phase transformation can change the catalytic activity. Both the 1T-TaS$_2$ and 2H-TaS$_2$ phases show comparable catalytic performance to that of Pt/C catalysts, which can be increased further upon electrochemical pretreatment. The authors stated that the presence of Ta$_2$O$_5$ during oxidation may accelerate the activity of the 2H-TaS$_2$ phase. Computational results indicate that the free energy of hydrogen adsorption on the basal planes and edge sites of each phase has significant effects on the respective reactions.[108] For example, the binding energy of hydrogen atoms on edges is too weak for the 1T-TaS$_2$ phase, leading to positive values for ΔG over the whole hydrogen coverage range (**Figure 5**). At 25% coverage, a value close to thermoneutral (ΔG = 0.46 eV) was observed. At higher coverage, hydrogen adsorption became even less favorable, resulting in poor HER performance. In addition, HER activity remains less active on the basal plane since it binds hydrogen atoms very weakly (ΔG = 1.24 eV).[108]

To improve the ORR, a new class of heterostructured (La,Sr)$_2$FeO$_{4-\delta}$ (LSF$_{214}$)–La$_{0.8}$Sr$_{0.2}$FeO$_{3-\delta}$ (LSF$_{113}$) electrode materials has emerged, consisting of a Ruddlesden–Popper (R–P) LSF$_{214}$ phase formed on the surface of the LSF$_{113}$ framework.[110] The higher catalytic activity of the LSF$_{214}$ phase and the lattice mismatch between the LSF$_{214}$ and LSF$_{113}$ interfaces accelerates oxygen vacancy formation and oxygen molecule adsorption, resulting in one order of magnitude improvement in ORR activity.

3.1.2. SPE for Electrocatalytic OER (EC-OER) on Single Phases

While the use of phase-based materials has been considered an advantageous situation for electrocatalytic HER, much less has been accomplished with respect to OER because of the sluggish kinetics and high positive potential required to compensate for the kinetic barrier.[23] It is important to keep in mind that the oxygen reduction reaction (ORR) is another slow kinetic process with high overpotential in electrochemical studies. Active OER catalysts in acidic medium have reasonable binding energies to couple with intermediates.[23] In terms of activity and stability, the OER catalysts, however, need to be exhibit superior performance under the appropriate reaction conditions, especially under high oxidation potentials. While we have seen much effort in the rational design and modulation of HER electrocatalysts, less attention has been paid to
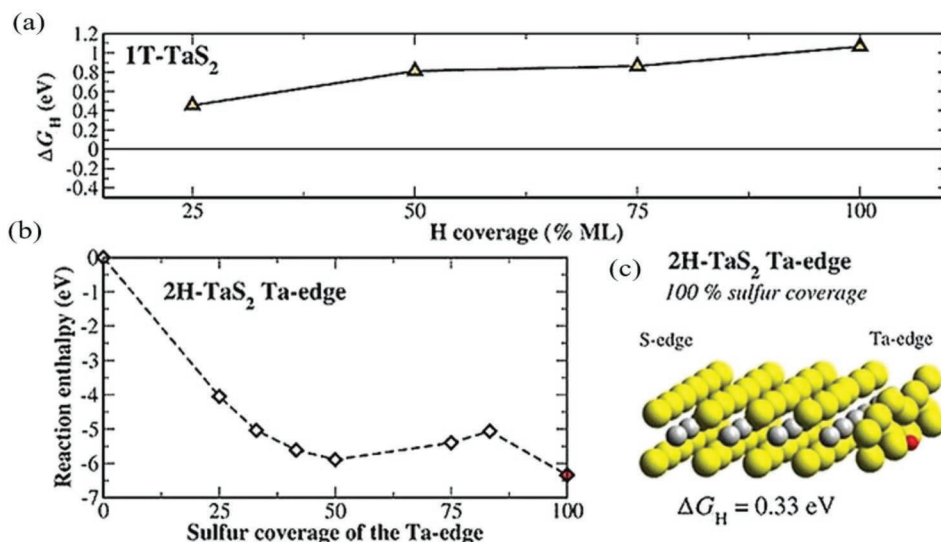
Figure 5. a) Free energy, ΔG_H versus hydrogen adsorption on the edge of 1T TaS$_2$, b) the free energy as a function of sulfur coverage of the Ta edge of 2H TaS$_2$, and c) the structure of a 100% sulfur-covered Ta edge. a–c) Adapted with permission.[108] Copyright 2017, Wiley-VCH.

developing OER electrocatalysts, representing a major bottle-neck of research on electrochemical water splitting.[23] Even when HER activity can be realized over an electrocatalyst, for efficient overall water splitting, it is highly desirable that the electrocatalyst also exhibits good OER characteristics under identical operating conditions. We have seen from a literature survey that the Volmer reaction associated with water splitting under alkaline conditions includes a water dissociation step at the beginning of the HER, making understanding of the overall process troublesome, while in acidic environments, such dissociation is relatively understood.[111,112]

MoS$_2$ and TaS$_2$ have been studied for HER for many years, while the electrocatalytic activity for OER with these two materials was recently revealed.[113] The reaction scheme for OER requires a four-electron proton transfer process with intermediates such as OH*, O*, and OOH*—a similar mechanism occurring on the catalyst surface for metal oxides, nitrides, and sulfides (**Figure 6**).[113] Computations show that the edge sites of both MoS$_2$ and TaS$_2$ are more active than their basal plane sites in the context of OER performance. When plotting the free energy diagram to evaluate the activity of edge sites in acidic solution, it is verified that the 1T-phase edges have the lowest kinetic energy barrier and that the 2H phase is the most active, with 50% sulfur coverage. For most of the phases, the OER activity is limited by splitting water through a one proton–electron transfer process (O* + H$_2$O → *OOH + H$^+$ + e$^-$), which introduces the overpotential needed to overcome the barrier of O=O formation.[23] The oxygen formation step via (OOH* → * + O$_2$ + H$^+$ + e$^-$) has the largest free energy difference occurring with S-edge sites of 2H-TaS$_2$. An as-prepared 1T/2H-MoS$_2$ polytype with a high 1T-phase content achieved a Tafel slope of 46 mV dec^{-1}, implying that multiphasic 1T/2H-MoS$_2$ nanostructures could pave the way for improved electrocatalytic performance. Volcano plots indicate that the activity of edges of 1T-MoS$_2$ and TaS$_2$ is comparable with that of IrO$_2$ and manganese oxides (Figure 6).[113] The experimental investigation has revealed that

an overpotential of 0.42 V is needed to reach a current density of 10 mA cm^{-2} with the 1T-MoS$_2$ phase, demonstrating the most efficient catalytic activity among the evaluated species (0.45, 0.48, and 0.54 V for 1T-TaS$_2$, 2H-MoS$_2$, and 2H-TaS$_2$, respectively). This activity is comparable with that of some electrocatalysts, for example, Mn oxide (0.54 V), and Mn$_3$O$_4$/CoSe$_2$ (0.45 V) in alkaline solution, but slightly worse than that of IrO$_x$ electrocatalysts in acidic solution.[113] Tafel plots show relatively high Tafel slope values of approximately 322, 282, 361, and 255 mV dec^{-1} for 1T-MoS$_2$, 1T-TaS$_2$, 2H-MoS$_2$, and 2H-TaS$_2$, respectively. However, with annealing treatment, the phase reverts from 1T-MoS$_2$ to 2H-MoS$_2$, resulting in a decrease in catalytic activity, and it has been confirmed that in acidic solution, the 1T phase exhibits higher catalytic activity toward water oxidation than does the 2H phase.[113]

With various crystal phases, noble metal core–shell nanoparticles could be an excellent choice for EC-OER because the synergistic effects between the multicomponents, unusual crystal structure and core can increase the electron transport at the interface. Based on that idea, Fan et al.[114] have prepared 4H/fcc-Au@Ir core–shell NRBs and evaluated their EC-OER performance. It was highlighted that the Tafel slope was ≈51.4 mV dec^{-1}, which was lower than that of the commercial Ir/C catalyst (74.3 mV dec^{-1}), suggesting highly efficient oxygen evolution activity of Au@Ir NRBs. The plausible reasons were the accelerated electron transport due to the 1D Au core in the Au@Ir NRBs, the abundance of active sites in the dendritic structure and the synergistic effects between the different Au and Ir components.[114]

3.1.3. SPE for Electrocatalytic OWS (EC-OWS)

The overall electrocatalytic water-splitting reaction has been recognized as promising in producing both hydrogen and oxygen in the presence of active catalysts. It is important in this reaction that the catalytic materials should have the ability to suppress
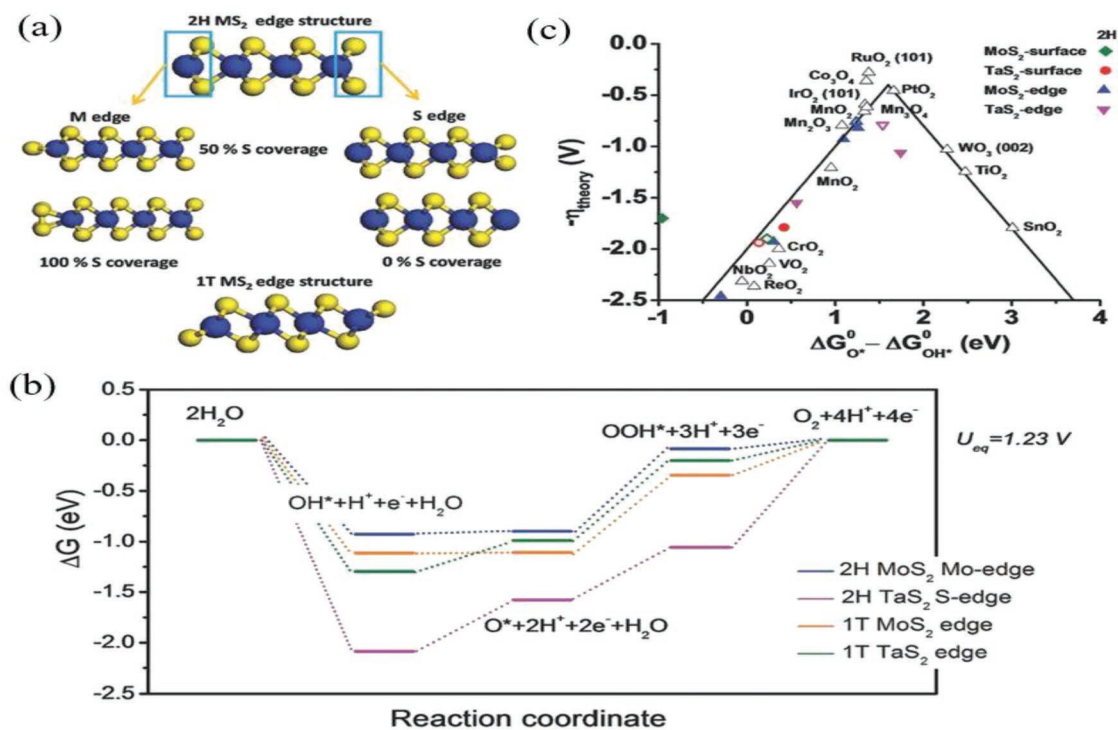
Figure 6. a) Schematics of edge structures of 2H and 1T-MS$_2$. b) In acidic solution, the reaction pathway of OER on the most active edge sites. c) Volcano plot of overpotential versus the difference in the adsorption energy of O* and OH*. a–c) Adapted with permission.[113] Copyright 2016, Wiley-VCH.

HER and OER activity regardless of the reaction medium. The likely reason is the water dissociation related Volmer steps stem from an unfavorable orbital orientation of the employed catalysts. It is thus necessary to synthesize catalytic materials with various crystal phases that can ameliorate the kinetic barrier. In the following section, we will examine and discuss some phase materials from recently published papers.

EC-OWS on Single Phases: As part of the growing scientific advances in energy conversion processes, water splitting in the presence of electrocatalysts appears to be a promising approach to produce hydrogen fuels, representing a functional and practical means.[115,116] The main obstacle to achieving high-performance water splitting is lowering the driving overpotential and improving the efficacy of the electrocatalyst. The expected performance of an electrocatalyst for the overall water-splitting system is largely dependent on: a) the intrinsic activity of catalytic active sites,[117] b) the improved conductivity of the electrode material,[118] c) the increased mass transfer properties, and d) the increased density of electrocatalytic active sites or surface area of the electrocatalysts.[119]

Li et al.[120] have studied the overall water-splitting performance (both OER and HER) of hybrid nanotube arrays (FeCoNi-HNTAs). Due to its excellent electrode kinetics, facile charge transfer, and improved intrinsic electrocatalytic HER activity, 1T'-MoS$_2$ was incorporated within the hybrid nanotube arrays. The FeCoNi-HNTAs were prepared from ternary Fe-, Co-, and Ni-based layered double hydroxide nanowire arrays (FeCoNi-LDH-NWAs) supported on a Ni foam substrate. The FeCoNi–HNTAs display striking performance for HER and OER in terms of catalytic activity and durability. The results

show that an overpotential of 58 and 184 mV was realized at a current density of 10 mA cm^{-2} for HER and OER, respectively, whereas an extraordinary durability of 200 mA cm^{-2} for 80 h continuous operation was observed. The reported Tafel slopes for HER and OER were 37.5 and 49.9 mV dec^{-1}, respectively, indicating rapid reaction dynamics. The overall cell voltage of 1.429 V in alkaline electrolyte solution was observed at a current density of 10 mA cm^{-2} when the FeCoNi–HNTAs were employed as both the anode and cathode for overall water splitting (**Figure 7**).

The plausible reasons for the performance of this hybrid structure are ascribed to the 1T'-MoS$_2$ activities and synergistic role of the trimetallic system. During OER reactions, Fe^{3+} functions as a highly active electrocatalytic site for OER since intermediate species can easily adsorb on the Fe sites due to the lower Gibbs free energy. In addition, it is proven that the addition of Fe can lower the overpotentials and increase the catalytic activity of Ni-based compounds for OER reactions. The contribution of Co ions is to adjust the electronic state of Fe and promote a high valence state, while the Co^{3+} ion positioned at octahedral sites is more beneficial for OER than the Co^{2+} ion positioned at tetrahedral sites, improving the intrinsic activity for OER reactions. The incorporation of Fe and Co in Ni-based compounds is seen to be an intriguing promoter because an increase in the quantity of Ni^{3+} centers affects the local electronic configuration and hence increases the electrocatalytic performance as well.[120] On the other hand, the metallic 1T'-MoS$_2$ phase could be maintained under both OER and HER operation, indicating that the stability of this phase was significant at both oxidation and reduction
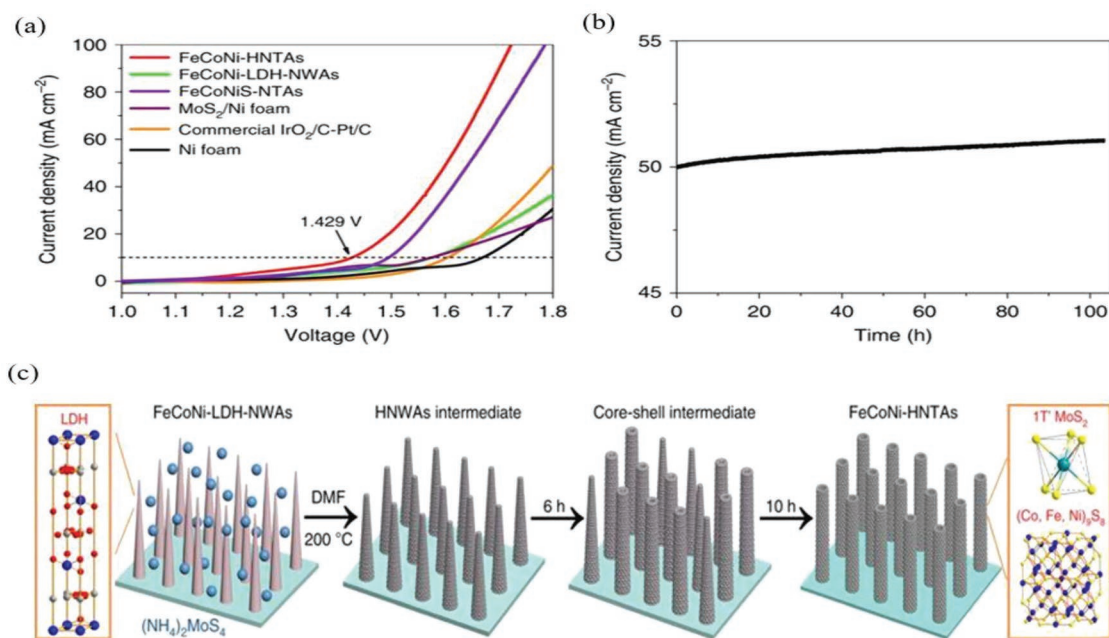
ADVANCED
SCIENCE NEWS
www.advancedsciencenews.com

ADVANCED
MATERIALS
www.advmat.de

Figure 7. a) Polarization plots in 1 M KOH electrolyte with a typical two-electrode set-up. Scan rate: 1 mV s⁻¹. b) Chronoamperometric response recorded on FeCoNi–HNTAs at a constant cell voltage of 1.59 V. c) Schematic of FeCoNi–HNTAs preparation and performance evaluation over FeCoNi-HNTAs for overall water splitting. a–c) Adapted with permission.[120] Copyright 2018, Springer Nature.

potentials. It is possible that the 1T′-MoS$_2$ phase could revert to the semiconducting 2H phase under the influence of reaction conditions, such as temperature, but in this case, it did not. However, long-term OER operation can oxidize MoS$_2$, indicating that 1T′-MoS$_2$ can impact both water-splitting half-reactions.[120]

In their previous studies,[121] Li et al. have evaluated the porous hybrid nanostructures together with amorphous Ni-Co complexes with 1T-phase MoS$_2$ (referred as PHNCMs) as a function of hydrazine (N$_2$H$_4$) quantity for the overall water-splitting reaction. Ni–Co hydroxide ultrathin nanosheets (NCUNs) act as precursors and templates for the subsequent PHNCM synthesis. The authors highlighted that overpotentials of 70 and 235 mV were achieved at 10 mA cm⁻² for HER and OER, respectively, over the hydrazine-promoted PHNCM electrocatalysts, demonstrating highly active and ultrastable electrocatalytic performance.[121] The calculated Tafel slope values indicate rapid reaction rate mechanisms for HER (38.1 mV dec⁻¹) and OER (45.7 mV dec⁻¹). In terms of overall water-splitting efficiency, the authors reported an overpotential of 1.44 V to achieve a current density of 10 mA cm⁻² for a 48 h operation without degradation (**Figure 8**). The possible reasons for this performance over PHNCMs were the amount of hydrazine hydrate (HZH), which was responsible for the phase transformation of MoS$_2$ and the crystallization of Ni–Co-based compounds.[121] With HZH, Ni–Co-based compounds were converted from a partial metallic state into amorphous complexes, and MoS$_2$ was transformed into a metallic 1T phase. The electron-donor ability of HZH could increase the quantity of amorphous Ni–Co complexes, further stabilizing the 1T-phase MoS$_2$. The facile electrode kinetics, improved electric conductivity and substantial increase in the number of electrocatalytic active sites can be realized with 1T-phase MoS$_2$. The

authors have also elucidated that porous nanostructures have the potential to generate more active sites and can successfully increase mass transport and gas permeability during water electrolysis. In addition, the preferential intramolecular proton transfer ability of the hydrazine-promoted Ni–Co complexes is thought to be advantageous in reducing the overpotential of electrocatalytic H$_2$ evolution.[121] Therefore, the PHNCM nanostructures have tunable capacity in increasing the electrocatalytic performance for overall water splitting.

EC-OWS on Heterophases: A good understanding of how the metallic MoS$_2$ phase affects the overall water-splitting reactions, especially the OER and HER, is of great importance. The engineering and architecting of heterointerfaces along with metallic MoS$_2$ have some beneficial effects for the overall water-splitting reactions. Zhang and co-workers[122] have designed multiple heterointerfaces along with metallic MoS$_2$ and evaluated how these heterostructures facilitate the intrinsic activities of the electrocatalysts. In basic medium, water undergoes dissociation (Volmer step), producing intermediates H* and OH⁻ that are chemisorbed on the surface of HER-assisted electrocatalysts.[17] If an electrocatalyst can perform that task effectively, an improved performance can ultimately be realized. Likewise, the water-oxidation activity for OER in basic medium depends on the chemisorption and dissociation of OH⁻ and the produced reaction intermediates such as OH*, OOH*, and H+.[123] Therefore, OER electrocatalysts that have the ability to combine both chemisorbed oxygen-containing and hydrogen intermediates can improve the water-oxidation reaction. There are reports that the undercoordinated Mo–S sites along the edges of MoS$_2$ show high chemisorption ability for both OH⁻ and oxygen-containing products, thereby enhancing the overall electrochemical water-splitting performance.[104] For example, a favorable HER performance was realized for the interfaces
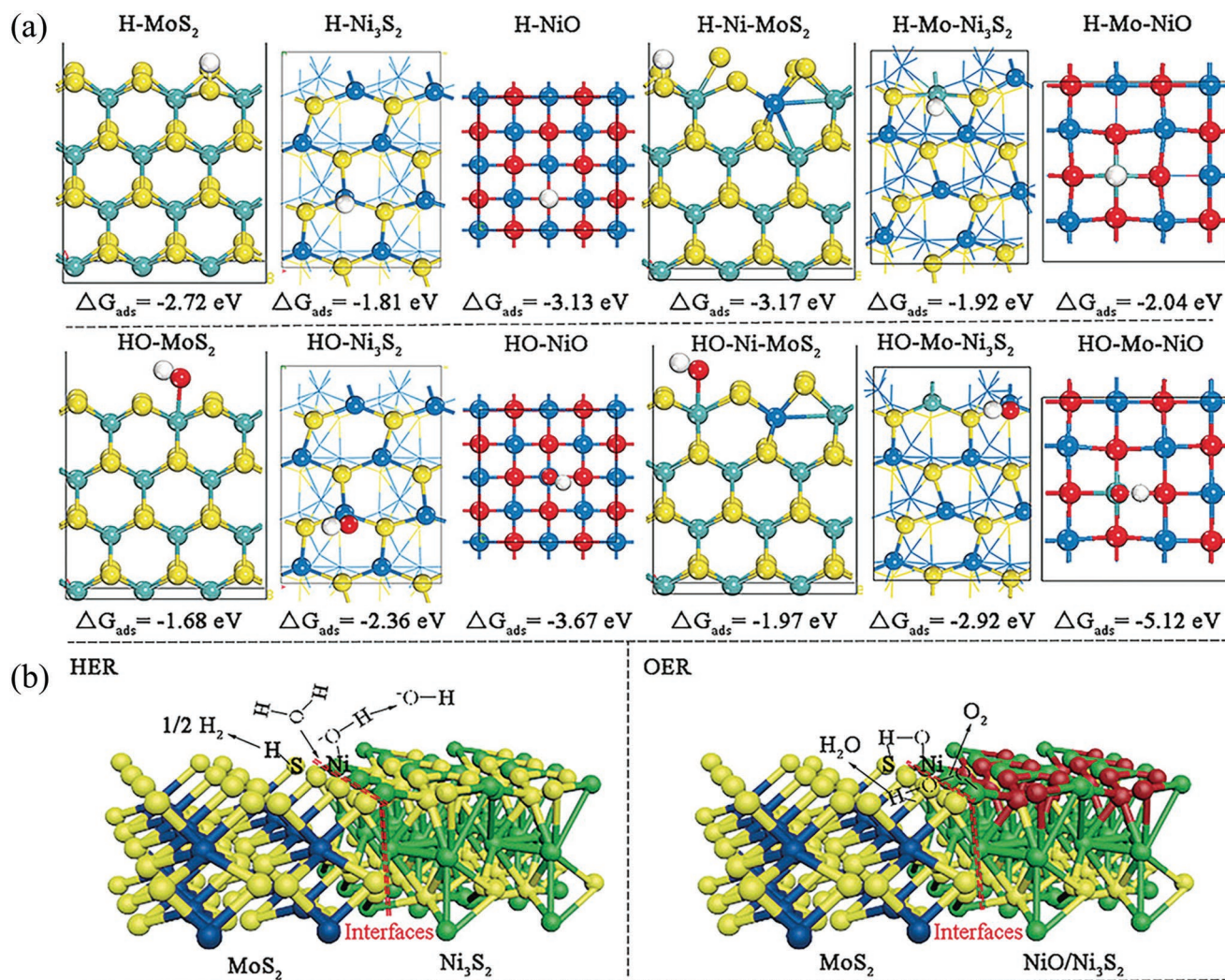
Figure 8. DFT analyses show heterointerfaces effects on overall water splitting reactions. a) H and OH intermediates chemisorption on the surfaces of MoS_2, Ni_3S_2, NiO, MoS_2/Ni_3S_2 heterostructures (Ni-MoS_2 and Mo-Ni_3S_2 models), and MoS_2/NiO heterostructures (Ni-MoS_2 and Mo-NiO models) respectively; and b) the tentative reaction mechanisms for the dissociation of H_2O, OH, and OOH intermediates on the MoS_2/Ni_3S_2 heterostructures. Yellow = S, green = Ni, blue = Mo, white = H, red = O. a,b) Adapted with permission.[122] Copyright 2016, Wiley-VCH.

between MoS_2 and Ni_3S_2, while the heterointerfaces between MoS_2 and NiO favored the OER process.[122] Density functional theory (DFT) analyses reveal that the chemisorption free energy of H is −3.17 eV on the surface of Ni-doped MoS_2 (Ni-MoS_2) samples, which is much lower than that for the (101) surface of Ni_3S_2 (−1.81 eV) and (002) surface of MoS_2 (−2.71 eV), indicating that H chemisorbs preferentially on the Mo–S edge sites (Figure 8).[122] In contrast, the chemisorption free energy of HO is −2.92 eV, which is lower than that on the surface of MoS_2 (−1.68 eV) and the surface of Ni_3S_2 (−2.36 eV), suggesting that the surface undercoordinated Ni sites of Mo-doped Ni_3S_2 (Mo–Ni_3S_2) are the first choice for HO chemisorption. The oxygen-containing intermediates show strong binding ability toward the (101) surface of Mo–Ni_3S_2. In addition, the chemisorption free energy of HO on the interfaces between MoS_2 and NiO for OER is −5.12 eV, implying that the Mo sites of Mo-doped NiO (Mo-NiO) readily facilitate the process. According to the DFT calculations, it is concluded that both Mo-Ni_3S_2 and MoS_2–NiO

interfaces promote the H chemisorption of MoS_2 and HO chemisorption of Ni_3S_2 and NiO. By the promotion of such intrinsic capacity, ideal electrocatalysts can effectively improve the overall water-splitting reactions through the deployment of HER and OER processes.[122]

3.2. SPE for Photocatalytic and Photoelectrocatalytic Water Splitting

Photocatalytic and photoelectrocatalytic water splitting are recognized as two of the most promising approaches in producing hydrogen from the utilization of solar energy. Since both processes take place under light illumination, the employed catalytic materials in these redox processes should fulfill some physical requirements. The band position and bandgap are the two key requirements in water-splitting photocatalysis, while the catalytic materials should have a minimum bandgap

**ADVANCED
SCIENCE NEWS**
www.advancedsciencenews.com

**ADVANCED
MATERIALS**
www.advmat.de

of 1.23 eV to meet the redox potentials of the H^+/H_2 and O_2/H_2O pairs. However, a plethora of photocatalytic materials have been evaluated in these redox reactions, and a number of phase materials have also gained consideration. SPE could be effective in these redox processes since it can tune the bandgap of the materials as well as other electronic properties, which we will see in the following section.

3.2.1. SPE for Photocatalytic HER (PC-HER)

A keen interest has accumulated in the scientific community to produce clean hydrogen fuel from a so-called photocatalytic water-splitting reaction by utilizing HER reactions over earth-abundant semiconductors because this is the most prominent way to convert solar energy into chemical products. The application of many novel photocatalysts has been theoretically and experimentally investigated for HER, including metal oxides,[124,125] silicides,[126] carbides,[127] and chalcogenides.[128] The application window of these photocatalytic materials, however, needs to be identified in detail because photon-to-exciton conversion, charge-carrier (e^-/h^+) recombination, light absorption range, quantum efficiency, etc., are likely related to their nanostructural properties.[129] Adding cocatalytic materials to the semiconductor surface could improve the photocatalytic activity, providing more hydrogen reduction sites and reducing the activation energy to ultimately accelerate proton reduction.[130,131] In this regard, owing to their large surface-to-volume ratio, tunable bandgap, suitable band position, and highly active chalcogenide atoms at exposed edges, TMD materials and some other metal oxides are unparalleled candidates for photocatalytic HER.[1,132] To improve the photocatalytic activity, attention has been given to synthesizing less expensive photocatalytic materials rather than using noble metals. As part of this advancement, the reaction mechanism of hydrogen evolution activity has also been studied.[133] At the end of this section, we provide a summarized overview (**Table 2**) of the recent publications that use the photocatalytic concept for hydrogen production.

PC-HER on Single Phases: The phase engineering approach marks a crucial step toward determining the latent potential of 2D TMD materials, which is indeed an inspiring development that could be a solution for many problems in materials science fields. Cho et al.[29] have observed that based on stacking geometry, MoS_2 shows two polymorphisms, namely, 2H and 1T phases. By rotating one of the 2H Mo-S tetrahedra by 60°, a 1T phase can be achieved. The 1T phase is metastable in nature, while the 2H phase is stable and has a semiconductive

Table 2. Summary of phase based photocatalytic materials for HER system.

Photocatalysts	Synthesis method	Light source	Sacrificial agents	Activity	Other variables	Refs.
1T-MoS_2 and N-doped 2H-MoS_2/graphene	Li-intercalation and hydrothermal methods	100 W Xe lamp	Triethanolamine	0.18 and 0.83 mmol g^{-1} h^{-1}	TOF[a]): 6.25 and 2.9	[134]
P25-TiO_2/1T-WS_2 and P25-TiO_2/2H-WS_2	Colloidal method	300 W Xe lamp	Methanol	2570 and 225 µmol g^{-1} h^{-1}		[147]
Si-doped TiO_2/$MoSe_2$ and TiO_2 nanosheets/1T-$MOSe_2$	Hydrothermal method	250 W Xe lamp	Triethanolamine	167.6 and 135.5 mmol g^{-1} h^{-1}		[148]
c-$KNbO_3$ and o-$KNbO_3$	Hydrothermal method	250 W Xe lamp	Methanol	1242 and 677 µmol g^{-1} h^{-1}	AQY (%): 1.95 and 1.2	[150]
TiO_2 NS (high {100} facet exposed) and TiO_2 cuboids NS (less {100} facet exposed)	Hydrothermal method	300 W Xe lamp	Methanol	362 and 79 µmol g^{-1} h^{-1}		[149]
o-$KNbO_3$, t-$KNbO_3$ and c-$KNbO_3$ microcubes	Hydrothermal	300 W Xe lamp	Methanol	333, 118, and 1242 µmol g^{-1} h^{-1}	AQY (%): 0.53, 0.16, and 1.95	[66]
1T-MoS_2/CdS NRs and 2H-MoS_2 NRs	Hydrothermal and lithium intercalation	300 W Xe lamp	Lactic acid	794.93 and 175.82 µmol g^{-1} h^{-1}		[53]
1T-Li_xMoS_2/$ZnIn_2S_4$ and 2H-MoS_2/$ZnIn_2S_4$	Hydrothermal	300 W Xe lamp		332.4 and 241.6 µmol g^{-1} h^{-1}		[140]
c-$KNbO_3$ and o-$KNbO_3$	Furfural-alcohol-derived polymerization-oxidation	300 W Xe lamp	Methanol	127 and 72.3 µmol g^{-1} h^{-1}		[143]
1T-MoS_2/O-g-C_3N_4	Solvothermal	500 W Xe lamp	Triethanolamine	1841.72 µmol g^{-1} h^{-1}	QE (%) = 7.11, and TOF = 156.6 h^{-1}	[11]
1T′-$Mo_{(1-x)}$ W_xS_2/CdS	Hydrothermal	300 W Xe lamp	Lactic acid	56.53 mmol g^{-1} h^{-1}		[151]
CdS:1T-MoS_2 and CdS:2H-MoS_2	Hydrothermal	300 W Xe lamp	Lactic acid	440 µmol g^{-1} h^{-1} and 3.07 mmol g^{-1} h^{-1}		[136]
1T-MoS_2/CdS-ZnS QDs	Self-assembly		Na_2SO_4	155 ± 3.5 mmol mg^{-1} h^{-1}		[152]
MoO_3/1T-MoS_2/g-C_3N_4	In situ sulfuration	300 W Xe lamp	Triethanolamine	513 µmol g^{-1} h^{-1}		[153]
Hexagonal@ cubic CdS core@shell nanorod	Hydrothermal	300 W Xe lamp	Na_2S (0.35 M) Na_2SO_3 (0.25 M)	742.5 µmol h^{-1}	Stability for 400 h	[154]

[a]Turnover frequency (TOF) is determined for each catalyst was calculated per mole of MoS_2 present in each catalyst, considering the fact that H_2 evolution happens on MoS_2 only.

character. To stabilize the 1T phase, electrons must be pumped electrons into it, which in turn causes it to become metallic in nature due to the half-filled d-orbital band. The introduction of distortions and/or defects in the structure of TMD materials gives rise to different properties; for instance, $1T-MoS_2$ displays conductivity that is a factor of 10^7 higher than the conductivity of its counterpart 2H phase. Maitra et al.[134] have demonstrated that the hydrogen evolution activity of single-layered $1T-MoS_2$ photocatalysts is higher than that of nitrogen-doped graphene $2H-MoS_2$. This is likely because reduced graphene as an electron transporter to MoS_2 increases the metallic conductivity of MoS_2 itself. The HER activity over single-layered $1T-MoS_2$ photocatalysts suggested the formation of a p–n junction in composites of n-type N-doped graphene with p-type MoS_2. It is worth noting that in the overall reaction scheme for the photocatalytic generation of hydrogen, the electron involved in the reduction process does not photocatalytically form on the MoS_2 surface but is transferred from the photogenerated species eosin (EY^-) to MoS_2. Additionally, Xu et al.[11] have designed the metallic $1T-MoS_2$ phase as a cocatalyst on 2D oxygenated $g-C_3N_4$ semiconductors using the in situ growth method for PC-HER activity. Among the prepared photocatalysts, $1T-MoS_2/O-g-C_3N_4$ shows outstanding photocatalytic performance, where the highest H_2 evolution rate was reported at approximately 1841.72 µmol g^{-1} h^{-1} for optimum $1T-MoS_2$ loading. At $\lambda = 420$ nm, the external quantum efficiency of the 0.2% $1T-MoS_2/O-g-C_3N_4$ 2D heterostructure was ≈7.11%, which is the highest value of all $g-C_3N_4$-based systems using Pt-free cocatalysts. For such outstanding photocatalytic performance, the possible reasons outlined were that the exposed edges and basal plane could be catalytically active for both photocatalysts, while the decreased contact layer between the $1T-MoS_2$ phase and $O-g-C_3N_4$ semiconductors facilitated the photoinduced electron transfer from the conduction band to the $1T-MoS_2$ phase, in turn increasing the participation of electrons in PC-HER. Moreover, the designed 2D heterostructure junction of 2D semiconductor-supported 2D metals through van der Waals interactions minimizes the Schottky barrier or even eliminates this barrier because of weak Fermi-level pinning, which is an important factor for improving charge transfer on the surface.

Nevertheless, Zeng et al.[7] have identified that an effective photocatalytic HER might be achieved through structural engineering of the phase junction between triazine-based crystalline carbon nitride ($tri-C_3N_4$) and tri-s-triazine-based crystalline carbon nitride ($tri-s-tri-C_3N_4$). In fact, the $tri-C_3N_4$ composite is vertically aligned on the surface of $tri-s-tri-C_3N_4$, which is crucial for achieving a photocatalytic H_2 evolution activity of 144 µmol h^{-1}, which is 30-fold higher than that of pristine $g-C_3N_4$. The reason for the increased activity is the formation of tight crystalline junctions between these two composites, which significantly boost the transfer and separation efficiency of the photocatalytic charge carriers. Because of this tuned property, more charge carriers can diffuse a longer distance on the junction area for directional separation. In addition, Yi et al.[135] have experimented with the metallic $1T-WS_2$ phase as a cocatalyst on 2D graphitic carbide nitride ($g-C_3N_4$) using a facile solvothermal approach for improving photocatalytic hydrogen evolution. As expected, the composite materials show an impressive performance compared with the bare $2D-C_3N_4$

and $2H-WS_2/2D-C_3N_4$ photocatalysts. The documented reasons were the excellent electrical conductivity through the designed p–n junction and improved active sites on the basal plane rather than exposed edge sites of the fabricated photocatalysts. The authors engineered the $1T-WS_2$ phase into the $2H-WS_2$ phase via a thermal annealing treatment route, however, its performance remains questionable. The phase conversion of the $1T-WS_2$ phase (64.1% concentration of 1T phase) at 400 °C shows a H_2 evolution rate of ≈331.09 µmol g^{-1} h^{-1}, which is almost 43.3- and 1.94-fold higher than that of the bare $2D-C_3N_4$ and $2H-WS_2/2D-C_3N_4$ photocatalysts. The 1T phase concentration decreases from 64.1% to 48.7% and 25.7% as the annealing temperature decreases from 400 °C to 300 °C to 200 °C, respectively, while the H_2 evolution rate also decreases from 331.09 to 208.69 µmol g^{-1} h^{-1} and 171.51 µmol g^{-1} h^{-1}. This photocatalyst provides an external quantum efficiency of ≈1.12% at a wavelength of 420 nm, indicating that the $1T-WS_2$ phase can accelerate the charge transfer to the surface and reduce the overpotential barrier for reactions to occur.

Because of their distinctive phase-engineering nature, MoS_2 materials show excellent stability and high efficiency for hydrogen evolution. Liu and co-workers[136] have investigated hydrogen evolution over metallic $1T-MoS_2$ hybrids at the gram scale using a hydrothermal synthetic pathway. The structural phase transition occurs from $2H-MoS_2$ to $1T-MoS_2$ with NH_4^+ ions employed as an electron source, while the application of alkali metals for this purpose was deliberately avoided. The elucidated reason is the long-term stability of the $1T-MoS_2$ phase because Li^+-intercalated products show limited stability. Coupled with a CdS nanorod semiconductor, the fabricated nanocomposites exhibit the highest hydrogen yield of 9.11 mmol g^{-1} h^{-1} with a 300 W Xe light source compared to that of pristine CdS nanorods and $2H-MoS_2/CdS$ nanocomposites, which give 440 µmol g^{-1} h^{-1} and 3.07 mmol g^{-1} h^{-1}, respectively. Interestingly, the $1T-MoS_2/CdS$ nanocomposite displayed prolonged durability even after five reuse cycles. The prime argument for such PC-HER performance with the $1T-MoS_2/CdS$ nanocomposite is the rapid charge transfer ability. However, according to theoretical assumptions, the authors indicated that the metallic nitrogen-doped MoS_2 structure as a cocatalyst could be more effective for improved hydrogen activity than the chosen semiconductors because such doping could speed up the electron–hole separation efficiency and create more active sites. In complementary works by the same authors, the $1T-MoS_2/CdS$ nanocomposite was prepared from a facile one-step solvothermal approach. The maximum hydrogen generation rate of 17.479 mmol g^{-1} h^{-1} was observed with an optimum loading of 0.2 wt% $1T-MoS_2$ on a CdS semiconductor, exhibiting a 39-fold higher value in terms of photocatalytic activity than that of pristine CdS nanorods. What is significantly striking here regarding the increased photocatalytic performance of the CdS nanorod semiconductors is that the synergistic effects stem from the intimate heterojunctions between the interfaces and rapid electron transport in the metallic phase of $1T-MoS_2$.[137]

Du et al.[53] have synthesized $1T-MoS_2/CdS$ NRs and $2H-MoS_2/CdS$ NR hybrids with various phases of MoS_2 nanosheets using hydrothermal methods. With a 10 wt% $1T-MoS_2/CdS$ nanorod heterojunction, the hydrogen generation

rate was 794.93 μmol g^{-1} h^{-1}, which was ≈35-fold and 4.5-fold higher than that of pristine CdS nanorods (22.51 μmol g^{-1} h^{-1}) and 2H-MoS$_2$/CdS nanorods (175.82 μmol g^{-1} h^{-1}), respectively. Nevertheless, loading more than 10 wt% 1T-MoS$_2$ nanosheets might be deleterious because the photocatalytic performance decreases gradually with the CdS nanorods with increasing light shielding by MoS$_2$. Evaluation of the photocatalytic durability reveals that the addition of 1T-MoS$_2$ and 2H-MoS$_2$ has the potential to alleviate photocorrosion even after 12 h of light irradiation. However, the reaction mechanism indicates that the interface between 1T-MoS$_2$ and CdS easily forms an Ohmic contact, which is able to reduce the contact resistance and increase the steady photoexcited electron transfer; therefore, 1T-MoS$_2$ could be considered an excellent cocatalyst for facilitating the CdS photocatalyst activity.

Wu et al.[138] have engineered different phases of the MoS$_2$ sample on a g-C$_3$N$_4$ semiconductor to accelerate the electron–hole pair separation and boost the hydrogen evolution rate. A 0.2 wt% 1T-MoS$_2$/g-C$_3$N$_4$ nanojunction presents the highest hydrogen evolution rate of 948.7 μmol g^{-1} h^{-1}, which is almost 26-fold and 83-fold higher than that of the 2H-MoS$_2$ phase and pristine g-C$_3$N$_4$, respectively, under the same experimental conditions. It is possible that g-C$_3$N$_4$ possesses a highly defined and unambiguous structure with minimal thickness, large aspect ratios, homogeneous tri-s-triazine-based units, and high crystallinity.[139] However, the combination of 1T-MoS$_2$ and g-C$_3$N$_4$ could serve as a feasible photocatalyst for hydrogen evolution because of its rapid charge pair separation, and the composites themselves do not decompose under controlled experimental conditions. Preparing nanocomposite junctions

with 1T-MoS$_2$ and other compounds may uncover the true intrinsic performance of photocatalysts for HER. Believing that speculation, Liu et al.[140] have prepared a 1T polymorph of MoS$_2$ on zinc indium sulfide (ZnIn$_2$S$_4$) surfaces by means of lithium intercalation using hydrothermal methods. Due to the presence of lithium ions, the phase structure of the MoS$_2$ samples changes from 2H to 1T. The photocatalytic activity is attributed to the quantity of engineered 1T-MoS$_2$ phase in the composites. A 2.0 wt% 1T-MoS$_2$/ZnIn$_2$S$_4$ composite exhibits a hydrogen formation rate of 332.4 μmol h^{-1}, which is 2.4- and 1.3-fold higher than that of the bare ZnIn$_2$S$_4$ and 2.0 wt% 2H-MoS$_2$/ZnIn$_2$S$_4$ composites, respectively. The reason is likely that the photoinduced electron–hole pairs on the ZnIn$_2$S$_4$ surfaces can easily be isolated in the presence of the 1T-MoS$_2$ phase because of the increased electrical conductivity and high-volume active sites.

The integration of 2H/1T′-MoS$_2$/graphene photocatalysts in both lateral and vertical directions by means of supercritical carbon dioxide treatment provides an excellent performance rate for hydrogen evolution, where graphene functions as an electron acceptor and transporter in the heterostructures. The band position between the two MoS$_2$ phases effectively promotes shifting of the electrons from the 1T′-MoS$_2$ phase to the 2H-MoS$_2$ phase to fill the photoinduced photoholes via the lateral heterojunction structure, which in turn reduces the recombination process between the charge carriers, as shown in **Figure 9**. It is worth noting that a higher photocurrent density for HER was observed.[141] However, the reported synthesis protocols are questionable because it is unclear how exactly this heterostructure was fabricated to ensure that graphene
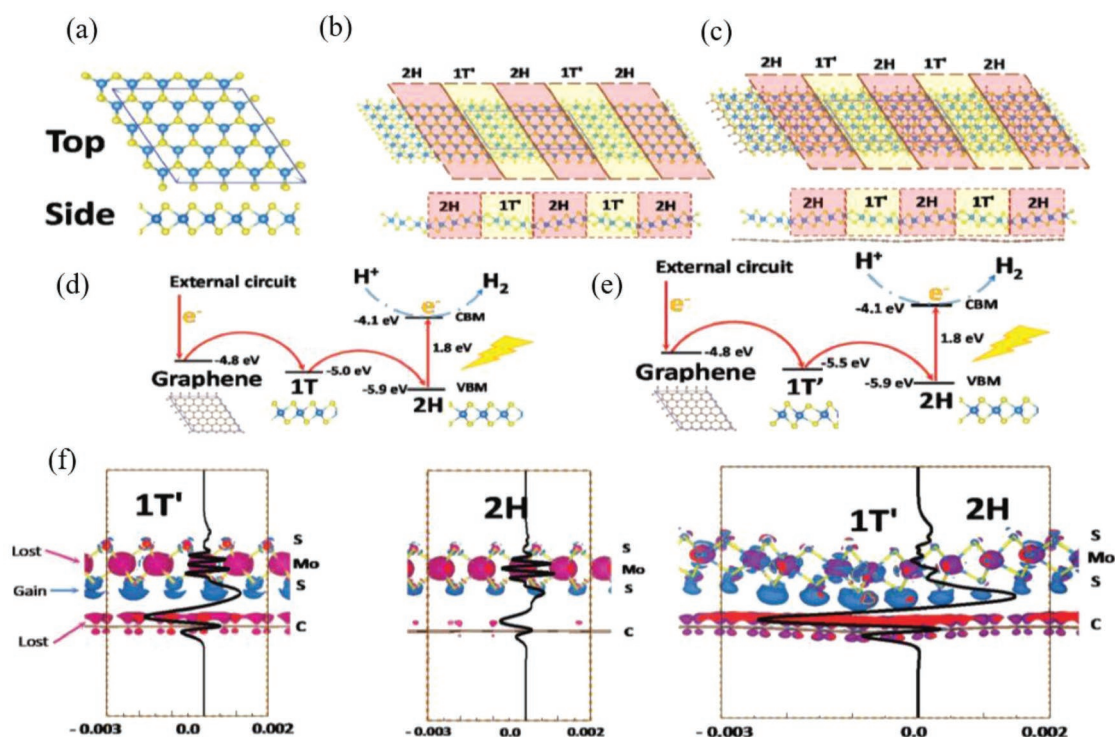
Figure 9. a–c) Structural representation of 2H-MoS$_2$ (a), 2H-/1T′-MoS$_2$ (b), and 2H-/1T′-MoS$_2$/graphene (c) photocatalysts. d,e) Band alignment of graphene, 1T-MoS$_2$ (1T′-MoS$_2$) and 2H-MoS$_2$ according to DFT calculations along with electron flow during the reactions, and f) charge density differences between 1T′-MoS$_2$, 2H-MoS$_2$, or 2H-/1T′-MoS$_2$ and the graphene due to the electronic coupling. a–f) Adapted with permission.[141] Copyright 2017, Wiley-VCH.

was selectively heterointerfaced with 1T′-, not 2H-MoS$_2$, and as designed, this system needs to be further investigated. In a separate study, Chou et al.[51] have evaluated the structural exfoliation of MoS$_2$ by means of lithium intercalation and demonstrated how varying the physical structure can impact HER photocatalysis.

Computational studies reveal that with increasing lithiation, the Mo atoms of MoS$_2$ become asymmetrically spaced, resulting in the generation of the 1T′ phase, which causes the normally inactive basal plane to be prone to hydrogen adsorption and hydrogen evolution. Additionally, the monolayer exfoliation enhances the surface area by as much as 1000-fold, which is beneficial because the basal plane activation gives nontrivial enhancement in catalytic performance compared with exposed edge site-dominated catalysis of the 2H-MoS$_2$ phase. Such an enhancement strategy with MoS$_2$ samples affords a fourfold increase in hydrogen yield.[141]

The 2H-MoS$_2$ phase is a semiconductor with a narrow bandgap, i.e., 2 eV, while the metastable metallic 1T-MoS$_2$ and quasi-metallic 1T′-MoS$_2$ show higher electric conductivity. The 2H-MoS$_2$ phase is regarded as photocatalytic, but its slow electron transfer in the MoS$_2$ plane makes it unfeasible for wider applications because such a property encourages electron–hole pair recombination and thus reduces the photocatalytic activity. Chang et al.[45] have prepared different phase-based MoS$_2$ samples using lithium molten salt intercalation at different temperatures. They performed photocatalytic hydrogen evolution over these samples and reported that a hydrogen yield of 1563.6 µmol g^{-1} h^{-1} with the corresponding apparent quantum efficiency of 24.1% at 420 nm was achieved with the 1T-MoS$_2$ phase, while the 2H-MoS$_2$ phase yielded ≈1658.5 µmol g^{-1} h^{-1} of hydrogen. The higher photocatalytic activity of the 2H-MoS$_2$ samples on the CdS semiconductor was linked to its smaller particle size compared with that of the 1T-MoS$_2$ phase. Additionally, the photocatalytic activity is differentiated with respect to CdS and TiO$_2$ semiconductor band matching with that of the MoS$_2$ samples. Because of the quantum confinement effect, the monolayer 2H-MoS$_2$ samples have a larger bandgap (1.3 eV) than that of the corresponding bulk MoS$_2$, where the minimum position of its conduction band (CB) is more negative than that of TiO$_2$. From a theoretical perspective, it might be improbable that a photoinduced electron from TiO$_2$ can enter the CB of 2H-MoS$_2$ samples for hydrogen reduction. Conversely, the photoexcited electrons can easily inject into both 1T- and 2H-MoS$_2$ for the hydrogen evolution reaction due to the more negative CB position of CdS, as shown in **Figure 10**.

PC-HER on Heterophases: To improve photocatalysis, it is necessary to fabricate intraplane heterojunctions because the different phases of MoS$_2$ exhibit diverse physical and chemical properties. A literature survey indicates that design and fabrication of the 1T/1T′-phase MoS$_2$ along with the 2H-MoS$_2$ phase in the same plane might be beneficial for reducing the charge recombination process because the rapid photogenerated electrons and holes can transfer from the latter phase to the former phase. Based on these ideas, multiphasic single-layer MoS$_2$ was developed, and it was found that it works well owing the 2H-MoS$_2$ phase, which absorbs visible light and creates charge pairs while the photoinduced charge pairs are separated via intimate contact between the 1T/1T′-phase MoS$_2$ and 2H-MoS$_2$ phase.[142] More specifically, at the interface of the n-type semiconducting 2H-MoS$_2$ and 1T′-MoS$_2$ phases, an upward band-bending Schottky barrier was formed, through which photogenerated electrons flowed from 2H-MoS$_2$ to 1T′-MoS$_2$. The hydrogen evolution reaction occurs on both the basal and edge sites of the 1T′-MoS$_2$ phase along with the edge sites of the 2H-MoS$_2$ phase, resulting in a fourfold higher hydrogen evolution rate than that of the pure 2H-MoS$_2$ phase. The designed heterostructure interface between the 1T′-MoS$_2$ phase and the 2H-MoS$_2$ phase is shown in **Figure 11**.

PC-HER on Multiphases: The phase engineering of nano- and microcrystalline photocatalysts in terms of their physical and optical properties could represent an emerging approach to enable highly effective water splitting for hydrogen generation. It is worth noting that the various crystallographic and electronic structures result in distinct effective masses of photogenerated carriers, their mobility, electron–hole pair recombination, etc., leading to different photocatalytic performances of dissimilar phases. Relationship studies between crystal structure and electronic structure are crucial because crystallographic symmetry has a major influence on photogenerated charge-carrier excitation and their transfer to the catalytic surface. In photocatalysis, NaNbO$_3$ is known as a highly stable and multiphase perovskite, which has been proven to be a competitive candidate for hydrogen generation under light irradiation. Li et al.[143] have prepared cubic-phase NaNbO$_3$ (c-NaNbO$_3$) and orthorhombic-phase NaNbO$_3$ (o-NaNbO$_3$) to understand the synergistic relationship between their electronic structure and photocatalytic properties. Hydrogen evolution was calculated to be ≈127 and 72.3 µmol h^{-1}, respectively, for c-NaNbO$_3$ and o-NaNbO$_3$ under a 300 W Xe lamp at λ > 300 nm. Possible reasons for the different reactivity's are ascribed to their different electronic structures. In parallel works, Zhang and co-workers[66] have studied the photoreactivity of temperature-dependent crystalline phases such as cubic KNbO$_3$ (c-KNbO$_3$), orthorhombic KNbO$_3$ (o-KNbO$_3$), and tetragonal KNbO$_3$ (t-KNbO$_3$) from aqueous methanol under UV irradiation. With a small amount of Pt cocatalyst, the c-KNbO$_3$ phase provides ≈1242 µmol h^{-1} g^{-1} of hydrogen at a quantum efficiency of 1.95%, while 333 µmol h^{-1} g^{-1} of hydrogen at a quantum efficiency of 0.53% was reported for the o-KNbO$_3$ phase, and 118 µmol h^{-1} g^{-1} of hydrogen at a quantum efficiency of 0.16% was reported for the t-KNbO$_3$ phase. The higher photocatalytic performance achieved with the c-KNbO$_3$ phase than that with the o-KNbO$_3$ and t-KNbO$_3$ phases is because of the high symmetry number in the bulk structure and the associated unique electronic structure. In addition, the improvement in either the charge-carrier lifetime or the electron transfer rate constant at the interfaces caused the high quantum efficiency, which is perhaps regulated by the electronic structure of the KNbO$_3$ perovskite sample. A recent computational study[144] revealed that the c-KNbO$_3$ phase has the largest electron mobility, a smaller electron effective mass of photoinduced electrons, a lower electron hole pair recombination rate and a much better light absorption capacity compared to those of the o-KNbO$_3$ and t-KNbO$_3$ phases. Therefore, the photoreactivity of the cubic phase should be higher than that of the other phases. Similarly,
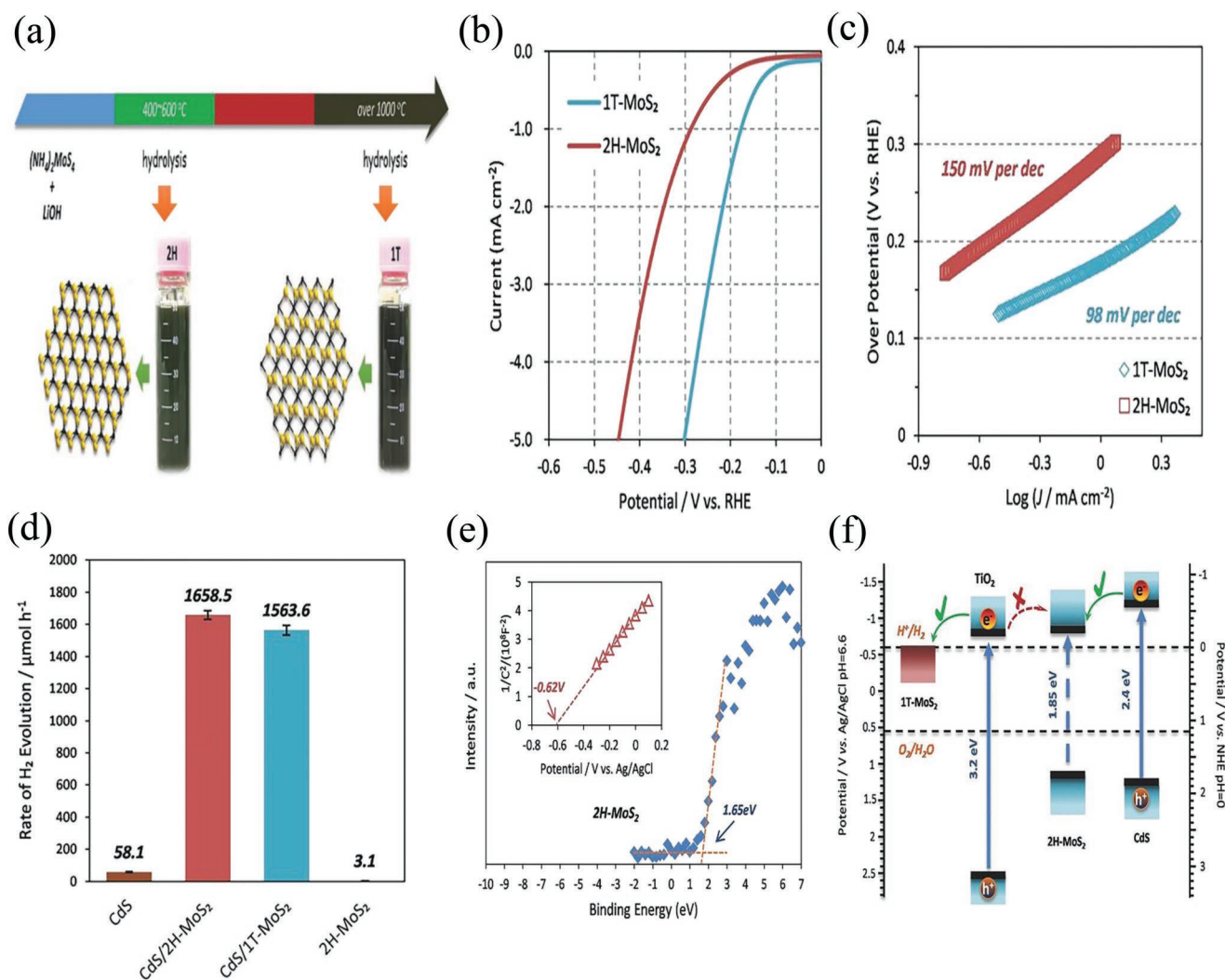
Figure 10. a) Schematic illustrations of hydrolysis exfoliation of 2H and 1T MoS_2 at different calcination temperatures. b) Linear sweep voltammograms (LSV) (5 mV s^{-1}) for MoS_2 films on FTO substrates, comparing the electrocatalytic response toward HER. The measured potentials were subjected to *iR* correction, and the supporting electrolyte was 0.5 M H_2SO_4 aqueous solution. c) Overpotential versus current density plots showing Tafel slopes expressed as mV per decade. d) Photocatalytic H_2 evolution activities of 1T- (MoS_2-1000) and 2H-phase MoS_2 (MoS_2-400) over commercial CdS. e) Valence band XPS (VB-XPS) spectrum of 2H-MoS_2. The inset shows the corresponding Mott-Schottky plots in 0.5 M Na_2SO_4 aqueous solution. f) Schematic energy-level diagrams of 1T-, 2H-MoS_2, TiO_2, and CdS in comparison with the potentials for water reduction and oxidation. a–f) Adapted with permission.[45] Copyright 2016, Wiley-VCH.

Chang et al.[145] have investigated the multicrystalline phases of Cu_2ZnSnS_4 (CZTS) chalcogenide semiconductors for hydrogen evolution under UV–vis irradiation. The wurtzite CZTS phase produces 21.2 µmol h^{-1} g^{-1} of hydrogen, while the kesterite CZTS phase yields 54.8 µmol h^{-1} g^{-1} of hydrogen, which is approximately threefold higher than that of the wurtzite CZTS phase. The kesterite CZTS phase remains stable for up to three 12 h cycles. It was clarified that the improved photocatalytic activity over CZTS is correlated with the band position of kesterite and wurtzite CZTS and the phase composition. The surface atomic configuration and different electronic structures (band structures) in different phases are responsible for the enhanced photocatalytic performance. Both kesterite and wurtzite CZTS have a direct bandgap in nature, while the CB and VB of kesterite CZTS are more dispersive, indicating that

this phase possesses lighter effective masses than the wurtzite CZTS phase does.[145] As a result, kesterite CZTS exhibited faster electron and hole migration abilities on the surface. Additionally, the dominant exposed facets of kesterite CZTS are {112} facets, which are polar and unstable facets with alternating cation and anion layers. Such instability of kesterite CZTS increases its ability to absorb cations and/or anions, which can compensate for the charge imbalance. On the other hand, wurtzite CZTS shows {100} sidewalls, representing a cation–anion parallel alignment surface. Overall, kesterite CZTS shows phase-dependent photocatalytic performance for H_2 evolution. Structural phase materials can be used not only to promote electron–hole separation during photocatalysis either by electron or hole trapping but also to supply sufficient reactive catalytic sites for redox reactions. The application of
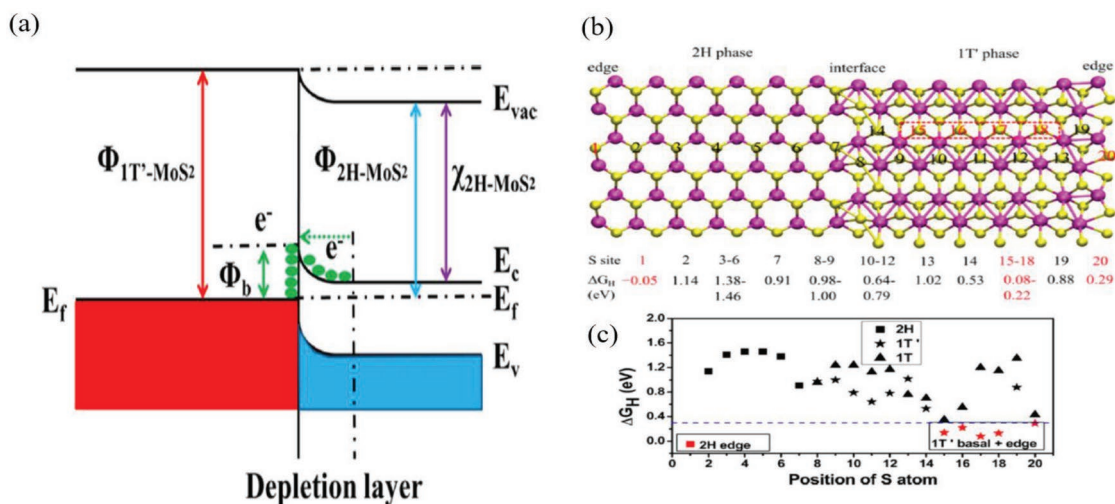
**ADVANCED
SCIENCE NEWS**

www.advancedsciencenews.com

**ADVANCED
MATERIALS**

www.advmat.de

Figure 11. a) Representation of multiphasic heterojunction between 1T′ and 2H phase of MoS_2. b) Schematic of 1T′–2H heterojunction. c) Simulated Gibbs free energy, ΔG_H against S atom position in 1T′–2H and 1T–2H heterojunctions. a–c) Adapted with permission.[142] Copyright 2016, American Chemical Society.

structural phase materials as cocatalysts has a significant influence on the photocatalytic performance since they can boost interfacial charge transfer, thereby facilitating surface reactions as well. However, a proper band alignment between the cocatalysts and the light-harvesting materials is essential to obtain the maximum benefit from the interfacial charge transfer processes. To obtain such alignment, engineering of the structural materials is first needed. For example, structured MoS_2 and WS_2 can be utilized as cocatalysts to improve the photocatalytic activity of the water-splitting reaction for hydrogen production. Bai et al.[146] have prepared hybrid junctions between TiO_2 nanosheets and 1T-MoS_2 nanosheets by means of lithium exfoliation using bulk MoS_2. The authors achieved higher PC-HER activity with the 1T-MoS_2/TiO_2 heterostructure than with its 2H-MoS_2 counterpart. They noted that the 1T-MoS_2 phase increased the number of active sites on the basal plane and edges for hydrogen evolution while providing electron delivery channels. In the 2H-MoS_2 phase, the active sites are

located only at the edges of the nanosheets. On the other hand, the 1T-MoS_2 phase exhibits higher charge transport mobility and has a higher density of reactive sites, making this phase an excellent candidate for photocatalytic H_2 evolution, as shown in **Figure 12**. Therefore, the loading of TiO_2 nanocrystals onto the 1T-MoS_2 phase shortens the electron diffusion distance and increases the diffusion rate compared with that of the TiO_2 loaded over the 2H-MoS_2 phase. As a result, the 1T-MoS_2/TiO_2 heterostructure shows extended photocatalytic activity for H_2 production compared to that of the 2H-MoS_2/TiO_2 phase.

Mahler et al.[147] have developed preparation protocols for making colloidal 2H-phase or 1T′-phase WS_2 monolayers. The as-prepared 1T-WS_2 nanosheets doped by P25-TiO_2 via a simple adsorption method enhance the hydrogen evolution rate by more than threefold to 2570 μmol g^{-1} h^{-1} compared with that of bare P25. **Figure 13**a shows that 1T-WS_2 possesses a high work function, which plays a key role in trapping the photon-induced translocation of the electrons from TiO_2 and
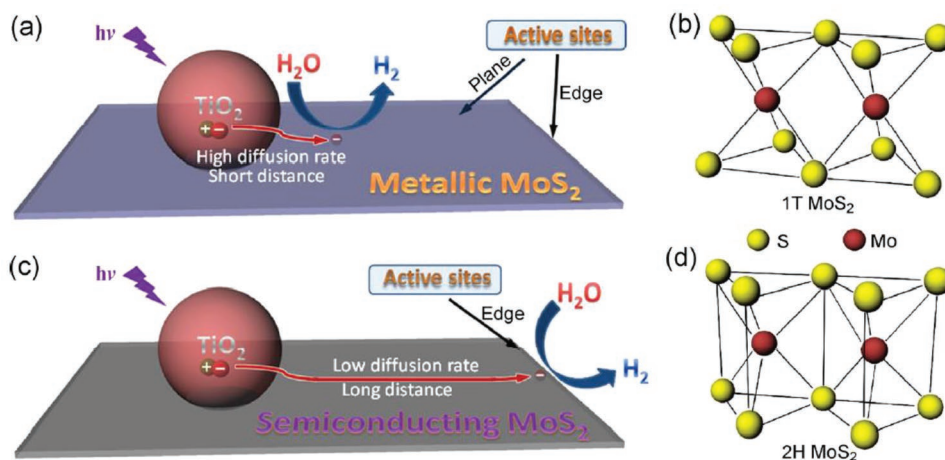

Figure 12. a) Photocatalytic reaction scheme for TiO_2/1T-MoS_2 hybrids structure, and b) crystal structure for 1T-MoS_2. c) Photocatalytic reaction scheme for TiO_2/2H-MoS_2 hybrids structure and d) crystal structure for 2H-MoS_2. a–d) Adapted with permission.[146] Copyright 2015, Springer Science.
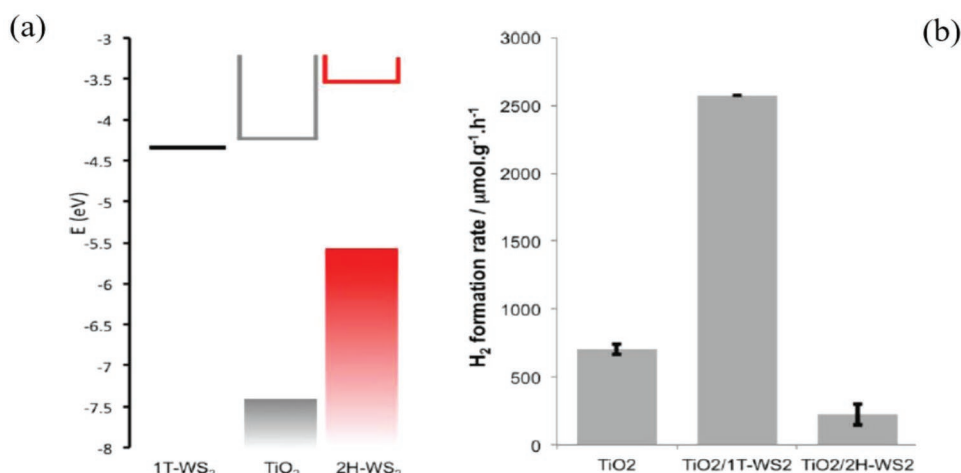
Figure 13. a) Schematic of electronic band alignment between TiO_2 and synthesized 1T-WS_2 and 2H-WS_2 nanostructures. b) Photocatalytic hydrogen production rates for P25-TiO_2 and the TiO_2:1T-WS_2 and TiO_2:2H-WS_2 nanocomposites. a,b) Adapted with permission.[147] Copyright 2014, American Chemical Society.

boosting H_2 production. The semiconducting 2H-WS_2 phase works as a light-harvesting material, which simultaneously provides photoinduced electrons to TiO_2 and supplies recombination centers for photoinduced electrons and holes in TiO_2. The heterostructures with 2H-WS_2, however, reduce the hydrogen evolution rate, as shown in Figure 13b.

Similarly, the presence of 1T-MoS_2 as a cocatalyst afforded higher photocatalytic H_2 activity when coupled with TiO_2, while lower performance was realized with the 2H-MoS_2 phase.[45] In contrast to this finding, it was reported that the photocatalytic performance in terms of H_2 evolution with 1T-MoS_2 was much lower than that with 2H-MoS_2 when loaded with CdS materials. We hypothesize that the CB band position of CdS (bandgap ≈ 2.4 eV) was more negative than that for the 2H-MoS_2 (bandgap ≈ 1.85 eV) and 1T-MoS_2 phases, which readily accelerated the pumping of electrons from CdS to 1T-MoS_2 and 2H-MoS_2. In the TiO_2 case, the CB band position was lower than that of the 2H-MoS_2 phase, making electron transfer to that phase infeasible; rather, the electrons would be transferred to the relatively lower CB of the 1T-MoS_2 phase.[45] He et al.[148] have investigated the photocatalytic performance of silicon-doped TiO_2 nanotubes mixed with 1T-$MoSe_2$ and TiO_2 nanotubes/$MoSe_2$ for hydrogen evolution from light-driven water splitting. The heterojunction between the silicon-doped TiO_2 nanotubes mixed with the 1T-$MoSe_2$ phase exhibits pronounced activity in absorbing intense light and speeds up migration of the electron–hole pair to the surface, which is believed to explain why this material shows higher photocatalytic activity than that of TiO_2 nanotubes. Hydrogen evolution rates of 167.6, 135.5, 0.46, and 0.35 µmol g^{-1} h^{-1} were observed for Si-doped TiO_2 nanotubes/1T-$MoSe_2$, TiO_2 nanotubes/1T-$MoSe_2$, Si-doped TiO_2 nanotubes, and TiO_2 nanotubes, respectively, which indicated the potency of Si-doped TiO_2 nanotubes/1T-$MoSe_2$ as photocatalysts. In a different study, Xu and co-workers have evaluated the TiO_2 anatase phase with different facets, namely, T_{sheets} (95% of facets exposed) and $T_{cuboids}$ (fewer {100} facets exposed), to compare hydrogen evolution from water splitting. The T_{sheets} exhibit a photocatalytic

hydrogen evolution rate (362 µmol h^{-1}) that is almost 4.6-fold higher than that of the $T_{cuboids}$ (79 µmol h^{-1}). Facet reactivity and surface defects can influence photocatalysis. It is worth noting that with more {100} facets exposed on T_{sheets}, more five-coordinate Ti atoms along with oxygen vacancies are available on the surface to function as active sites for water splitting to produce hydrogen.[149]

3.2.2. SPE for Photocatalytic OWS (PC-OWS)

In photocatalysis research, the overall water splitting with the aid of light illumination is not yet fully understood because the complicated and unresolved scientific challenges of the processes create further questions regarding the sustainable and practical implications of this technology.[17] Determining the underlying mechanistic relationships among the surface phases, crystal structure and photocatalytic activity has become one way to address many unsettled issues in PC-OWS.[17,155] As we have shown throughout this review, the surface phase largely affects the photocatalytic activity because the phase junction is likely to improve the electron conductivity and suppress the charge-carrier recombination rate, which we will discuss in depth in the following sections.

PC-OWS on Heterophases: To prevent electron–hole recombination during photocatalysis, it would be very interesting to design and synthesize photocatalytic materials with different phase ratios that can maximize their synergistic effect and enhance the photoactivities of the phase junction. The photoactivity of the phase junction is also affected by the charge transfer processes between the different crystal phases. Therefore, constructing a well-matched and nondefective interfacial structure is highly desirable not only for promoting effective interfacial charge transfer but also for realizing a prolonged lifetime of electrons and holes in photocatalysis. The metal oxide semiconductor Ga_2O_3 has four polymorphs, namely, α-, β-, γ-, and ε-Ga_2O_3, which are highly attractive photocatalysts for the overall water-splitting reaction.[156] Upon calcination,

ADVANCED
SCIENCE NEWS
www.advancedsciencenews.com

ADVANCED
MATERIALS
www.advmat.de

one can convert all other phases into the β-Ga_2O_3 phase, which is the most thermodynamically stable phase.[157] Literature survey indicates that the overall photocatalytic water splitting reaction has been scrutinized deliberately on the α-Ga_2O_3 and β-Ga_2O_3 phases and their mixtures.[158] Jin and co-workers[159] have investigated mixed-phase γ/β-Ga_2O_3 as a photocatalyst to understand the effect of the phase junction on the overall water-splitting reaction. The authors anticipated that mixed-phase γ/β-Ga_2O_3 could drive the photocatalytic activity in a progressive manner due to the accelerated charge separation at the phase junction. Of the prepared samples, the γ-Ga_2O_3 phase along with the $Rh_{0.5}Cr_{1.5}O_3$ cocatalyst exhibits HER and OER activity of 67 and 30 $\mu mol\ m^{-2}\ h^{-1}$, respectively. With the complete conversion of the γ phase into the β phase, considerable photocatalytic activity was attained individually for HER (105.6 $\mu mol\ m^{-2}\ h^{-1}$) and OER (49.3 $\mu mol\ m^{-2}\ h^{-1}$).[159] It was argued that enhancement of the β phase in the samples improved the photocatalytic activity because of the evolution of the disordered structure during the phase transformation. The evolution of the disordered structure is likely to be relevant to the inherently defective spinel structure of the γ-Ga_2O_3 phase rather than the lattice mismatch factor. The formed defects in mixed-phase γ/β-Ga_2O_3 might be helpful in recombining an electron with a donor site favored by an oxygen vacancy and the hole with an acceptor site favored by either a gallium-oxygen vacancy pair or gallium vacancy.[159] However, the contribution from the formed interfaces may yield different results for the overall water-splitting reaction, with the interface between α-Ga_2O_3 and β-Ga_2O_3 as an example. It was posited that the photocatalytic performance at the phase junction of α-Ga_2O_3 and β-Ga_2O_3 was higher than that at the phase junction between γ-Ga_2O_3 and β-Ga_2O_3 since the disordered structure in the γ–β phase junction of Ga_2O_3 provides defect sites that accelerate the charge-carrier recombination processes, negating the expected efficiency for the overall water-splitting reaction.[158]

The formation of α–β phase junctions and the appearance of both phases on the surface are crucial in the proliferation of mobile electrons, thereby increasing the photocatalytic activity. Wang et al.[158] have examined the α–β phase junctions of Ga_2O_3 in water-splitting reactions in the presence of light and noted that the photoactivity was higher than that of standalone α- or β-phase structures. With the α–β phase junctions of Ga_2O_3, the figures of merit reached three- and sevenfold higher than that of the individual α-Ga_2O_3 and β-Ga_2O_3 phases. Moreover, the photocatalytic activity of the α–β phase junction samples was much greater than that of mechanically mixed α-Ga_2O_3 and β-Ga_2O_3 samples, the latter of which had an activity almost equal to the summed individual activities of the α-Ga_2O_3 and β-Ga_2O_3 phases.[158] Considering the microscopic analysis, it was demonstrated that neither the particle size nor surface area was believed to be the reason for achieving high photocatalytic activity, but rather the presence of the α–β phase junction. The formed junctions facilitate ultrafast electron transfer in $\approx$3 ps, which is much more rapid than the recombination (>1000 ps) and trapping processes (14–32 ps). Additionally, the lifetime of the photoinduced electrons in the microsecond timescale at the α–β phase junction is much higher than that of the individual α-Ga_2O_3 and β-Ga_2O_3 phases. The phase junction was beneficial for allowing these long-lived photoinduced electrons

to participate in surface redox reactions, thus increasing the overall photocatalytic activity (**Figure 14**).[158]

However, the highly active α–β phase junction can provide only qualitative information by means of spatial separation of photoinduced electron–hole pairs, leading to a long-lived charge transfer state that is beneficial for OWS. Understanding of the dynamic relationship between the phase junction and its photocatalytic activity is needed, and fabrication and engineering of more effective semiconductor-based photocatalysts may reveal their intrinsic activities. Numerous unanswered questions remain; for example, the effect of lattice misfit and strain of the interfaces on the energy band alignment is far less understood, as is how bonding networks near the interfaces could impact the band mismatch within the charge depletion layer. Ju and co-workers[160] have studied the α–β phase junction theoretically to address these questions because understanding strain-dependent energy band assignment and the bonding networks near the interfaces is crucial in tuning the photocatalytic activity of the junction. The authors used a potential-line-up approach to determine the band alignments of the α–β phase junction of Ga_2O_3 (**Figure 15**). It is evident that the electrostatic potential is localized in the region with a 1 nm width that is parallel to the charge depletion regime, and the asymptotic macroscopic average of the β phase is lower than that of the α phase (0.35 eV). The valence band offsets are much higher than the conduction band offsets (Figure 15). Even if it is too low, the conduction band offset (0.07 eV) cannot be ignored since the lattice strain and mismatch of the two phases is the primary cause of this.[158] The effects of lattice mismatch are significant because atoms induce rearrangement near the interfaces and because phenomena such as defects appear. With small driving forces, the conduction band offset is unable to promote the transfer of electrons across the junction, and an adiabatic mechanism for electron transfer at the interface coupling is suggested.[160] Theoretical analyses indicate that the bandgap between the conduction band and valence band is large enough such that the oxidation potential allows O_2 to be obtained from water oxidation and the reduction potential allows hydrogen to be obtained from proton reduction.[161] The relative energy level position on both sides of the junction is dependent on the band offsets, which account for the confinement potential for charge carriers across the junction and are one of the most important parameters in tuning the photocatalysts. Basically, the offsets are discontinuities between the CB minimum or VB maximum of each semiconductor at the common interface. To fully enable band bending, the catalytic particle size should be less than or equal to twice the width of the space charge region, which describes the bonding network near the interface with respect to the band offsets.

Possessing ultrathin thickness, layered nanosheets have appeared as an emerging class of new materials with a wealth of unusual physical characteristics that are advantageous for increasing both the photocatalytic activity and long-term durability.[162] Zhang et al.[163] have synthesized free-standing single-layered nanosheets of the γ-Ga_2O_3 phase using hydrothermal protocols in the absence of any kind of shape-controlling agents. The surface defects and hydroxyl group passivation are thought to be the primary reasons for the structural stability of single-layered γ-Ga_2O_3 nanosheets. Assessment was carried out

**ADVANCED
SCIENCE NEWS**

www.advancedsciencenews.com
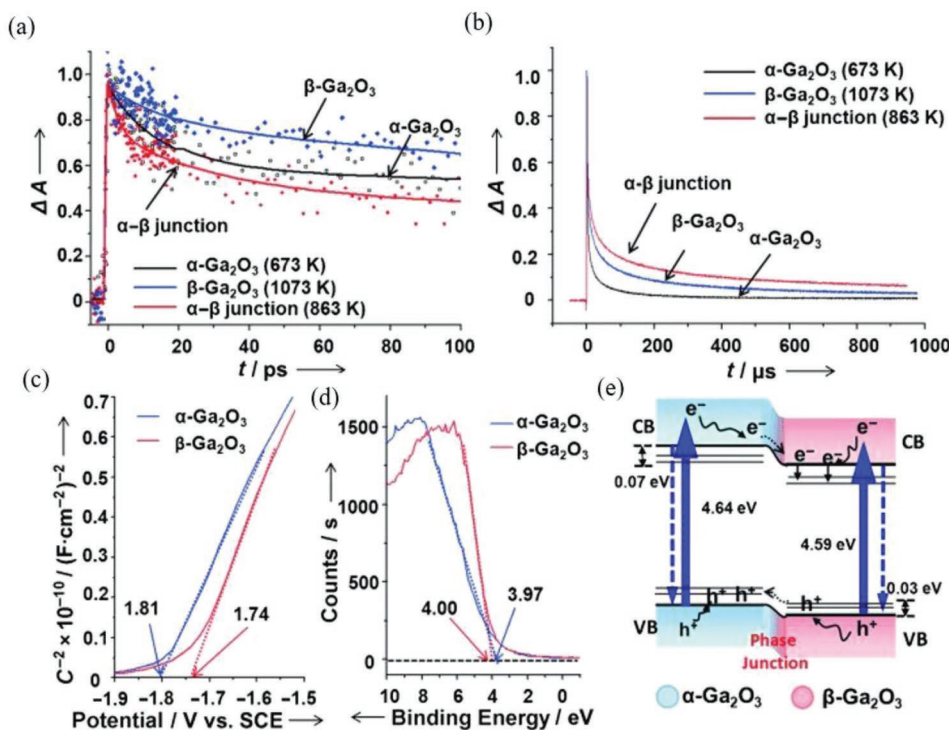
**ADVANCED
MATERIALS**

www.advmat.de

Figure 14. a) Study of transient absorption spectroscopy of Ga_2O_3 samples. Conditions: Wavelength 850 nm, 255 nm laser, pulse duration 50 fs. b) Study of time-resolved IR of Ga_2O_3 samples excited by a 266 nm laser pulse of 6–8 ns duration; α–β junction: Ga_2O_3 with an α–β phase junction obtained by calcining an α-Ga_2O_3 sample at 863 K. c) Mott–Schottky curves of α-Ga_2O_3 and β-Ga_2O_3 electrodes measured in Na_2SO_4 solution (0.3 M, pH ≈7.0). d) XPS valence band spectra of α-Ga_2O_3 and β-Ga_2O_3. e) Illustration of charge transfer cross the α–β phase junction. a–e) Adapted with permission.[158] Copyright 2012, Wiley-VCH.

over the prepared monolayer samples, and 312.5 and 67.5 µmol of hydrogen and oxygen were observed over the course of a 4 h reaction at a controlled pH.[163] The figure of merit of the monolayer γ-Ga_2O_3 phase for PC-OWS was at least onefold greater than that of bulk γ-Ga_2O_3 samples (25 µmol of H_2). The rationale for this activity was related to the ultrathin structure, which enables the shortest diffusion lengths of photoinduced charge pairs and provides a substantial number of active sites due to the large surface area.[163] In addition, the photocatalytic activity of the monolayer nanosheets remained unchanged after three cycle runs. However, the formation rate of oxygen and hydrogen was decreased over the course of the reaction, and the

PC-OWS system was regenerated after evacuation. The reason for the reduced formation rate was the reverse reaction of H_2 and O_2 into H_2O with extended reaction time, representing a further barrier in the formation of H_2 and O_2. The results indicate that the apparent quantum yield of the γ-Ga_2O_3 monolayers is 0.35% at 250–264 nm. Nevertheless, the pH has a significant effect on the surface charge of photocatalysts in inducing electrostatic attraction or repulsion between the catalyst surface and the reactant molecules and subsequently increases or inhibits the photocatalytic reaction rate.[164] In an acidic environment (pH ≈ 3.2), the formation of both O_2 and H_2 decreased significantly, while there was no change in the formation of the
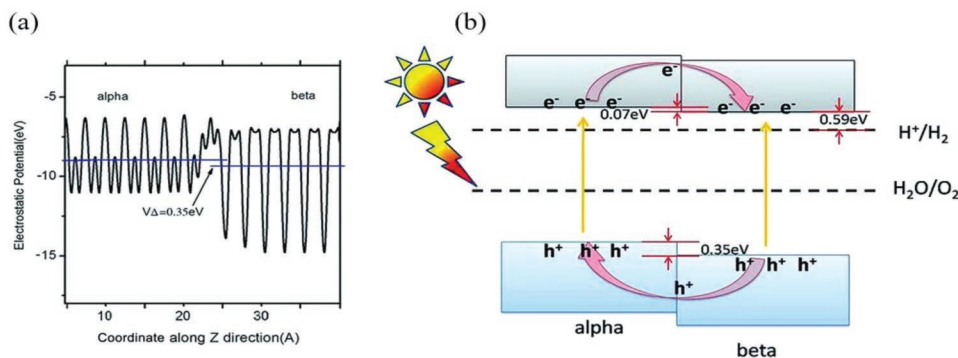

Figure 15. a) The electronic potential profile for α–β phase junction, and b) the band-offset representation. a,b) Adapted with permission.[160] Copyright 2014, The Royal Society of Chemistry.

**ADVANCED
SCIENCE NEWS**

www.advancedsciencenews.com

**ADVANCED
MATERIALS**

www.advmat.de

gases at pH ≈ 10.1. Upon further increasing the pH to 13.2, the gases can form rapidly, the rate of which is comparable to that of neutral solution. This is more likely at high pH values, and the considerable quantity of physisorbed OH^- groups can participate in the photoinduced charge-carrier separation process, which induces involvement of the γ-Ga_2O_3 monolayers in O_2 uptake and hole scavenging to produce oxygen.[163]

PC-OWS on Multiphases: As we discussed previously, TiO_2 has three phases, anatase, rutile, and brookite, where the brookite phase is superior to the other phases in generating H_2 and O_2 in a photocatalytic cell system. Understanding the higher photoelectrical activity with some preferred phases compared to others remains a complex and elusive task, and the scenario is more likely exacerbated for anatase and brookite phases when they are in a photocatalytic system. Li et al.[165] have studied PC-OWS and tested the reactivities of the three phases of TiO_2 semiconductors from both thermodynamic and kinetic standpoints. Neither anatase nor brookite was able to produce H_2 and O_2 under standard experimental conditions, while the contribution of PC-OWS may come from extended UV-light illumination. Clearly, a significant PC-OWS was observed in the rutile phase. The varied results with these phases are caused by the different crystalline nature of these phases. Addressing the questions regarding the inactivity of anatase and brookite hinges on the presence of deep trapped states above the valence band level of TiO_2, which can decrease the potential of photoinduced holes. A two-electron process is much more preferable for photoinduced holes in forming $OH\bullet$ radicals from H_2O molecules than is a direct four-electron process for O_2 production. Upon UV-light irradiation, the abundance of these trapped states is slowly decreased to increase the overpotential for water oxidation and consecutively produce O_2. When considering the rutile phase, there are no trapped states above the valence band level, and hence, there is enough potential for water oxidation and proton reduction.[165]

A phase transition can change the band position from its original point, and this can alternatively be seen as a band edge engineering approach. Scheelite monoclinic $BiVO_4$ (m-$BiVO_4$) is a well-documented photocatalyst with a conduction band edge (CBE) that has a more positive potential than the potential needed for water reduction and is incapable of generating H_2. While this photocatalyst is readily amenable to O_2 evolution under visible-light irradiation due to its proper valence band edge (VBE), its disadvantages, for example, weak surface adsorption properties and poor charge transport characteristics, necessitate further reconsideration of its photocatalytic activity. Jo et al.[40] have attempted to increase the CBE of yellow-colored m-$BiVO_4$ through a phase transition by utilizing both In and Mo dopants, obtaining a greenish-colored $Bi_{1-X}In_XV_{1-X}Mo_XO_4$ compound ($GBVO_X$; X = atom ratio of In and Mo), which in turn has the ability to split water into O_2 and H_2 in the presence of visible light in the absence of any sacrificial reagents. DFT analyses reveal that In^{3+}/Mo^{6+} dual doping induces the phase transformation into a mixed phase of monoclinic $BiVO_4$ and tetragonal $BiVO_4$ from the pure monoclinic $BiVO_4$ phase, which is responsible for an increase in its unit cell volume, compressive lattice strain, and CBE, as well as a widening of its bandgap. The authors explained how this dual doping can influence the H_2 and O_2 evolution rate and noted that there

is an optimum level of doping concentration for both metals that triggers the OER and HER simultaneously; however, the rate-determining step is controlled by the water reduction process. Indeed, the best-performing photocatalyst, $GBVO_{0.10}$, is a mixture of monoclinic (m) $BiVO_4$ and tetragonal (t) $BiVO_4$ phases, where ≈60% is the tetragonal $BiVO_4$ phase. From a surface energy perspective, the formation energies of In^{3+}/Mo^{6+} dopants in m-$BiVO_4$ and t-$BiVO_4$ are 1.31 and 1.79 eV, respectively; the former is independent of lattice strain, and the latter is dependent on cell volume variation. The formation energy of In^{3+}/Mo^{6+} dopants in t-$BiVO_4$ is related to the cell volume, which is 1.407 Å, while the cell volume for m-$BiVO_4$ is 1.253 Å. When the cell volume decreases, the formation energy of In^{3+}/Mo^{6+} dopants in t-$BiVO_4$ decreases, and it even becomes smaller than that of m-$BiVO_4$ with a cell volume less than 1.320 Å. Additionally, when the cell volume decreases below 1.254 Å, the total energy of doped t-$BiVO_4$ decreases compared with that of undoped t-$BiVO_4$. This result further verifies that the change in the formation energy of In^{3+}/Mo^{6+} dopants is accelerated within t-$BiVO_4$ compared with that within m-$BiVO_4$ as the cell volume decreases. Finally, a more stable t-$BiVO_4$ phase can be realized with doping than without doping, which increases the performance of greenish-colored $Bi_{1-X}In_XV_{1-X}Mo_XO_4$ compounds for PC-OWS.

Due to their excellent physical properties, for example, ion exchange, intercalation, and catalysis, Ruddlesden–Popper phases (RPPs), with the generic formula of $(A_2)'$ [$A_{n-1}B_nO_{3n+1}$], have gained considerable attention as photocatalysts for water splitting, where A′ is H or K and A is $La_{2/3}$ or Sr. These layered structural materials utilize their interlayer space as reaction sites, where the electron–hole recombination process could be nullified by the physical isolation of the photoinduced electron and hole pairs.[166] To confirm this hypothesis, Shimizu et al.[167] have prepared a series of RPP hydrous layered photocatalytic materials $H_2La_{2/3}Ta_2O_7$, $K_2La_{2/3}Ta_2O_7$, $H_2SrTa_2O_7$, $La_{2/3}Ta_2O_3$, and $KTaO_3$ for H_2 and O_2 evolution from water splitting. The results indicate that hydrous catalytic materials show superior activity compared to that of anhydrous materials such as $La_{2/3}Ta_2O_3$ and $KTaO_3$, while characterization studies have revealed that the high performance of the hydrous photocatalysts is due to their hydrated layered structure, which can function as a host for photogenerated electrons and holes. Introduction of Ni within the interlayer space increases the activity of $H_2La_{2/3}Ta_2O_7$ materials, while no improvement is observed for $H_2SrTa_2O_7$ catalysts. In fact, the highly dispersed Ni species act as active sites for H_2 evolution during photocatalytic water splitting.

Layered perovskite photocatalysts have proven to be effective in producing hydrogen from water splitting. Li et al.[168] have highlighted a new series of layered perovskite photocatalysts, $ABi_2Ta_2O_9$ (A = Ca, Sr, Ba), while orthorhombic $SrBi_2Ta_2O_9$ catalysts show superior activities compared with tetragonal $BaBi_2Ta_2O_9$ catalysts. Computational studies reveal that the direct-bandgap feature of these catalysts has significant effects on hydrogen production and that the orthorhombic phase is identified as having a greater number of effective states available for the photoinduced electrons and holes. Additionally, Zou et al.[169] have reported a series of novel solid photocatalysts, $BiTa_{1-x}Nb_xO_4$ ($0 \leq x \leq 1$), with different phases such as triclinic

**ADVANCED
SCIENCE NEWS**

www.advancedsciencenews.com

**ADVANCED
MATERIALS**

www.advmat.de

and orthorhombic. In pure water splitting under light irradiation, the authors have found that the triclinic phase shows less activity than that of the orthorhombic phase because the bandgap of the orthorhombic phase is much narrower than that of the triclinic phase. The narrow bandgap more readily promotes exciton transfer from the valence band to the conduction band. In terms of hydrogen production, it was shown that 41 µmol h^{-1} of the product was obtained with a composition of $x = 0.2$, which is one of the studied orthorhombic phases.

3.2.3. SPE for Photoelectrocatalytic OWS (PEC-OWS)

The application of clean inexhaustible solar energy in hydrogen production from overall water splitting is deemed to be a highly attractive approach, while consideration has been given to the development of low-cost and environmentally benign semiconductor materials.[170] To date, a variety of photocatalysts have been employed in this process, and remarkable advancements in this field have been reported. However, a proper narrow bandgap and position are critical criteria in this process, which can be tuned by fabricating and designing the different phase materials. Such a preparative strategy will intensify efficient photogenerated charge separation and migration to reactive sites. In the following section, we will emphasize a variety of phase materials for overall water splitting and discuss their main underlying mechanisms.

PEC-OWS on Single Phases: The merging of both light harvesters and charge-carrier guiders in a single system is known as a photoelectrochemical (PEC) cell, which has shown promising technological effectiveness in utilizing solar energy. The development of PEC cells has been continuously investigated to increase charge separation and transport at the interface.[171] The occurrence of water oxidation or hydroxyl ion formation is necessary in PEC to provide sufficient protons and electrons to support the desired reaction. Substantial research has been directed toward semiconductor-based photoanode and/or photocathode materials to improve the charge-carrier separation and transport; these materials are highly stable and catalytically active for HER and OER and thus enhance the overall water-splitting reaction efficiency. Photoelectrode (anode and/or cathode) materials, however, play central roles in overall water-splitting reactions, which form H_2 and O_2 as products.[172]

To verify the effect of different phases of MoS_2 on the PEC performance, Pi and co-workers[173] have fabricated a 3D photoanode with exfoliated MoS_2 nanosheets on TiO_2 nanorod arrays (TiO_2 NAs) by using both hydrothermal and drop-casting methods. Among the prepared samples, the TiO_2 NAs/1T-MoS_2 composite with an optimized mass loading of the 1T-MoS_2 phase shows a higher photoelectric conversion efficiency than that of TiO_2 NAs/2H-MoS_2 and TiO_2 NAs. A photocurrent density of 1.91 mA cm^{-2} was reported for the TiO_2 NAs/1T-MoS_2 composite, which is far superior to that of the TiO_2NAs/2H-MoS_2 counterpart (1.12 mA cm^{-2}) and TiO_2 NAs (0.42 mA cm^{-2}). The plausible reasons for the improved catalytic performance were ascribed to the strong interaction between the 1T-MoS_2 phase and TiO_2 NAs and the superior conductivity of the 1T-MoS_2 phase. The calculated electrical

conductivity for the 1T-MoS_2 phase was ≈3500 S m^{-1}, while the 2H-MoS_2 nanosheets exhibited an electrical conductivity of only 1.43 S m^{-1}. This finding is in line with the fact that the 1T-MoS_2 phase is metallic, whereas the 2H-MoS_2 phase is semiconducting. Therefore, the photoinduced holes can move into the 1T-MoS_2 nanosheets from TiO_2 NAs, leading to improved separation efficiency. In addition, the TiO_2 NAs/1T-MoS_2 composites have greater endurance than do the other prepared samples. With the TiO_2 NAs/1T-MoS_2 composite, a photocurrent of approximately 1.79 mA cm^{-2} (>92% of the starting current) was observed over the 12 h PEC test, while the value was only 87% for the TiO_2 NAs and 82% for TiO_2 NAs/2H-MoS_2.[173]

A promising technique that has appeared involves tuning the bandgap of metal oxides, in which the O 2p valence orbitals are hybridized with the high-lying valence orbitals of a foreign element, generating shallow valence bands in wide-bandgap metal oxides. Lou and co-workers[174] have studied this technique by inserting Bi^{3+} cations into anodized MoO_3 thin films at a controlled rate, causing the formation of ternary γ-Bi_2MoO_6 thin films along with shallow valence bands and reduced bandgaps, and the authors used them as photoanodes for PEC water-splitting devices. Two phases of ternary γ-Bi_2MoO_6 thin films are associated with the bismuth precursor concentrations and hydrothermal temperature, where a low concentration provides γ(L)-phase Bi_2MoO_6 and a high precursor concentration results in high-temperature-phase γ(H)-Bi_2MoO_6. Characterization studies show that compared with that of MoO_3 ($E_g = 3.4$ eV), the bandgap for both γ(L)-Bi_2MoO_6 and γ(H)-Bi_2MoO_6 is reduced to 2.7 and 3.05 eV, respectively.[174] The reason is likely that the generation of the higher-lying O 2p valence band maximum is the driving force in the bandgap reduction for γ(L)-Bi_2MoO_6, while the hybridization of the Bi 6s orbitals with the O 2p valence orbitals induces the lower valence band maximum potential for the γ(H)-Bi_2MoO_6 thin film. Regarding photoactivity, the highest photocurrent density was observed with the highest γ(L)-Bi_2MoO_6 concentration. The reasons highlighted for this activity were as follows: 1) the formed trilayer Bi_2MoO_6/MoO_3 heterostructure allows smooth entrance of photoexcited charges from the surface generation sites into the charge collection sites at the Mo substrate, thus affording a minimum charge-carrier recombination rate, and 2) the MoO_6 octahedra-coordinated γ(L)-Bi_2MoO_6 has a large conduction band allowing rapid separation and migration of delocalized charges.[174]

An individual search for PEC-OWS was performed by Chemelewski et al.,[175] who prepared amorphous FeOOH (a-FeOOH) catalysts for OER in PEC cells. With 10 nm thick films, the a-FeOOH catalysts display an overpotential of 550 mV to reach 10 mA cm^{-2}, demonstrating good photocatalytic activity. Because of the thinness of the films, they absorb less than 3% of the solar photons (AM 1.5 G) along with energy higher than 1.9 eV and work as a protective layer separating the solution from the solar absorber. In a three-electrode setup, the a-FeOOH/amorphous-Si (a-Si) device attained a total water-splitting efficiency of 4.3% at 0 V versus RHE and maintained its efficiency over the course of 4 h of testing.

PEC-OWS on Heterojunctions: In a PEC system, the charge transport processes between the conducting substrate and catalytic materials are important, necessitating rational fabrication

**ADVANCED
SCIENCE NEWS**

www.advancedsciencenews.com

**ADVANCED
MATERIALS**

www.advmat.de

of the phase junction for the analyzed materials. This consideration carries substantial significance because during the process in which photogenerated charge carriers are transferred from catalytic materials to conducting substrates, a dramatic recombination rate of the photoinduced electrons and holes may occur.[184] In such a case, one can design the phase junction to prolong the lifetime of the photogenerated hole and electrons and thereby improve the photoactivity. We can consider two types of TiO_2 phase junctions for the PEC photoanode: a) rutile nanorods over anatase films and b) anatase films on rutile nanorods along with fluorine-doped tin oxide (FTO) substrates for PEC-OWS.[176] As explained elsewhere, for the phase junction (a), the photocurrent density and onset potential were increased since the photoinduced electrons migrated to anatase films from the rutile nanorods, while a decline in the performance for water splitting over the phase junction (b) was noted, as shown in **Figure 16**.[176] To obtain unidirectional charge-carrier migration and reduce the number of defect sites at the interface, it is thus necessary to tune the phase alignment configuration, which would increase the PEC-OWS performance. Three types of anatase and rutile phase alignment configurations have been considered as photoanodes in the PEC-OWS system: random alignment of various phases (type A), rationally ordered phase alignment (type B), and ordered phase alignment in a reverse configuration (type C).[177] By evaluating the band position, it was concluded that the charge recombination rate was higher in type A and type C than in type B, resulting in improved photocurrent density with type B, as shown in Figure 16. Likewise, the phase junction between the type B system and TiO_2-AR (calcined slowly with

oxygen) exhibited higher performance in terms of charge separation and migration.[177] Apart from this finding, the interface between the type B system and TiO_2-dAR (calcined with oxygen in two steps) slightly enhanced the charge-carrier separation and migration to the reactive sites because of the presence of interfacial dislocations. In such a situation, the CB represents an energy barrier for excess minority carriers so that electrons can migrate to the reactive sites, as shown in Figure 16.[177]

The advantages of structural phase materials would be heightened if one could construct a phase junction by considering the periodic arrangement of various crystal phases along a preferred orientation. The reason is because at the atomic level, the vectorial separation and transfer of photoinduced charge carriers utilizing periodic phase interfaces could improve the photocatalytic performance for H_2 formation. One of the examples in this case would be the twin-induced phase junction between the CdS and $Cd_{1-x}Zn_xS$.[178,179] An examination with $Cd_{0.5}Zn_{0.5}S$ nanorod photocatalytic materials reveals that long-range ordered twinning planes with preferred[111] orientation can be efficient in separating photoinduced charges and contribute to the prolonged lifetime of the photogenerated holes and electrons. Such twinning superlattices can be utilized to obtain other alternating dense homojunctions, such as cubic zinc-blende (ZB) and hexagonal wurtzite (WZ), along that orientation. As shown in **Figure 17**, the boundaries of the twinning $Cd_{0.5}Zn_{0.5}S$ nanocrystals suddenly disrupt the continuity of the ZB lattice structure, while the WZ segment distribution in the ZB lattice was observed. Interestingly, it can be observed that parallel homojunctions such as ZB–WZ–ZB in a real nanocrystal may be realized with periodic arrangement and dense distribution,
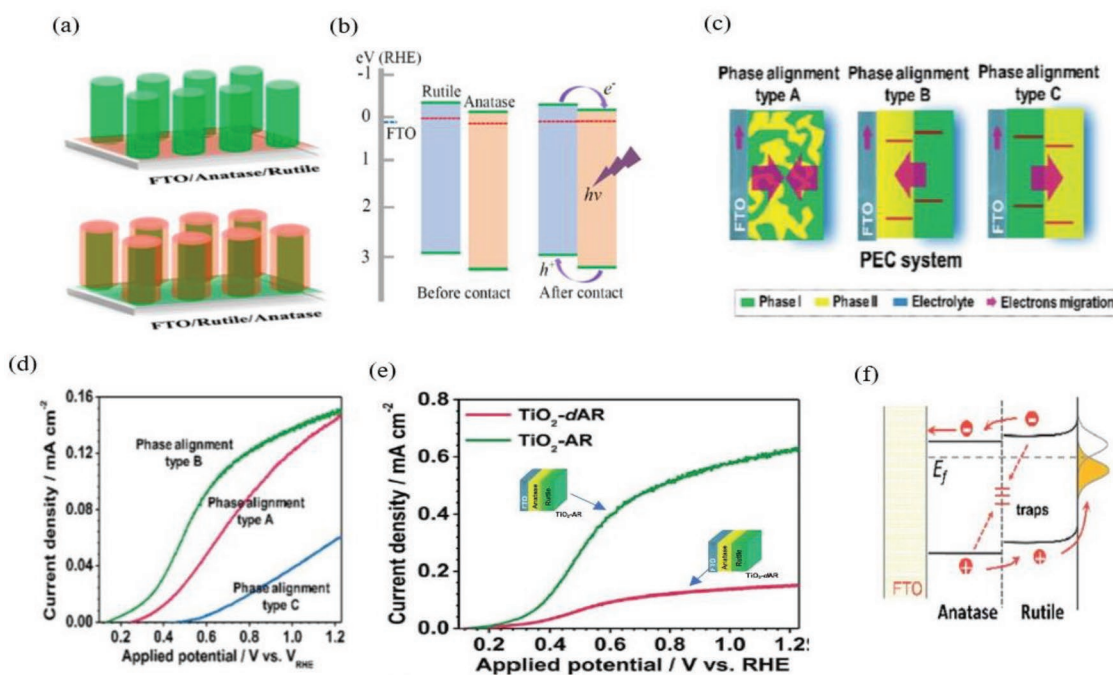

Figure 16. a) Representation of anatase/rutile and rutile/anatase junctions on FTO substrates, and b) their band position before and after contact. a,b) Adapted with permission.[176] Copyright 2016, American Chemical Society. c) Representation of various phase alignment in PEC system along with charge separation and transfer direction. d) CV profile for type A, type B, and type C phase alignment. e) CV profile for TiO_2-dAR and TiO_2-AR photoanode, and f) profile for charge transfer processes over the interfaces. The dotted arrow indicates the undesirable interface trapping or recombination process. c–f) Adapted with permission.[177] Copyright 2016, The Royal Society of Chemistry.
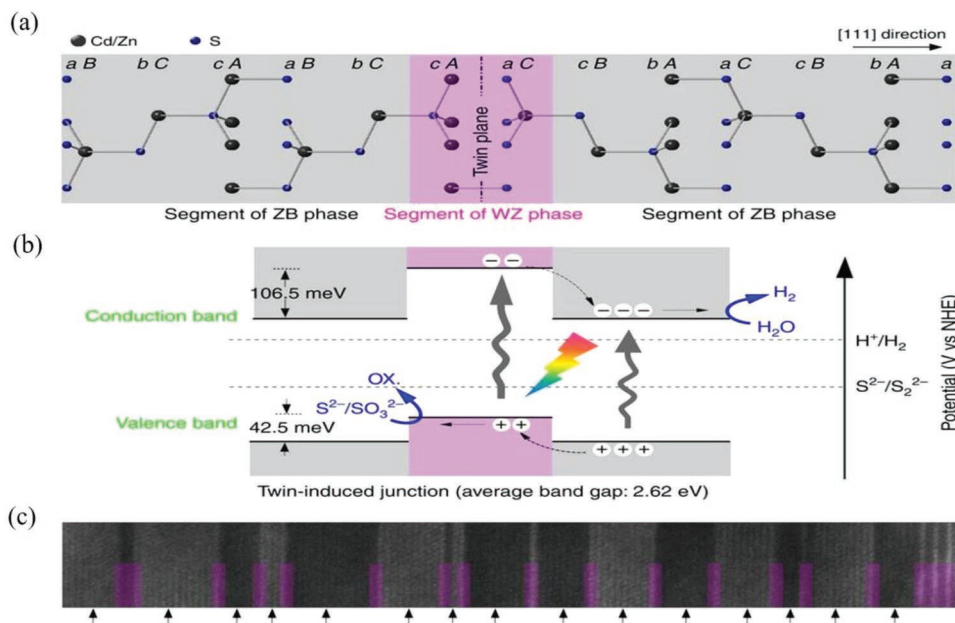
Figure 17. a) Representation of ball–stick structure of a typical twin boundary in a zinc blende (ZB) nanocrystal to form a ZB–WZ–ZB homojunction. b) Profile for charge-transfer processes over the ZB–WZ–ZB homojunction. c) Representation of the parallel homojunctions in a real $Cd_{0.5}Zn_{0.5}S$ nanorod (from TEM image); the black arrows and pink squares represent the segments of ZB and WZ structures, respectively. a–c) Adapted with permission.[178] Copyright 2013, Springer Nature.

as shown in Figure 17b. The upshift of both the CB and VB energy levels for the WZ segment was higher than that for the ZB segment, where the former segment spatially separated the photogenerated holes and electrons from the ZB segment, i.e., away from the twin plane and toward the twin plane on the WZ segments. It is recognized that the built-in interface exhibits Type II staggered band alignment. Therefore, the large distribution and close interconnection of the homojunctions of ZB and WZ at the atomic level is somewhat different from that of other heterogeneous junctions, which can only facilitate the separation of either holes or electrons alone. However, the formation of such homojunctions is responsible for excellent photocatalytic activity in H_2 production by accelerating the vectorial transfer of the photoinduced charge carriers.[178]

3.3. SPE for Photocatalytic Carbon Dioxide Reduction into Energy

The concept of generating valuable chemical fuels from CO_2 reduction under photocatalysis has been adopted over the years and involves multiple electron transfer processes. One of the key assessment parameters in photocatalysis for any given material is the Faradaic efficiency, which dictates that an active catalyst may experience low overpotential to drive the reaction in the forward direction toward the desired products. In the case of CO_2 reduction, it is thus necessary to design photocatalytic materials that have as small of an overpotential as possible while producing a substantial volume of the products. While much effort has been devoted to designing an active photocatalytic material, many aspects remain to be worked out. With an alternating electronic band structure, phase materials have been highly examined in CO_2 reduction, while we note

that many underlying issues remain unresolved. The following section will discuss such challenges and provide some new insights into the reduction of CO_2 into valuable chemical fuels.

3.3.1. SPE for Photocatalytic Carbon Dioxide Reduction (PC-CRR)

We have basically described how HER works with electrochemical and photoelectrochemical approaches, and we intend to rekindle the idea that different phases and their engineering at the atomic scale can amplify photocatalytic activity, thereby improving the end yields as well as the stability. The use of potential semiconductors with appropriate bandgap windows for CRR has been long sought. However, the main mechanism for CRR remains less understood because of its thermodynamic inactivity and the involvement of multielectron (typically 2–12 electrons) reaction processes that depend on the reaction environment.[180]

As shown in **Figure 18**, there are a number of reaction processes involved in PC-CRR. Unlike photodriven water splitting, the CRR proceeds by the incidence of solar energy (photon energy) on the surface of the semiconductor, which should have energy ($E_{h\nu}$) equal to or higher than the bandgap (E_g).[181] The bandgap excitation (photoexcitation) pumps electrons into the CB and holes into the VB, which function as the active sites for photoreduction and photooxidation, respectively. The CB is the lowest energy band where no electron exists at the ground state, and the VB is the highest energy band occupied by electrons. The electron–hole pair can move to the surface, combining at trap sites (recombination process) by means of radiation or nonradiation processes.[182] Additionally, these electrons can move along the semiconductor surface where they can react with surface-adsorbed species, CO_2, but this can only
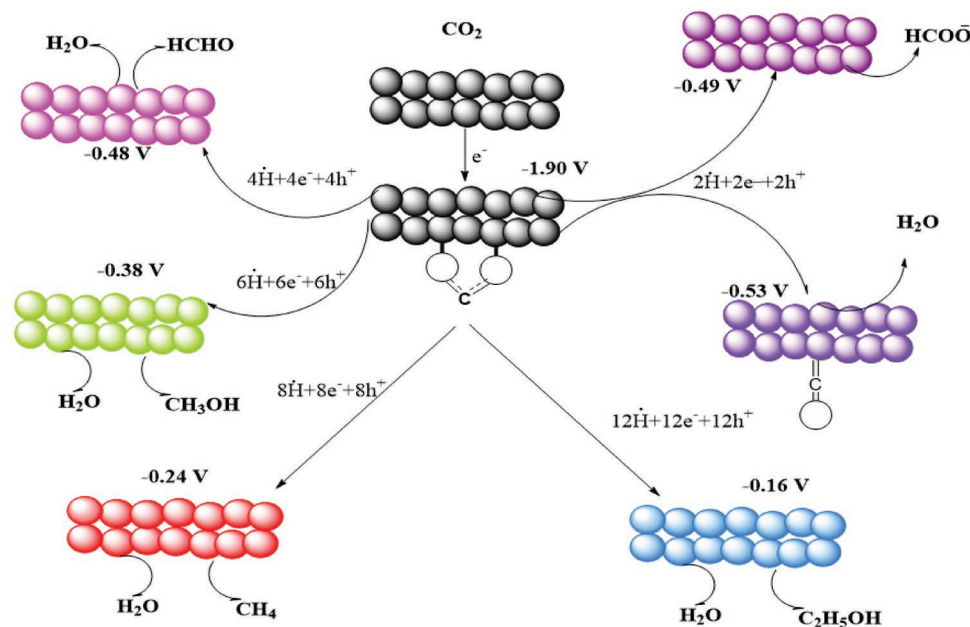
**ADVANCED
SCIENCE NEWS**

www.advancedsciencenews.com

**ADVANCED
MATERIALS**

www.advmat.de

Figure 18. Schematic representation of CO_2 reduction reactions. The negative values adjacent to the products represents the redox potential versus normal hydrogen electrode at pH 7.

be realized when the recombination process is much slower during the transitions.[183] Since CO_2 is thermodynamically very stable and inert, the reduction cannot be performed by all surface-reaching electrons. Apart from contributions by the semiconductor, the catalyst needs to be effective as well, meaning that it should contain electrons with higher energy than that of the reduction potential of CO_2. For an ideal photocatalytic system, the position of the CB should be well above the reduction potential of interest at a controlled pH, while the position of the VB should be well below the oxidation potential of water oxidation. The first step in photocatalytic CO_2 reduction is the formation of electron–hole pairs, i.e., excitons, excited by incident photons. After band excitation, the pairs should be separated spatially with minimization of their recombination, and the separated electrons and holes will activate reduction and oxidation processes, respectively, at the interface. With few-nanosecond lifetimes, the pairs are sufficient to activate and complete the redox reactions, while the time scale of their recombination is two or three times faster than that of other electron processes, which is known as one of the major rate-liming steps.[184] Unlike the ORR, which yields only H_2O or H_2O_2 as a major product, there are many CRR products, such as methane, methanol, carbon monoxide, formate, formaldehyde, and higher hydrocarbons (C_2 and others) and oxygenates. As shown in Figure 18, the potentials for methane and methanol are much lower than that of CO_2, which makes the CO_2 reduction process more favorable from a thermodynamic standpoint. Nonetheless, the kinetic analysis suggests that these reactions are not easy to achieve because they require more electrons, while the products of carbon monoxide, formaldehyde and formic acid can be realized with fewer electrons. In addition, the reactions need 2–8 electrons and protons to obtain the products of interest and must avoid recombination processes. Any photocatalytic process that suppresses electron–hole pair recombination would significantly improve the CO_2 reduction

efficiency.[182] The PC-CRR, however, suffers from low conversion efficiency because of several reasons, including the mismatch between the solar spectrum and absorption ability of the semiconductor and very fast charge-carrier recombinations.[182] Great efforts have been made to improve the matching of the semiconductor bandgap with the solar spectrum by engineering the surface of the semiconductor, changing the phases, defect engineering, doping, and so on.

An important aspect during photocatalysis is the activity of the photoinduced holes because as many holes are produced as electrons in the system. The accumulation of holes on the photocatalyst surface could increase the charge-carrier recombination rate, resulting in a reduction in the electron lifetime. The most destructive role, however, that holes can play is to initiate photocorrosion if they cannot be utilized properly during photocatalysis. The holes could be consumed by supplying exogenous electron donors such as water, hydrogen, methane, and alcohols, while the synthesis process of artificial electron donors needs to be considered very carefully because it may cause more CO_2 emissions.[185] Among the exogenous electron donors, water appears to be more competitive because of its abundance and inexpensiveness. The oxidation potential of water, however, is higher than that used for CO_2 reduction, which implies that ideal photocatalysts should have the ability to oxidize water and reduce CO_2 simultaneously, but there is a dearth of this kind of photocatalyst.[186] In the presence of water, the photocatalytic reduction of CO_2 needs to have water splitting occur to continuously supply hydrogen for hydrogenation, which is very demanding in the manufacture of value-added chemicals. However, the use of water as an electron donor remains problematic because of its competition with CO_2 in terms of the reduction process. Scrutiny of the thermodynamic and kinetic window shows that the reduction potential of water to hydrogen is 0.0 V at pH 0, which is definitely much more positive than that most of CO_2 reduction reactions such as those that form

carbon dioxide, formic acid, and formaldehyde; the former reaction only needs two electrons, whereas the latter reactions undergo 4–8-electron processes. This consideration indicates that the generation of hydrogen is much more favorable than the generation of other products through CO_2 reduction. This fact is more likely considering that the reduction of CO_2 in water is limited by its low solubility, which indirectly increases the probability for electrons to react with protons for HER rather than for both electrons and protons to reach CO_2 for CRR. Therefore, reaction selectivity is important in the case of CRR, where modifying the photocatalyst surface, altering the exposed facets, introducing new active sites, applying directional charge driving forces, etc., are subject to that reaction selectivity.[180,182,187]

Here, we aim to explore PC-CRR in the production of value-added chemical compounds under light irradiation while emphasizing different phases of photocatalysts and how these phases can be achieved from laboratory protocols as well as the impact of these phases on the end products of CO_2 reduction processes. There is always an implicit understanding that phase tuning could change the local electronic configurations of the materials, which ultimately show improved physical and chemical properties that are essential for particular reactions of interest. Readers should be aware that there is a growing number of articles about PC-CRR with noble metal and effective photocatalyst systems,[184,188] which we do not summarize here because of the scope and limitation of this review article. At the end of this section, we tabulate (**Table 3**) some phase-based photocatalytic materials used for CO_2 reduction.

PC-CRR on Single Phases: Yu et al.[189] have investigated the exposed {001} and {101} facets in the anatase phase of TiO_2 samples in PC-CRR for methane production. By combining DFT calculations and experimental evidence, the authors confirmed that the photoactivity of CO_2 is highly dependent on the ratio of the exposed {001} to {101} facets. It has also been reported that the concentration of HF used in sample preparation has significant effects; for example, the formation of methane increases until the quantity of HF added exceeds 6 mL, which then reduces the photocatalytic activity of the sam-

ples. The accepted reasons were the large number of exposed {001} facets in anatase, which drive an electron overflow on {101} facets owing to their lower percentage. Therefore, the electrons on the {001} facets and within the interior are barely shifted to {101} facets, and because of the rich availability of {001} facets, the electrons can easily recombine with holes on {001} facets. Similarly, He et al.[190] have analyzed anatase TiO_2 catalysts with different morphologies, for example, nanoparticles, nanotubes, and nanosheets, for PC-CRR in the presence of water. The anatase nanosheets show superior photoactivity compared to that of nanotubes and nanoparticles. One plausible reason for this performance is that the anatase nanosheets have highly energetic exposed {001} facets, which could promote the oxidative dissolution of H_2O with holes, resulting in many electrons available for the reduction of CO_2 on {101} facets. An excess quantity of Ti^{3+} species caused by surface fluorination at the low-energy {101} reductive facets accelerated the reduction of CO_2 to CO_2^- and prolonged the lifetime of the photoinduced electron–hole pairs, thereby improving the photocatalytic activity.[190]

PC-CRR on Multiphases: TiO_2, one of the most well known and experimentally evaluated semiconductor materials in photodriven CO_2 reduction systems, naturally has three polymorphs/phases: a) anatase, b) brookite, and c) rutile. Of these phases, the investigation of brookite for CRR is less prevalent in the literature than studies of anatase, rutile or their mixtures. The electronic structure of these three polymorphs has a significant effect on the electron–hole separation processes. Theoretical analyses reveal that among the three polymorphs of TiO_2, anatase naturally has an indirect bandgap, while rutile and brookite possess a direct bandgap. Compared with the rutile and brookite phases, anatase has a smaller average effective mass of photoinduced electrons and holes, which makes it possible for anatase to transfer electrons and holes from the bulk side to the surface side very quickly, resulting in a reduced charge-carrier recombination rate and thus increasing the photoactivity for this phase.[191] It was shown that for anatase, the lifetime of electrons and holes was nearly an order of magnitude higher
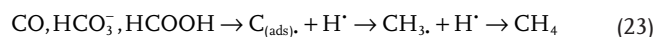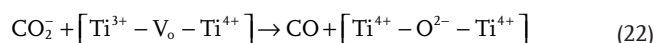
Table 3. Phase-based photocatalytic materials for CO_2 reduction.

Materials	Synthetic method	Cocatalyst	Light source	Reactions conditions	Yields and efficiency	Refs.
Anatase TiO_2 single crystals with {101} facets	Solvothermal	1 wt% RuO_2	300 W Xe lamp	CO_2 and H_2O vapor	CH_4 1.8 µmol g^{-1}	[200]
Ni-doped anatase TiO_2	Solvothermal		18 W Hg lamp	CO_2 saturated water	CH_4 14 µmol g^{-1} after 1 h irradiation	[201]
In doped anatase TiO_2	Solvothermal		400 W Hg lamp	CO_2, He, and H_2O vapor	CH_4 244, CO 81, C_2H_4 0.06, C_2H_6 2.78, C_3H_6 0.02, C_3H_8 0.02 µmol g^{-1} h^{-1}	[202]
Anatase TiO_2 nanosheets exposed with 95% of {100} facets	Hydrothermal		300 W Xe lamp	CO_2 and H_2O vapor	CH_4 5.8 ppm g^{-1} h^{-1}	[149]
Defective TiO_2 (anatase, rutile, and brookite)	Hydrothermal		150 W solar simulator	CO_2 and H_2O vapor	CH_4 12.8, CO 18.9 µmol g^{-1}	[52]
Anatase TiO_2			300 W Xe lamp	CO_2 and H_2O vapor	CH_4 1.35 µmol g^{-1} h^{-1}	[189]
Rutile TiO_2 modified anatase TiO_2 nanorods	Hydrothermal		300 W Hg lamp	CO_2 and H_2O vapor	CH_4 2.5 µmol g^{-1} h^{-1}	[203]
Monoclinic $BiVO_4$, tetragonal $BiVO_4$	Microwave-assisted hydrothermal		300 W Xe lamp	CO_2 and H_2O vapor	C_2H_5OH 600 µmol	[204]

**ADVANCED
SCIENCE NEWS**

www.advancedsciencenews.com

**ADVANCED
MATERIALS**

www.advmat.de

than that of rutile.[192] Having an indirect bandgap, the anatase phase promotes the highest photoactivity by preventing charge-carrier recombination, which strikingly increases the diffusion path length for electrons and holes. As a result, rapid translocation of the photon-excited electrons and holes from the bulk to surface was realized, where the photochemical reaction takes place. It is worth mentioning here that an excited charge carrier can penetrate deeper into surface sites from the bulk if the material promotes a higher electron mobility and longer lifetime. In this case, anatase is much more superior than the rutile phase because the surface penetration of the charge carrier in anatase is ≈5 nm, while that for is rutile nearly 2.5 nm, so it makes sense that anatase is much more promising than rutile polymorphs.[68]

Liu et al.[52] have studied photodriven CO_2 reduction in manufacturing value-added chemical compounds such as CO and CH_4 in the presence of water vapor reducing agents over defect-free and defective TiO_2 anatase, rutile, and brookite nanocrystals. Hydrolysis and hydrothermal synthetic methods were employed to selectively obtain the three TiO_2 phases, while in situ diffuse reflectance infrared Fourier transform spectroscopy (DRIFTS) was used to distinguish the CO_2 adsorption species and reaction intermediates on the anatase, rutile and brookite phase surfaces. The results indicate that the defective TiO_2 phases show remarkable photoactivity compared to that of the defect-free TiO_2 phases. Much of that role is likely due to the generation of oxygen vacancies and Ti^{3+} centers on the surface, which induce CO_2 activation both in the dark and under photoillumination by forming CO_2^- intermediates.[52] The surface-engineered brookite phase is reported to provide the highest yield of CO and CH_4 products, followed by the anatase and rutile phases. The formation of oxygen vacancies due to the defective brookite phase causes the rapid reaction of CO_2^- with adsorbed H^+ or surface OH^- groups and provides an alternative reaction pathway involving HCOOH intermediates.[52] Briefly, the reaction mechanism confirms the water dissociation (Reaction 17) and the formation of CO_2^- (Reaction 18), while reaction 19 shows that HCO_3^- intermediates have been observed on both helium (He)-treated anatase and brookite phases. CO forms from the reaction between CO_2^- and H^+ (Reaction 20), self-transformation (Reaction 21) or direct dissociation by healing the V_O sites (Reaction 22). However, CO_2^- intermediates were not observed on the He-treated brookite phase under photoillumination with water vapor reducing agents.[52] CH_4 can be produced via multielectron processes (Reactions 23 and 27) by the conversion of CO, surface HCO_3^- and HCOOH, as shown below.

Defective TiO_2 anatase and brookite:

$$H_2O + h^+ \rightarrow H^+ + OH^\cdot \tag{17}$$

$$CO_2 + Ti^{3+} \rightarrow Ti^{4+} - CO_2^- \tag{18}$$

$$OH^\cdot + CO_2^- \rightarrow HCO_3^- \tag{19}$$

$$CO_2^- + H^+ + e^- \rightarrow CO + OH^- \tag{20}$$

$$CO_2^- + CO_2^- \rightarrow CO + CO_3^{2-} \tag{21}$$

$$CO_2^- + \left[Ti^{3+} - V_o - Ti^{4+} \right] \rightarrow CO + \left[Ti^{4+} - O^{2-} - Ti^{4+} \right] \tag{22}$$

$$CO, HCO_3^-, HCOOH \rightarrow C_{(ads)\cdot} + H^\cdot \rightarrow CH_{3\cdot} + H^\cdot \rightarrow CH_4 \tag{23}$$

Defective TiO_2 brookite:

$$CO_2 + 2H^+ + 2e^- \rightarrow HCOOH \tag{24}$$

$$CO_2^- + 2H^+ + e^- \rightarrow HCOOH \tag{25}$$

$$HCOOH \rightarrow CO + H_2O \tag{26}$$

$$CO, HCOOH \rightarrow CH_4 \tag{27}$$

The presence of defects at the surface or bulk in a structural phase-based photocatalytic material has a positive effect on the overall photocatalytic performance due to its direct influence on the electronic structure. During photocatalysis, the defect sites work as recombination centers for photoinduced charge carriers and accelerate the overall reaction. It was reported that a single crystal of anatase before and after calcination treatment possessed much lower recombination rates for charge carriers than those for a rutile single crystal. Because rutile single crystals have a higher density of bulk defects, there is a higher probability of recombination of the photoinduced charge carriers and a reduction of their lifetime.[193] However, the presence of both defects simultaneously could further improve the surface reactions as well as photocatalytic activity for both anatase and rutile polymorphs. It was shown that when surface defects trapped the photoinduced electrons–holes upon light illumination, they could migrate to the reactive sites where they could combine with the electron acceptors/donors. In doing so, surface defects can play a role in prolonging charge-carrier separation, while the electron–hole pairs trapped by the bulk defect sites recombine because of the unavailability of reaction sites.[193] Compared with the CB and VB states, the defects increase the number of electronic states within the bandgap since the weaker bonding at defect sites can decrease the energy gap between the bonding and antibonding orbitals. During photocatalysis, the photoinduced charge carrier follows the mid-gap states to reach either the CB or VB, which controls the charge-carrier dynamics, known as surface states or trap states, if only when they are from surface defects.[194] It is improbable for charge carriers that lie in deeper trap states to contribute to the surface reactions, while those in shallower trap states can contribute to the surface reactions. Therefore, structural phase materials possess trap states of different depths, which can further change the lifetime of the charge carriers. Not only can surface defects cause variations in surface trap states for photoinduced charge carriers, but surface terminations also play a role in altering the trap states in structural phase materials. By varying the position of the hole-trapping states in the bandgap, it is thus possible to tune the photocatalytic materials for improved performance.

Kar and co-workers[195] have investigated the PC-CRR into methane (CH_4) over a pure rutile phase and mixed phases

ADVANCED
SCIENCE NEWS
www.advancedsciencenews.com

ADVANCED
MATERIALS
www.advmat.de

of anatase and rutile square-shaped TiO_2 nanotube arrays from electrochemical anodization in a water-based electrolyte, FANT-aq (flame-annealed TiO_2 nanotubes in aqueous electrolyte) and ethylene glycol-based electrolyte (FANT-eg) at 750 °C flame annealing. The FANT-aq sample produces 156 μmol $g_{catalyst}^{-1}$ h^{-1} of methane, while FANT-eg produces approximately 9.5 μmol $g_{catalyst}^{-1}$ h^{-1} of methane under solar light irradiation. The yields from the LANT-aq, (Low temperature annealed anatase-phase nanotubes in aqueous electrolyte) and LANT-eg (eg = ethylene glycole) samples were 92 μmol $g_{catalyst}^{-1}$ h^{-1} and 2 μmol $g_{catalyst}^{-1}$ h^{-1}, respectively. However, the flame annealing process partially converted the anatase phase into the rutile phase in the ethylene glycol-based TiO_2 nanotubes, which resulted in improved photoreduction of CO_2 into methane. A suitable band position is necessary to start the photocatalysis, and in this case, flame annealing in oxygen-deficient conditions may induce the formation of oxygen vacancies and Ti^{3+} states, which create subenergy levels below the conduction band (**Figure 19**). These subenergy levels reduce the energy needed for the excitation of electrons. The effective bandgap subsequently decreases due to the defects and subenergy levels.[195]

The phase conversion from anatase to rutile to brookite is said to be challenging because of the poor understanding of the applied processes and technologies, even though a growing number of synthetic protocols are available.[196] It is more believable that the coexistence of phases in TiO_2 photocatalysts could open opportunities to achieve higher photoactivity than that of the pure anatase or rutile phase because a synergistic phenomenon between them may need to be realized. Benavides et al.[196] have obtained various phases (anatase and/or rutile) of TiO_2 by varying the laser power density incident on a film of amorphous TiO_2 nanoparticles prepared by means of an incomplete nonhydrolytic sol–gel ester elimination reaction between titanium isopropoxide and oleic acid.

The motivation was the low-power-assisted photoactivation of TiO_2 films at room temperature. The microscopic studies reveal that only a critical particle size (14 nm) of amorphous TiO_2 nanoparticles can allow the laser-induced phase conversion into anatase. With a high propensity to absorb molecular oxygen, the TiO_2 nanoparticles undergo a successive phase transition from anatase to rutile. The authors insist that both phases may be patterned using the system dimensions of 25 × 25 mm^2 for a usable device. However, they claimed that in the absence of any kind of dopant in the TiO_2 film prior to photoactivation, the phase conversion is still achievable, and the great accomplishments of this work suggest that easy integration with TiO_2 can be suitable for many photo-electrocatalytic applications.[196]

Anatase and rutile heterojunctions for photocatalytic processes have shown remarkable efficiency because of the improved charge-carrier lifetimes, but such performance over anatase and rutile heterojunctions is now questionable and necessitates more fundamental exploration in this area. It is important to look at what actually happens within these heterojunctions, especially regarding the direction and efficiency of photoinduced holes and their impact on the photocatalytic function. Recently, Kafizas and co-workers[197] have studied hole transfer processes over anatase and rutile heterojunctions in films by using transient absorption spectroscopy (TAS) protocols as a function of phase composition. The phase conversion from anatase to rutile was observed above 600 °C, but this conversion process is slow in nature. The authors have insisted that the photoinduced holes can move to anatase from rutile on sub-microsecond time scales. Among the analyzed samples, an anatase and rutile composite shows an almost fivefold increase in anatase hole yield due to such hole transfer mechanisms from rutile. The charge recombination at the heterojunction surface is interesting, showing intermediate decay dynamics ($t_{1/2} \approx 4$ ms) between that of
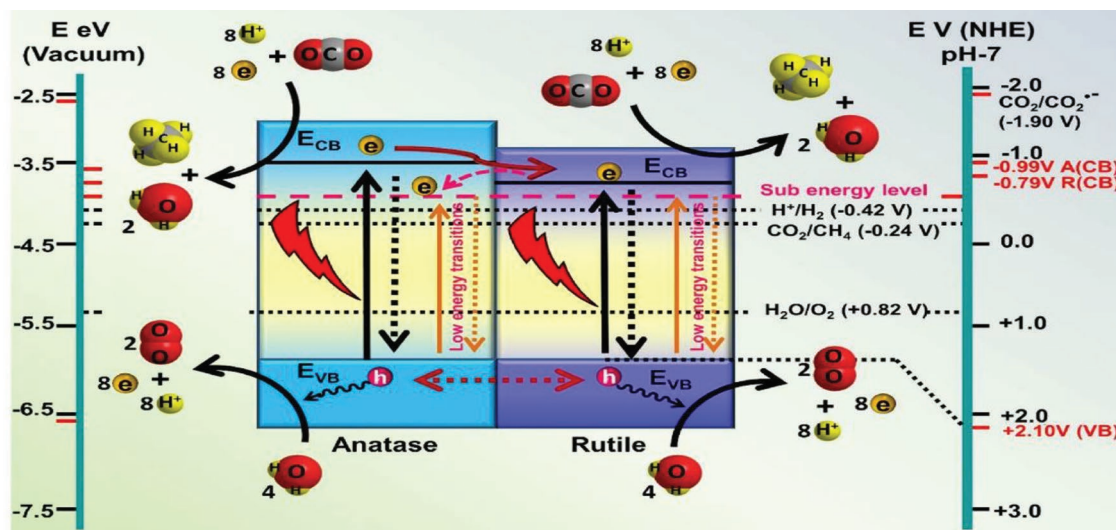

Figure 19. Possible reaction mechanism over FANT-eg. Due to the band position, electrons and holes move to their corresponding reactive sites inducing the photoredox reaction. It might be possible that anatase TiO_2 has low-energy shallow traps (0.8 eV below the conduction band of rutile) that cause electrons to move from rutile to anatase. Holes can move into the valence band of rutile or anatase or remain in the valence band of the same semiconductor depending on the type of energy band alignment. Adapted with permission.[195] Copyright 2019, Elsevier.

**ADVANCED
SCIENCE NEWS**

www.advancedsciencenews.com

**ADVANCED
MATERIALS**

www.advmat.de

pure anatase ($t_{1/2} \approx 0.5$ ms) and rutile ($t_{1/2} \approx 20$ ms), which negate the speculation that the synergistic enhancement in photocatalytic reactivity is solely caused by an enhancement in charge-carrier lifetime.[197]

Apart from TiO_2-based semiconductive materials, $NaNbO_3$ appears to show promising photocatalytic performance. With a typical perovskite structure, $NaNbO_3$ primarily displays two phases: a) cubic (c-$NaNbO_3$) and b) orthorhombic (o-$NaNbO_3$). Li et al.[143] have examined the photocatalytic performance of c-$NaNbO_3$ and o-$NaNbO_3$ phases and reported that the CO_2 reduction activities with the c-$NaNbO_3$ phase outperformed those of the o-$NaNbO_3$ phase under UV–vis light illumination.[198] Theoretical analyses reveal that the electron–hole pair generation and separation is highly accelerated due to the unique electronic structure of the c-$NaNbO_3$ phase. The authors stated that the high symmetry in the crystal structure could also improve the photoinduced excitation and transfer (**Figure 20**).

In another study, Li et al.[199] have tested c-$NaNbO_3$/o-$NaNbO_3$ phases for PC-CRR and found 30% and 200% enhancement in photoactivity with the mixed-phase junction compared with that of the standalone c-$NaNbO_3$ phase and o-$NaNbO_3$ phase, respectively. In brief, the photoactivity is higher in the c-$NaNbO_3$ phase than in the o-$NaNbO_3$ phase, while the mixed-phase junction synthesized between 450 and 525 °C exhibits much better activity than that in the c-$NaNbO_3$ phase and o-$NaNbO_3$ phase. The reason behind this result is that the phase junction could improve the photocatalytic performance of $NaNbO_3$. The phase junctions between the c-$NaNbO_3$ phase and o-$NaNbO_3$ phase can promote the photoinduced electrons from the conduction band of the o-$NaNbO_3$ phase to the trapping sites on the c-$NaNbO_3$ phase, lowering the charge recombination rate on the o-$NaNbO_3$ phase and thereby further prolonging the lifetime of the electron–hole pair in the mixed-phase $NaNbO_3$ junction. It is obvious that charge transfer in the c-$NaNbO_3$ phase is much easier than that in the o-$NaNbO_3$ phase, where the former phase is proven to show higher photocatalytic activity than that of its counterparts. We hypothesize that the electronic structure of c-$NaNbO_3$ changed the charge-carrier behaviors because the CB of c-$NaNbO_3$ is more dispersive than that of o-$NaNbO_3$,[143] indicating the smaller effective mass of the photoinduced electrons in c-$NaNbO_3$. As a result, the electrons easily separate from the holes and migrate to the reactive sites, thereby increasing the photoactivity. In summary, the mixed-phase junction appears to play a vital role in increasing the propensity of charge pair separation, and this is likely to improve the photocatalytic efficiency.[199]

4. SPE for Environmental Treatment

SPE is of great significance in catalyst design for environmental treatment by AOPs.[16] AOPs (i.e., PC-AOPs, EC-AOPs, PEC-AOPs, and FAOPs) have been regularly defined as water treatment processes conducted under mild conditions (room temperature and standard pressure) and based on the in situ formation of a series of ROSs at an adequate concentration to efficiently remove the contaminants.[21] To be specific, ROSs such as hydroxyl, sulfate, single oxygen, and superoxide radicals can be produced in the presence of homo- or heterogeneous
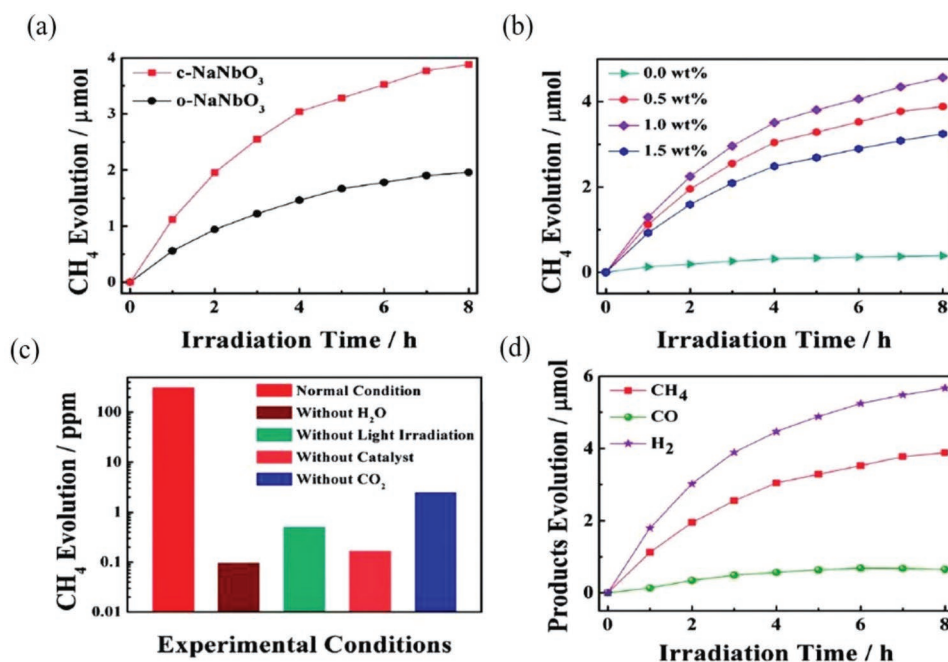

Figure 20. a) CH_4 formation in gas-phase reaction over c-$NaNbO_3$ and o-$NaNbO_3$ phases along with 0.5 wt% Pt loading. b) CH_4 formation over c-$NaNbO_3$ phase with 0.0, 0.5, 1.0, and 1.5 wt% Pt loadings. c) CH_4 formation in reference tests in absence of H_2O, CO_2, light irradiation, and catalyst compared with that in normal conditions. d) CH_4, CO, and H_2 formation in gas-phase reaction over 0.5 wt% Pt loaded c-$NaNbO_3$ phase. a–d) Adapted with permission.[143] Copyright 2012, American Chemical Society.
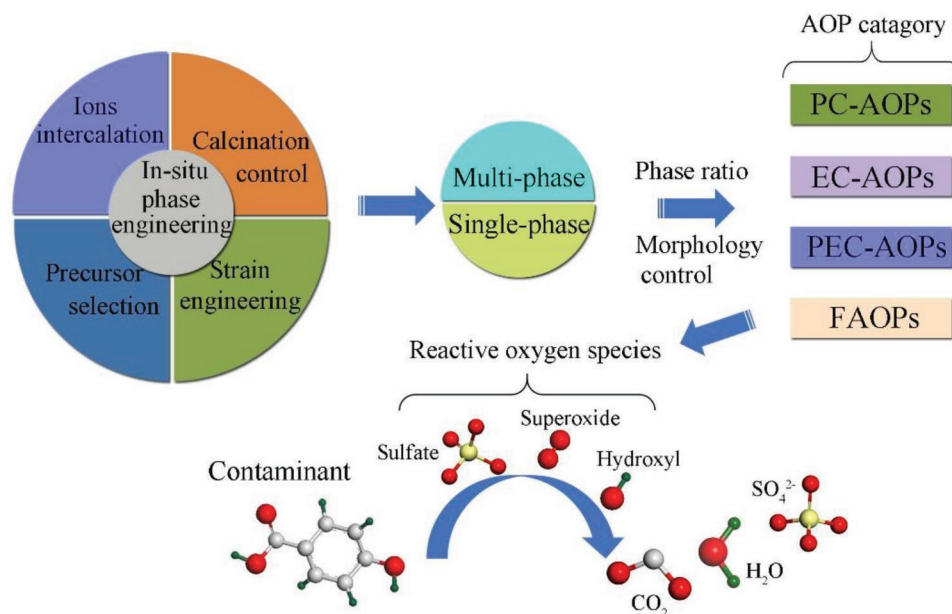
Figure 21. Roadmap of the in situ phase engineering for AOP applications.

catalysts, upon illumination, an applied voltage or with oxidizing agents (like H_2O_2, O_3, peroxymonosulfate or potassium persulfate), which can readily oxidize and decompose organic pollutants into nontoxic or less-toxic compounds (**Figure 21**).[205] However, the homogeneous catalyst-based AOPs suffer from some structural disadvantages. First, the generation of ROSs is strongly affected by pH value. Additionally, the rate of the redox cycle is hindered by the inherently slow reduction kinetics of metal ions (e.g., Fe^{3+} to Fe^{2+}).[16] In contrast, heterogeneous catalyst-based AOPs, which generally rely on nanoscaled metal oxide catalysts, have thus been studied to overcome these shortcomings.[206] Much efforts have been put on in situ phase engineering, which can convert precursors into efficient hetero-phase or single-phase catalysts via various approaches (Figure 21) such as metal-ion intercalation,[78] precursor selection,[207] strain engineering,[28] or thermal control.[208] For the same compound, it may exhibit various properties in different single-phase forms. It is worth noting that multiphase engineering route allows for the construction of suitable heterojunctions, which can maximize solar light utilization, enhance charge separation and transfer in semiconductors for more excellent photocatalytic activity. Through adjusting the multiphase ratios, phase morphology, or single-phase species, desired performance of catalysts can be achieved in environmental science. Multiphase engineering strategy plays an important role in catalyst preparation for PC-AOPs, while single-phase engineering strategies have been widely employed in PC-AOPs, EC-AOPs, PEC-AOPs, and FAOPs.[209] Based on the above analysis, the discussions are organized as follows.

4.1. EC-AOPs on Single Phase

The electrochemical advanced oxidation process has the superiority of being versatile and environmentally compatible. Other benefits include excellent energy efficiency, easy handling, and mild operation conditions. Conventionally, this technique is realized by the electrocatalytic oxidation at anodes, also known as anodic oxidation.[205] Once the process happens, robust oxidizing hydroxyl radicals (HO$^\bullet$) can be produced on the anode surface.[210] Typically, the probability of electrochemical oxidation is related with three parameters: i) the formation of chemically or physically adsorbed HO$^\bullet$ ($2H_2O \rightarrow 2HO^\bullet_{ads} + 2H^+ + 2e^-$); ii) competition of pollutant oxidation by HO$^\bullet$ with the OER process ($2HO^\bullet_{ads} \rightarrow O_2 + 2H^+ + 2e^-$); iii) the nature of the anodic material, including activity, stability and cost. Studies have principally focused on the latter two parameters, as it is crucial for EC-AOPs to be operated at suitable voltages to efficiently oxidize organic pollutants while avoiding the hole consumption by OER. Undoubtedly, single-phase engineering plays an important role in design of more stable and active electrode materials for organic pollutant degradation.

Metal oxides with inactive OER activity, such as tin dioxide (SnO_2) and lead dioxide (PbO_2), can generally act as the effective catalysts or substrates for electrochemical pollution oxidation, since OER side reaction is suppressed. Many techniques like anodic or cathodic deposition, have been directed to obtain different phases of metal oxides.[62] Abaci et al. investigated the performance of different phases of PbO_2 toward electrochemical phenol degradation.[63] By changing the precursor concentration and deposition current density, films of pure α-PbO_2 and β-PbO_2 were obtained, respectively. Consequently, the higher conductivity, superior stability, and unique porous structure endowed β-PbO_2 with higher HO$^\bullet$ flux and faster oxygen-atom transfer, resulting in better performance than α-PbO_2 in phenol degradation. The feasibility of different phases of nontoxic metal oxides (e.g.,. MnO_2, WO_3) are also explored for environmental electrocatalysis. With its abundant sources, MnO_2 has been broadly used as the electrode material for electrochemical application. Devaraj and Munichandraiah[64]

**ADVANCED
SCIENCE NEWS**
www.advancedsciencenews.com
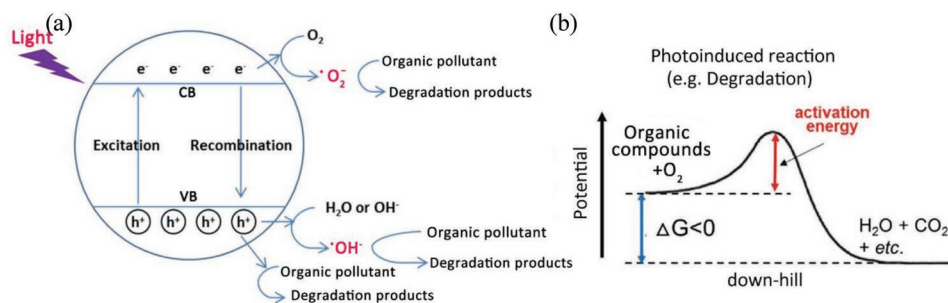
**ADVANCED
MATERIALS**
www.advmat.de

Figure 22. a) Proposed schematic photocatalytic degradation mechanism of organic pollutant over semiconductors. Reproduced with permission.[213] Copyright 2015, Elsevier. b) Distinct classifications of down-hill photocatalytic reactions. Reproduced with permission.[212] Copyright 2018, Wiley-VCH.

investigated the specific electrochemical capacitance of three MnO_2 phases, which followed an order of α-MnO_2 > γ-MnO_2 > β-MnO_2, suggesting their different electrocatalytic activities. Massa et al. reported the electrochemical oxidation of phenol over two electrodeposited MnO_x phases (α-MnO_2 and α-Mn_2O_3),[62] which exhibited distinctive activity and stability. To be specific, the cathodically electrodeposited α-MnO_2 was proved to be the more active phase and degraded phenol by 26.8%, while the anodically electrodeposited α-Mn_2O_3 showed better stability than α-MnO_2, with a final working potential of 2.9 V (vs RHE). Recently, they further reported two types of MnO_x-based anodes for the electrochemical oxidation of phenol.[210] Mixed cubic bixbyite α-Mn_2O_3/tetragonal α-MnO_2 (α-Mn_2O_3/α-MnO_2) and pure tetragonal α-MnO_2 were deposited on titanium foil by anodic or cathodic electrodeposition. It is noted that α-Mn_2O_3 is liable to induce the unwanted OER side reaction due to its low OER overpotential, while α-MnO_2 was considered as the more active MnO_x phase for the electrooxidation of organic compounds. Thus, the α-Mn_2O_3/α-MnO_2 showed a lower degradation efficiency of phenol (22.3%) than that ($\approx$43%) of pure tetragonal α-MnO_2 under ambient condition. However, at elevated pressure and temperature, the two electrodes displayed enhanced conversion efficiencies (up to $\approx$75%), due to the improved O_2 dissolution and reaction kinetics. In addition, it was suggested that the electrogenerated oxygen formed from OER by α-Mn_2O_3 could be exploited as a ROS for the degradation of recalcitrant organics under appropriate pressure and temperature.

WO_3 has five phase forms, i.e., hexagonal, monoclinic, triclinic, orthorhombic, and tetragonal phases. The monoclinic (m-WO_3) and hexagonal (h-WO_3) phases are most commonly studied for electrochemical water treatment. Generally, m-WO_3 is thermodynamically stable among its different polymorphs, while h-WO_3 will be transformed into m-WO_3 at elevated treatment temperatures. Through a cathodic deposition method, Habazaki et al.[211] obtained m-WO_3 film as the anode material for electrochemical decomposition of phenol. The as-deposited WO_3 film was in an orthorhombic phase, which transformed to amorphous WO_3 by annealing at 250 °C, and then to m-WO_3 phase at annealing temperatures over 350 °C. The thermodynamic stability of m-WO_3 rendered it with a low phenol decomposition rate and better adhesion to the substrate during electrolysis, exhibiting relatively high electrochemical activity in the chloride-containing solution.

4.2. PC-AOPs

Utilizing semiconductors and light illumination, a heterogeneous photocatalytic oxidation process is crucial in transforming organic pollutants into less toxic and biodegradable materials. As shown in **Figure 22**a, upon light irradiation, photocatalysis is initiated by the reception of photons that possessed higher energy than the bandgap energy (E_{bg}) of semiconductor materials. Charge separation then occurs in the semiconductor, triggered by electron transition from the valence band (VB) to the conduction band (CB), with holes retained in the VB. Consequently, organic degradation can be proceeded in two possible pathways. On one hand, the highly oxidizing photogenerated holes can oxidize the target contaminant directly. Alternatively, water molecules can be oxidized by the holes to form hydroxide radicals, which are accountable for indirect oxidation of organic pollutants. On the other hand, the dissolved oxygen in the solution can prevent the charge recombination and favor the generation of superoxide radicals for degradation of pollutants. However, if electrons cannot be transferred effectively, their accumulation in the CB will inevitably increase electron–hole recombination rate, resulting in low PC-degradation performance. Besides, from the thermodynamical point, the VB maximum is proposed to be more positive than the oxidation potential of the organic compounds to be oxidized.[212] Unlike the water splitting and CO_2 reduction, which are thermodynamic uphill reactions with a large positive change in Gibbs free energy (ΔG), the photodegradation of organic compounds in the existence of oxygen is usually a down-hill reaction, as shown in Figure 22b. Once a photocatalyst satisfies the thermodynamic demands, the degradation reaction may happen and the rate of the reaction can be evaluated by the kinetics, which usually involves the generation, diffusion, bulk and surface recombination of the electron–hole pairs, accompanied by the oxidation reaction with the organic compounds.

As aforementioned, the surface properties, thermostability, and conductivity of different phases have notable effects on the performance of the photocatalysts. Accordingly, it may be deliberative to promote or inhibit the phase transformation to select the more desired single phase or mixed phases for photocatalytic based AOPs. In the following sections, we review the SPE strategy over some promising single- or multiphase materials for PC-degradation, as summarized in **Table 4**.

Table 4. Structure-dependent activity of metal oxides in photochemical degradation and oxidation.

Photocatalysts	Category	Structural phases	Photochemistry application	Light condition	Reaction rate[a] (k) [min^{-1}]	Refs.
TiO$_2$ hollow nanospheres	Multiphase	Anatase/rutile	Methylene orange removal	8 mW cm^{-2}/UV–vis light	53% degradation/200 min	[214]
TiO$_2$ mesoporous hollow spheres	Multiphase	Brookite/anatase	Phenol and RhB degradation	300 W Xe lamp	0.077	[215]
TiO$_2$(B)/anatase nanowires	Multiphase	Anatase/brookite	RhB degradation	300 W Xe lamp	0.0402	[216]
Silica–titania	Multiphase	Anatase/rutile	Phenol oxidation	8 W UV light	198 mg g^{-1} h^{-1}[b]	[217]
TiO$_2$ microspheres	Multiphase	Rutile/anatase	Phenol and MB degradation	300 W Hg lamp	100% degradation/180 min	[218]
TiO$_2$(B)/anatase nanobelts	Multiphase	H$_2$Ti$_3$O$_7$/TiO$_2$(B)/anatase/rutile	Methyl orange photodegradation	300 W Hg lamp	0.0005	[219]
Brookite/rutile TiO$_2$ bicrystal	Multiphase	Brookite/rutile	Phenol oxidation	300 W Xe lamp	0.0274	[220]
Hexagonal/monoclinic WO$_3$ phase junction	Multiphase	Monoclinic/hexagonal	RhB degradation	300 W Xe lamp with 420 nm filter	0.01241	[221,210]
Zn$_3$(OH)$_2$V$_2$O$_7$·2H$_2$O precursor	Multiphase	Zn$_3$(VO$_4$)$_2$/Zn$_2$V$_2$O$_7$/ZnO triphase	Phenol/dyes degradation	500 W Xe lamp	80% degradation/150 min	[222]
Bi$_2$MoO$_6$/Bi$_2$Mo$_3$O$_{12}$ nanoplate	Multiphase	α-Bi$_2$Mo$_3$O$_{12}$/γ-Bi$_2$MoO$_6$	Aromatic alkanes oxidation	500 W Xe lamp with 400 nm filter	185.4 µmol g^{-1} h^{-1}[c]	[223,224]
BiVO$_4$ microspheres	Multiphase	M-BiVO$_4$/T-BiVO$_4$	Norfloxacine degradation	Visible light ($\lambda \geq$ 420 nm)	0.0159	[225]
Carbon nitride (CN)	Multiphase	Melon-based GCN/triazine-based crystalline carbon nitride (CCN)	RhB degradation	300 W Xe lamp with 400 nm filter	1.06 h^{-1}	[163]
TiO$_2$ nanobullets	Single phase	Brookite > anatase > rutile	RhB degradation	300 W Xe lamp	≈80%, degradation/60 min	[226]
FeOOH rod-like particles	Single phase	α-FeOOH > β-FeOOH	Acetaldehyde decomposition	500 W Xe lamp	–	[227]
MnO$_2$ nanocacti/nanorods	Single phase	α-MnO$_2$ > β-MnO$_2$	Degradation of congo red dye	500 W Hg lamp	0.1125	[228]
Flower-like MnO$_2$ nanocomposites	Single phase	δ-MnO$_2$ > α-MnO$_2$	MB degradation	8 W Hg lamp	0.05526	[229]
BiVO$_4$ nanodendritic/sheets/flowers	Single phase	ms-BiVO$_4$ > tz-BiVO$_4$ > ts-BiVO$_4$	MB degradation	400 W Xe lamp	≈70%, degradation/6 h	[230]

[a] Reaction rate constant for pollutant degradation, which was calculated based on the pseudo-first-order reaction kinetic model at the conversion below 70%; [b] Specific initial reaction rate, which represents reaction rate normalized by the amount of catalyst; [c] Formation rate of benzaldehyde during selective oxidation process.

4.2.1. PC-AOPs on Single Phase

TiO$_2$ has three crystalline phases, anatase, rutile, and brookite, which are widely used in photocatalysis. It is highlighted that the difficulty in brookite-based TiO$_2$ synthesis makes it the least investigated phase comparing with anatase and rutile. In a recent study, Choi et al.[226] had approached the unrevealed properties of brookite TiO$_2$ film as a photocatalyst for PC-AOPs application, through the photocatalytic degradation of several organic compounds, such as rhodamine B and tetramethylammonium chloride. Comparing with anatase and rutile TiO$_2$, the brookite phase exhibited much higher photoactivity, despite its smaller specific surface area compared with anatase. The study found the hydroxyl radicals as the main active species on brookite. The authors ascribed the higher performance of brookite phase to the below properties: i) a higher driving force

with more negative flat-band potential; ii) the efficient charge transfer kinetics with high conductivity; and iii) the production of more hydroxyl radicals, including mobile OH radicals.

It is noted that most forms of iron oxides and oxyhydroxides (FeOOH) have semiconductor properties and can act as promising photocatalysts for pollutant removal. Basically, there are two phases of Fe$_2$O$_3$ (α and γ), which differ in many aspects. α-Fe$_2$O$_3$ tends to be more stable, and its semiconductor properties make it possible to act as a photocatalyst, while the ferrimagnetic feature of γ-Fe$_2$O$_3$ makes it more suitable for high-density recording application. Cherepy et al.[231] conducted a kinetic study of photoexcited charge carriers in α-Fe$_2$O$_3$ and γ-Fe$_2$O$_3$ nanoparticles and found that the α-Fe$_2$O$_3$ and γ-Fe$_2$O$_3$ possessed equal transient absorption decay. Besides, the dynamics of the excited electrons in these two phases were also experimentally studied by the degradation
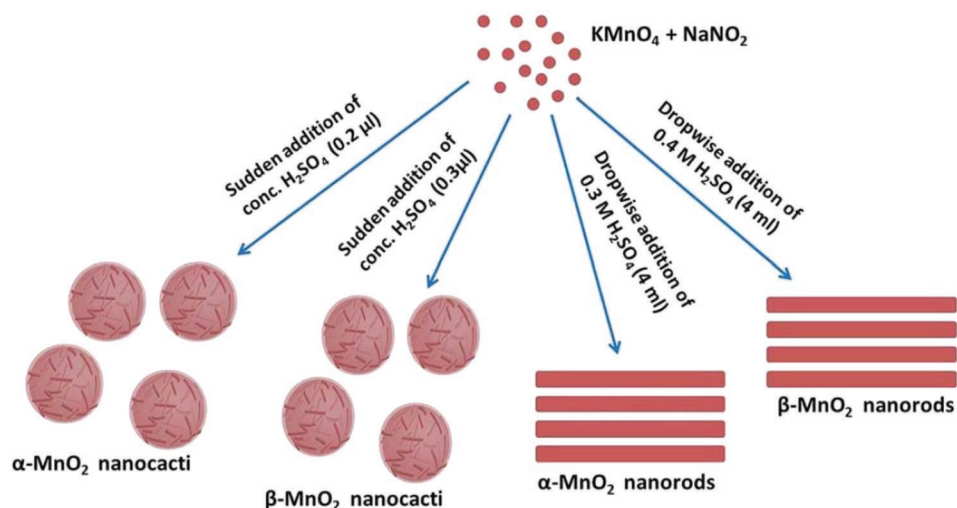
**ADVANCED
SCIENCE NEWS**

www.advancedsciencenews.com

**ADVANCED
MATERIALS**

www.advmat.de

Figure 23. Illustration of the formation of α- and β-MnO$_2$ nanocacti and nanorods at different reaction conditions. Reproduced with permission.[228] Copyright 2017, The Royal Society of Chemistry.

of Orange II. Interestingly, the ultrafast transient absorption of Orange II on these two phases showed no difference comparing with the commercial Fe$_2$O$_3$. Usually, FeOOH has two main phase structures, i.e., goethite (α-FeOOH) and akageneite (β-FeOOH), and both deliver outstanding photocatalytic properties. The bandgap energy of α-FeOOH (2.0 eV) is narrower than β-FeOOH (2.2 eV), indicating a higher visible-light absorption ability. Ohno's group[227] reported that the presence of chloride ions could lead to the preferred formation of β-FeOOH, whereas α-FeOOH was formed under the assistance of ethanol even in an acidic condition. Under visible-light irradiation, α-FeOOH with a larger specific surface area exhibited better photocatalysis than β-FeOOH toward acetaldehyde decomposition. In addition, the photodegradation activity of pyrene depended on the iron oxide phases, following a sequence as: α-FeOOH > α-Fe$_2$O$_3$ > γ-Fe$_2$O$_3$ > β-FeOOH.

The crystalline phases of MnO$_2$ include α-, β-, γ-, δ-, η-, and ε-MnO$_2$, which will exhibit different behavior in photocatalysis. The phase-dependent activity of MnO$_2$ has been recently investigated toward the photodegradation of dyes by Das et al.[229] Through a solution chemistry route, hierarchical flower-like MnO$_2$ were synthesized. The phase transition of MnO$_2$ from δ-phase to α-phase occurred at 450 °C, without morphology changes. The dye degradation indicated that δ-MnO$_2$ displayed a higher catalytic efficiency than α-MnO$_2$. This can be attributed to the diverse d bandgap energies (1.70 and 1.85 eV for δ- and α-phase, respectively). In addition, the different exposed facets of δ- and α-MnO$_2$ had a varying adsorption ability toward the reactants, which in turn affected the formation of ROS for dye degradation. Kumar et al.[228] reported phase engineering of α- and β-MnO$_2$ toward visible-light-driven photocatalysis. As shown in **Figure 23**, H$^+$ concentration was critical for phase transition of MnO$_2$ during the hydrothermal reaction. To be specific, decreasing H$^+$ concentration permitted the reduction of Mn^{4+} concentration for [MnO$_6$] unit growth, resulting in the formation of α-phase. In contrast, elevating H$^+$ concentration promoted the crystal face formation of β-MnO$_2$. Due to the enhanced active site exposure and larger specific surface area

brought by the massive tunnels in α-MnO$_2$, it exhibited superior photochemical degradation properties on Congo red and methyl orange.

Bismuth vanadate (BiVO$_4$), a promising visible-light-driven photocatalyst, can exist in three phase forms, i.e., monoclinic scheelite (ms), tetragonal scheelite (ts), and tetragonal zircon (tz). Guo et al.[230] prepared three phases of BiVO$_4$ by adjusting the hydrothermal time, acidity, and molar ratio of Bi to V and then investigated their photocatalytic activity toward dye degradation. As a result, the reactivity toward RhB degradation under UV or visible-light irradiation showed an order as ms-BiVO$_4$ > tz-BiVO$_4$ > ts-BiVO$_4$. Different crystal phases endow BiVO$_4$ with different band structures with ms-BiVO$_4$ possessing the narrowest bandgap and a unique hybridized VB, while ts-BiVO$_4$ has the largest bandgap. Specifically, the hybridized VB grants ms-BiVO$_4$ the higher oxidation ability and large dispersion, which favor the transfer of photogenerated holes and thereby enhancing the efficiency of organic pollutant oxidation.

4.2.2. PC-AOPs on Multiphases

For improvement of PC-AOPs activity, the charge recombination rate should be reduced as much as possible. Distinctly, heterophase engineering has been reported to solve this problem on various metal-based semiconductors, including Fe$_2$O$_3$, Mn$_2$O$_3$, TiO$_2$, and WO$_3$, etc.[232] As compared to traditional heterojunction between two different semiconductors, facile construction of heterophase junctions in exactly the same composition has more advantages in photogenerated charges transfer between the interfaces.[233] It can not only promote charge transfer and separation more efficiently, but also enhance light adsorption and phase stability, leading to more efficient photocatalysis than a single phase. Besides, considering the structure or lattice matching, the construction of heterophase junctions is more controllable and straightforward.
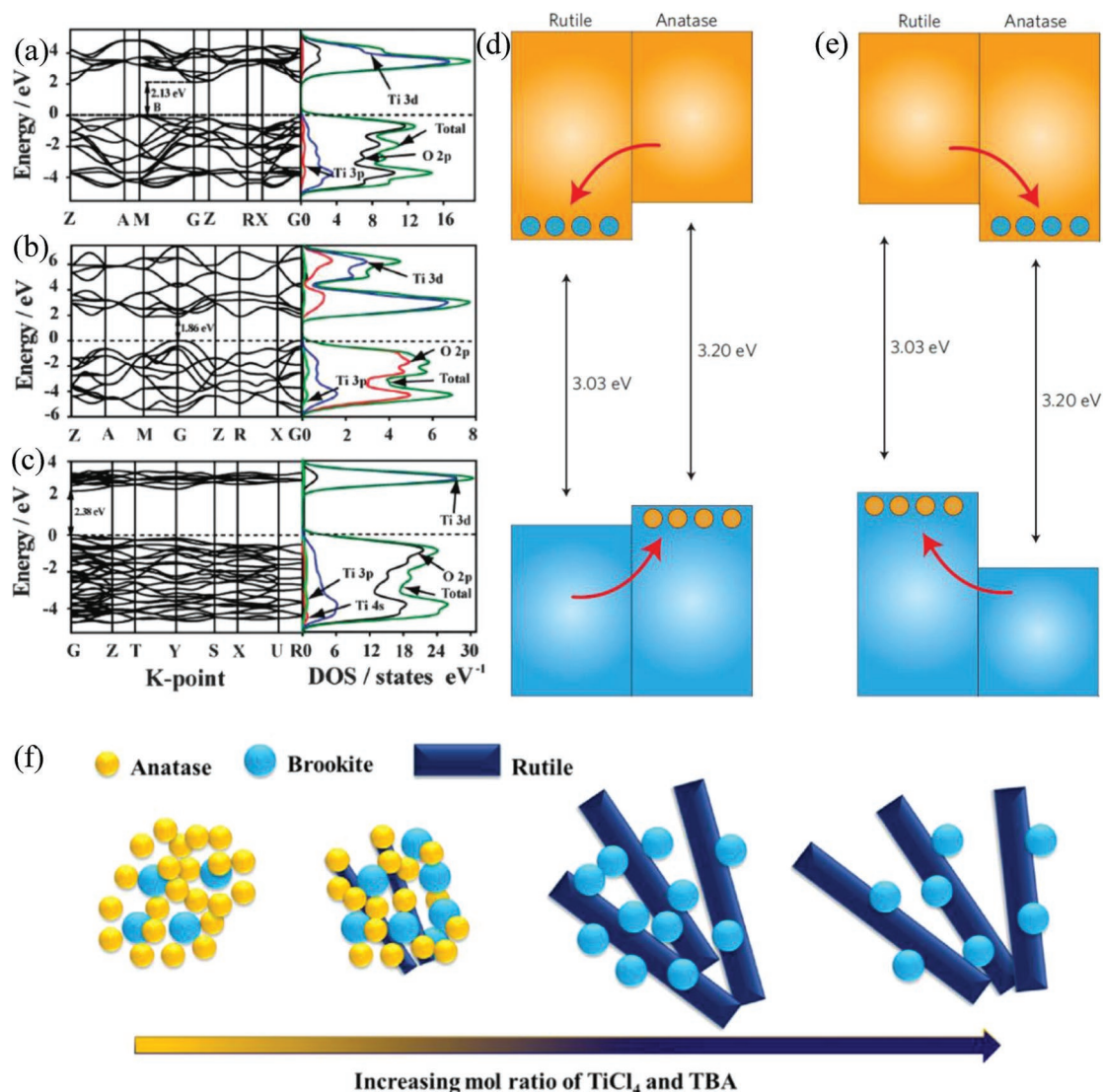
Figure 24. a–c) The band structure and DOS for: a) anatase, b) rutile, and c) brookite TiO$_2$. a–c) Reproduced with permission.[192] Copyright 2014, The Royal Society of Chemistry. d,e) Two proposed valence and conduction band alignment mechanisms for the anatase/rutile interface: d) Type-II (rutile), e) Type-II (anatase). d,e) Reproduced with permission.[237] Copyright 2013, Springer Nature. f) Formation of TiO$_2$ nanorods samples with different phases. Reproduced with permission.[220] Copyright 2016, Elsevier.

As stated before, titania (TiO$_2$) can exist in anatase, rutile, and brookite forms. Rutile TiO$_2$ is stable, while anatase and brookite phases are metastable and brookite is scarcely investigated due to the synthesis difficulty. Rutile TiO$_2$ has its merits of better chemical stability, greater light scattering efficiency, and lower production cost. Anatase TiO$_2$ appears to be an indirect-bandgap semiconductor, while rutile and brookite TiO$_2$ belong to the direct ones. Because of this, the lifetime of photoexcited electrons and holes produced in anatase TiO$_2$ tends to be longer than in rutile or brookite TiO$_2$ (**Figure 24**a–c).[192,234,235] Besides, as anatase TiO$_2$ has a higher localized density of states, it will produce more surface-adsorbed ROS than rutile phase. Hence, it is widely believed that the PC activity of anatase TiO$_2$ is superior to that of the rutile phase.[236] Rutile TiO$_2$ possesses smaller bandgap energy (only 3.03 eV) than anatase TiO$_2$ (3.20 eV) and Scanlon et al.

have found that the CB and VB edges of rutile TiO$_2$ were 0.22 and 0.44 eV higher than anatase.[237] When combining the two phases in a rutile/anatase biphase configuration, such a band alignment would favor photogenerated electron transfer from rutile to anatase phase while holes migrate conversely from anatase to rutile TiO$_2$. Consequently, charge recombination is suppressed, as explained in Figure 24d,e.

A typical example of employing anatase/rutile heterophase junction is Degussa P25, which is a mixture of anatase (70 wt%) and rutile (30 wt%) and has been utilized as a reference sample in photocatalysis.[238,239] Since the synergy between the two phases in P25 was firstly suggested in 1991,[240] there has been intense discussion on the mechanism and optimal phase composition. Hurum and co-workers have proposed that rutile TiO$_2$ played a more critical role in the heterophase.[238] Kordouli et al. reported the effect of anatase/rutile (A/R) ratios

**ADVANCED
SCIENCE NEWS**

www.advancedsciencenews.com

**ADVANCED
MATERIALS**

www.advmat.de

on photocatalytic degradation efficiency of P25.[241] It was found that numerous heterojunctions were constructed at A/R ratios of 0.5 and 0.8, which showed efficient degradation on Orange G and Yellow 28. Likewise, Besenbacher's group observed a notable synergetic effect between anatase and rutile TiO_2 that permitted for higher activity than a pure single phase.[242] It was reported that a well-defined anatase ratio (40–80 wt%) endowed the sample with the most distinct synergistic effect in photocatalytic degradation of methylene blue.

In addition to A/R ratio, the different morphologies formed in TiO_2 heterophase are closely related with the final photocatalytic activity. When constructed as hollow microspheres, heterophase TiO_2 exhibited further enhanced photocatalysis than the bulk one. Through the Ostwald ripening process, Zhao et al. synthesized mesoporous hollow spheres of biphase TiO_2 (23 wt% brookite and 77 wt% anatase) for excellent PC degradation of phenol and rhodamine B (RhB).[215] Macak et al. synthesized integrated TiO_2 nanotubes (NBs) layers through self-organized electrodeposition.[236] To accurately study the effect of phase composition and morphology, the initial deposited TiO_2 NBs were annealed at different temperatures. The proportion of rutile increased with elevated annealing temperatures, leading to reduced photoactivity. The TiO_2 NBs annealed at 450 °C maintained the well-defined anatase phase and exhibited the best activity. This result was basically consistent with most reports in literature that claim the better performance of anatase among different TiO_2 forms. Attributed to the optimized geometry and shorter carrier-diffusion paths, TiO_2 NBs with the same A/R ratio to commercial P25 exhibited a higher degradation efficiency of methylene blue (MB) than P25. However, this report also put forward a counter-argument toward the function of anatase/rutile heterophase, i.e., the mixtures of anatase and rutile would weaken the photocatalytic efficiency comparing with pure anatase phase. In addition, the ratio and the configuration position of anatase/rutile will act different positive or negative roles.

Excepted for the anatase/rutile heterophase junction, brookite/rutile junction has also been launched as efficient photocatalysts. As mentioned before, the brookite phase of TiO_2 has gained much less attraction due to its thermodynamic metastability.[243] However, it is reported that the activity of brookite TiO_2 can exceed anatase TiO_2 under certain condition.[244] By regulating the ratio of $TiCl_4$ and t-BuOH during the solvothermal process, Cao et al. synthesized crystalline TiO_2 with different phase constitutions and morphologies, as shown in Figure 24f.[220] Distinctly, the brookite/rutile TiO_2 nanocrystals with a high brookite content (72 wt%) were prepared for the first time. Comparing with the commercial P25, this biphase TiO_2 displayed more superior photocatalytic degradation performance toward phenol oxidation. It was also suggested that the synergetic effect between rutile and brookite TiO_2 increased with a higher brookite proportion, which might be more effective in promoting charge separation than that of anatase/brookite junction. Through a surface-preferred phase transformation, Ma's group synthesized TiO_2 nanowires with brookite/anatase junctions.[216] Specifically, during the high-temperature calcination, brookite nanowires partially converted into the anatase phase and form heterojunction naturally. With an optimized structure containing

24 wt% brookite in the bulk and 100 wt% anatase on the surface, the sample exhibited the best photocatalytic degradation performance of RhB, with a reaction rate constant of 0.0402 min^{-1}.

As an alternative semiconductor catalyst to conventional TiO_2, WO_3 has drawn intriguing attraction due to its outstanding visible-light absorption ability. However, SPE investigations on WO_3 are limited due to the barely controllable phase transition process. Generally, h-WO_3 is not strictly stoichiometric and the structure of h-WO_3 could not be maintained without stabilizing ions in the hexagonal channels.[246] Benefiting from the open-tunnel structure and rich intercalation chemistry, h-WO_3 normally has a high specific surface area.[247] In contrast, m-WO_3 is more attractive for photocatalytic applications due to its thermodynamic stability and suitable bandgap energy for the visible-light adsorption. Taking advantage of the metastability of h-WO_3, Li's group tuned the phase transition of WO_3 utilizing K_2SO_4 as a stabilizing agent.[221] Consequently, an effective h/m-WO_3 photocatalyst was synthesized, and the constructed phase junction enabled efficient electron–hole pair separation for more efficient RhB degradation than pure m-WO_3.

In addition to energy application, phase regulating of MoS_2 can also be employed in environmental engineering for photocatalytic treatment of organic pollutants. It was found that the high mobility for charge transport and density of active sites support 1T MoS_2 with the superior role to act as the cocatalyst than 2T phase for enhancing the photocatalytic dye degradation performance of TiO_2.[146] Recently, Saber et al.[248] investigated the effect of the mixed phases of MoS_2 on photocatalytic pollutant degradation. Through a hydrothermal method by adjusting Mo:S ratio, MoS_2 nanosheets with different phases (1T/2H, 1T/3R, and 2H) were obtained, as shown in **Figure 25**a. The photocatalytic results showed a much higher performance of the 1T/2H phase compared to the 2H and 1T/3R phases. The computational calculations demonstrated that the introduction of 1T sites into the 2H structure could create the surface distortions, mid-gap states and sulfur vacancies at the edges of the 1T defect sites, which serve as active sites for photocatalysis. Further, it was claimed that 1T defect is more suitable for cooperating with 2H rather than 3R, as the 1T regions in the 3R phase are more homogeneously distributed than in the 2H phase, causing 1T/3R more challenging to be exfoliated.

Bismuth molybdates have a basic component formula of $Bi_2O_3 \cdot xMoO_3$ where x = 3, 2, or 1, are corresponding to α, β, γ, and γ' phases, respectively. With suitable band location and excellent spectral properties, phase engineering on bismuth molybdates (α-$Bi_2Mo_3O_{12}$, β-$Bi_2Mo_2O_9$, γ-Bi_2MoO_6, and cubic $Bi_{3.64}Mo_{0.36}O_{6.55}$) have received interesting research attention. Song et al.[223] proposed the fabrication of $Bi_2MoO_6/Bi_2Mo_3O_{12}$ biphase by a one-step Bi self-doping route. During the synthetic process, the introduced Bi^{3+} would combine with a portion of MoO_4^{2-} and influence its transition to MoO_6 octahedron, in situ forming a $Bi_2MoO_6/Bi_2Mo_3O_{12}$ composite, as shown in Figure 25b. The heterostructure granted the biphase with significantly better photocatalytic activity toward the oxidation of toluene to benzaldehyde than that of the individual bismuth molybdate phase.
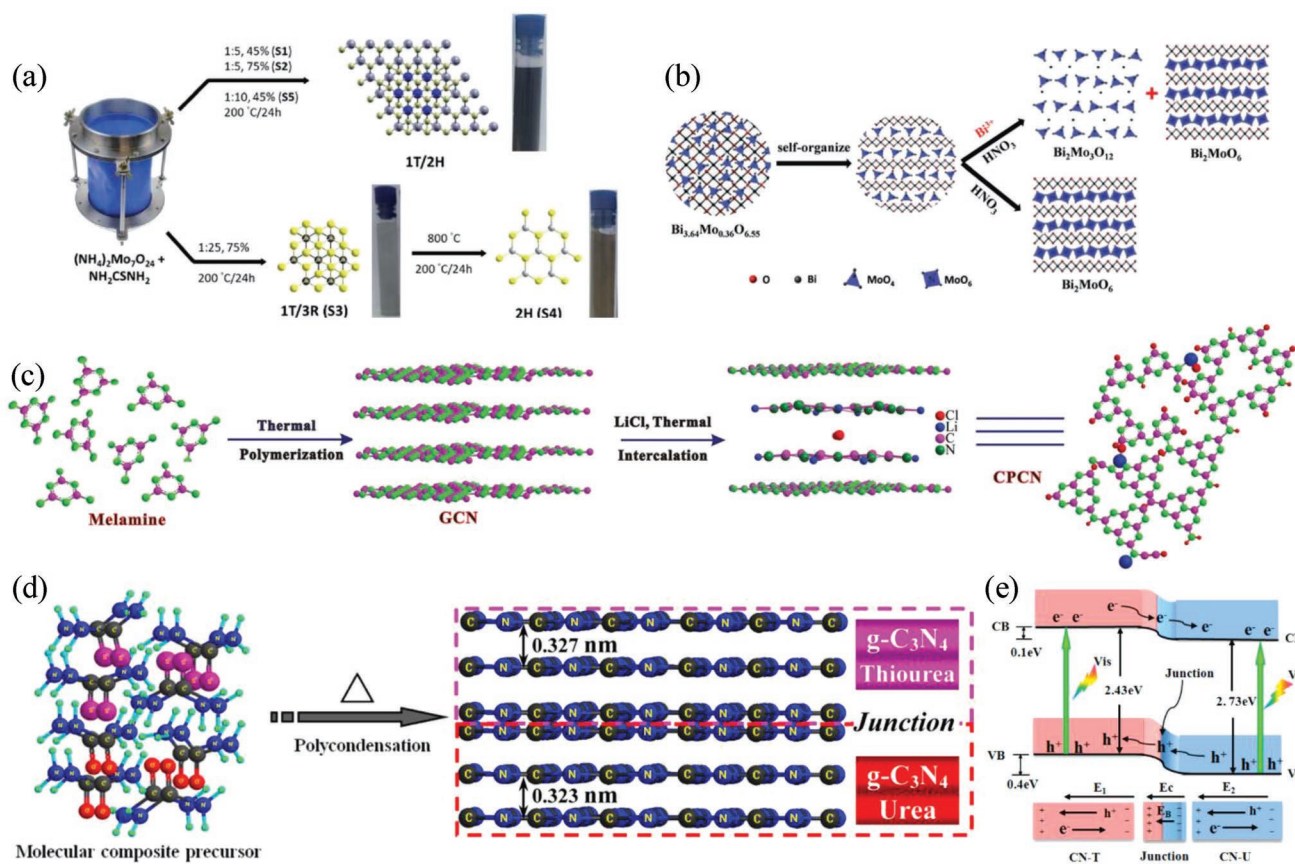
ADVANCED
SCIENCE NEWS
www.advancedsciencenews.com

ADVANCED
MATERIALS
www.advmat.de

Figure 25. a) Illustration of the preparation of MoS_2 nanosheet with different hybridized phases. Reproduced with permission.[248] Copyright 2018, The Royal Society of Chemistry. b) The formation of Bi_2MoO_6–$Bi_2Mo_3O_{12}$ heterojunctions. Reproduced with permission.[223] Copyright 2017, The Royal Society of Chemistry. c) The preparation approach of CPCN. Reproduced with permission.[163] Copyright, 2016 Wiley-VCH. d) Schematic illustration of the formation process of the CN-T/CN-U heterojunction. e) Schematic illustration of electron–hole separation and transport at the g-C_3N_4/g-C_3N_4 heterojunction interface. d,e) Reproduced with permission.[207] Copyright 2013, American Chemical Society.

Yu et al. reported a general method for the synthesis of Ag_2O/Ag_2CO_3 heterostructures by tailoring calcination time and temperature.[249] The as-obtained photocatalyst displayed extremely high activity and stability, superior to previously reported Ag_3PO_4 catalyst. Through a microwave-assisted hydrothermal method and subsequent calcination process, Zeng et al.[222] reported the preparation of $Zn_3(VO_4)_2$/$Zn_2V_2O_7$/ZnO triphase. The phase transition process of $Zn_3(OH)_2V_2O_7 \cdot 2H_2O$ can be defined as follows: i) the dehydration of $Zn_3(OH)_2V_2O_7 \cdot 2H_2O$ to form $Zn_3(VO_4)_2$ and ii) partial $Zn_3(VO_4)_2$ undergo a phase transition to produce $Zn_2V_2O_7$ and ZnO ($Zn_3(OH)_2V_2O_7 \cdot 2H_2O \rightarrow Zn_3(VO_4)_2 \rightarrow Zn_2V_2O_7 + ZnO$). The double Z-scheme heterojunction constructed in the triphase hybrid could effectively prolong the lifetime of photogenerated charges, accelerate the interfacial charge-transfer and allow for wider light-response. As a result, the composite exhibited conspicuously higher visible-light photoactivity than pure $Zn_3(VO_4)_2$ in the degradation of phenol and dyes.

Metal-free polymeride, typically carbon nitride (g-C_3N_4, CN), has been reported to be another kind of candidate for phase engineering and utilized for PC-AOPs. Several groups[207,250,251] have prepared isotype heterojunctions through interface coupling of differently structured graphite carbon nitride (GCN).

For example, an isotype heterojunction of polymeric carbon nitride (CPCN), that contains two different GCNs, melon-based GCN and triazine-based crystalline CCN, was reported to be naturally formed at the interface between GCN and CCN by a thermal reaction method (Figure 25c).[252] Due to the great compatibility between GCN and CCN and good match of their different band structures, the formed heterojunction can act as a driving force for separating the photogenerated charge carriers, which endows the CPCN with significantly improved photocatalytic performance for the photocatalytic degradation of RhB over monocomponent GCN and CCN under visible-light irradiation. Dong et al. reported a novel layered g-C_3N_4-T/g-C_3N_4-U metal-free heterophase junction by the polymerization of two different precursors (thiourea and urea) simultaneously (Figure 25d).[207] The junction exhibited significantly enhanced photocatalytic activity for the removal of NO from the air under visible-light irradiation. As indicated in Figure 25e, the improved performance could be directly ascribed to the efficient charge separation and transfer across the heterojunction interface and to the prolonged lifetime of the charge carriers. These well-designed isotype heterojunctions by coupling of organic polymers present an effective avenue for developing efficient metal-free photocatalysts.

4.3. PEC-AOPs on Multiphases

The preponderance of the PC-AOPs system is its compatibility for large-scale applications. Nevertheless, the reusability and the complex separation of photocatalysts from the reaction solution present a great challenge for the commercialization of this technique. In a PEC system, immobilization of photocatalysts onto conducting substrates eliminates the requirement for separation of a photocatalyst from the solution suspension. In addition, PEC technique combines the synergy between electrocatalysis and photocatalysis to afford a much higher efficiency for pollutant remediation. To be specific, the PEC-AOPs system consists of the employment of light irradiation and a continuous current or bias anodic potential to a semiconductor-based anode for the constant extraction of photogenerated electrons through an external circuit. The electrochemical techniques make it possible to separate the oxidation half-reaction from the reduction reaction, permitting the investigation of the photocatalytic oxidation alone without the need to consider the removal of photoelectrons by electron acceptors. Apart from its significance in photocatalysis, TiO_2 has been testified to be an expressly attractive PEC candidate for the decomposition of organic compounds in water.[209] Similar to the leading advantage of anatase phase in PC-degradation, the most suitable single phase for PEC degradation is anatase TiO_2.[209] However, studies have revealed that the rutile phase of TiO_2 immobilized onto a conductive substrate can also exhibit meaningful PEC oxidative capability, although inferior to that of the anatase phase.[253] Leng et al.[254] reported that a rutile TiO_2 film, obtained by electro-oxidization of Ti foil and thermal oxidization at 700 °C, exhibited a higher photoelectric conversion efficiency than anatase TiO_2 film prepared by the sol–gel method and calcination at 500 °C. Additionally, the rutile phase had a better adhesion property onto the Ti substrate than the anatase phase, making the TiO_2 anode more stable.[254] Zhao's group first adopted a PEC approach to investigate the photocatalytic performance of nanoporous anatase TiO_2 film electrode.[255] Further, they employed the same approach to prepare nanoporous anatase/rutile TiO_2 film electrode for photocatalytic degradation of organic compounds.[256] Compared to pure anatase TiO_2, the coupling of anatase/rutile phases enabled the vectorial displacement of electrons from anatase to rutile TiO_2 that can inhibit the recombination of photogenerated electron/hole pairs. Owing to the longer lifetime of holes, the anatase/rutile TiO_2 photoanode could oxidize a broad range of organic compounds more effectively and nonselectively.

In a typical work, Garcia-Segura et al. synthesized a TiO_2 anode film made of 29% rutile, 9% anatase, and 62% of Ti_7O_{13} by an atmospheric plasma spray method.[257] This photoanode was linked with an air-diffusion cathode that generates H_2O_2 in a photoelectrochemical cell to examine its oxidation ability toward the degradation of Acid Orange 7. The authors crosswise compared the catalytic performance of the TiO_2 films under different AOPs conditions, i.e., EC-AOPs, PC-AOPs, and PEC-AOPs. The worst degradation performance (21% color removal in 300 min) took place in PC-AOPs, due to the quick recombination of the photogenerated electron–hole pairs, which would further restrict the reaction of holes with water to form ·OH for the pollutant degradation. EC-AOPs in the dark degraded relatively quickly the dye solution (46% color removal in 300 min), which can be ascribed to the oxidation behavior of ·OH generated at the TiO_2 surface as intermediate of the anodic oxidation of water to O_2 by the reaction: $H_2O \rightarrow$ ·OH + H^+ + e^-. The limiting performance found in EC-AOPs can then be attributed to the poor production of reactive ·OH on TiO_2 anode from the anodic oxidation. In contrast, the PEC-AOPs was proved to be the most robust technique for the dye degradation (total color removal in 120 min), which verifies the point that the employment of the current provides the efficient separation of the photogenerated electron–hole pair on the TiO_2 photoanode, fast electrons transfer to the cathode and improvement of the reaction between holes and water to produce large quantities of oxidant ·OH. The dye degradation also followed a pseudo-first-order, which was quickened with increasing anodic current due to the higher ·OH generation from the production of more photogenerated holes and the faster anodic oxidation of water.

Except from adopting the traditional annealing approach for the phase regulation, elements doping is also applicable to accelerate or prohibit phase transition to receive desired phase structure or constitution. Egerton et al. reported that C-doped TiO_2 nanotube photoanodes presented a noticeable improvement in PEC degradation of sodium oxalate.[258] It was proved that C doping repressed the transformation of anatase to rutile TiO_2, allowing the growth of anatase phase to a larger size that was in favor of the PC activity. Tu et al.[259] described that the incorporation of Sn into TiO_2 lattices could accelerate phase transition from the anatase to rutile at low annealing temperature, leading to a smaller energy bandgap. The coexistence of anatase with tiny amount of rutile TiO_2 generated the favorable interface, which could trap electrons to enhance charge separation. As a consequence, the PEC degradation on MB was effectively improved.

4.4. FAOPs on Multiphases

Due to the superior efficiency in removing organic pollutants in wastewater, Fenton-like AOPs have received growing attention recently.[206,260] Typically, Fenton reaction requires the activation of H_2O_2 to produce ·HO by the catalysis with a Fe^{2+}/Fe^{3+} redox pair. In contrast, researchers have proposed two distinct reaction pathways (i.e., radical and/or nonradical) for Fenton-like AOPs.[261] As shown in **Figure 26**, the radical pathway, is based on introducing effective catalysts to activate an oxidizing agent such as peroxymonosulfate (PMS) to produce various ROS including ·OH, $SO_4^{·-}$, and $^1O_2$, which can strongly oxidize or turn most organic pollutants into low toxic compounds.[262] For the nonradical pathway, heterogeneous catalysts can serve as a mediator to facilitate the electron transfer from pollutants to the oxidant directly.[16] Consequently, the heterogeneous catalysts play the crucial roles in both the reaction pathways. Interestingly, structural-based single or multiple phase nanoengineering was also adopted in adjusting the catalytic properties of catalysts based on metal oxides.

Zhang et al.[263] synthesized β-MnO_2 nanorods for MB oxidation with the assistance of H_2O_2, while Dong et al.[264]

ADVANCED
SCIENCE NEWS
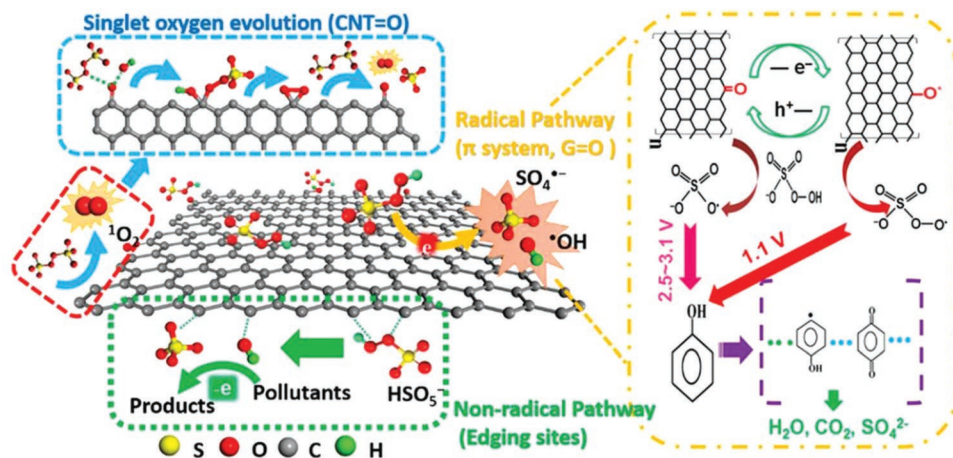www.advancedsciencenews.com

ADVANCED
MATERIALS
www.advmat.de

Figure 26. Illustration of activation of PMS on carbocatalysts. Reproduced with permission.[261] Copyright 2018, American Chemical Society.

evaluated the catalytic properties of β-MnO$_2$ nanowires for the phenol degradation. From the thermodynamical point, the initial concentrations of the oxidizing agent, pH, and reaction temperature have a direct influence on the catalytic performance. Wang's group first compared the catalytic performance and activation energy of α-, β-, and γ-MnO$_2$ in PMS activation for phenol solution degradation. Attributed to high surface area, oxygen loss, and double tunneled structure of α-MnO$_2$, the activity of the three phases followed an order of α-MnO$_2$ > γ-MnO$_2$ > β-MnO$_2$.[265] The authors found that α-MnO$_2$ can completely degrade phenol in 15 min at 45 °C. Based on the first-order kinetics and Arrhenius relationship, the activation energy was thus calculated to be at a very low value (21.9 kJ mol^{-1}) for α-MnO$_2$. They also compared the catalytic activity of manganese oxides with different oxidation states in phenol degradation by AOPs. Possibly arising from the different redox potentials, the activity of these oxides abided the sequence as Mn$_2$O$_3$ > MnO > Mn$_3$O$_4$ > MnO$_2$.[266] It was also reported that, due to the distinction in different surface atom arrangements on the active surface facets, corolla-like δ-MnO$_2$ displayed better performance than urchin-shaped α-MnO$_2$ in AOPs[267] α- and β-MnO$_2$ nanorods were also synthesized for excellent catalytic decolorization of dyes with H$_2$O$_2$.[268]

Generally, layer-structured δ-MnO$_2$ can be readily transformed into the tunnel-structured α-, β-, and γ-MnO$_2$, due to its thermodynamical metastability. Sinha et al.[269] found that MnO$_2$ underwent a shape transformation from 2D nanosheets to 1D nanowires, along with the phase transition from δ-phase to α-MnO$_2$ via a dissolution–recrystallization path. The α-MnO$_2$ nanowires can act as a reusable catalyst for the hydrolysis of benzonitrile to benzamide. The proportion of the surface Mn (III) and the surface adsorbed oxygen plays the key roles in determining the catalytic activity of different phased MnO$_2$. Through an anion-assisted hydrothermal method, Kuang et al.[270] reported 1D α- and β-MnO$_2$ nanorods via altering the anions. Photocatalytic results proved that β-MnO$_2$ nanostructures exhibited better catalytic activity and stability to remove organic pollutants with the assistance of H$_2$O$_2$. To be specific, comparing with α-MnO$_2$, β-MnO$_2$

holds the higher percentage composition of surface Mn (III), which provides the maximum electron transfer from Mn (III) to H$_2$O$_2$ to produce the ROS and react with MB. Also, the higher proportion of surface adsorbed oxygen in β-MnO$_2$ would promote the reversion of Mn (IV) to Mn (III) for further electron transfer.

In another study, Khan et al. reported α-Mn$_2$O$_3$/α-MnO$_2$ nanorod biphase, which showed more efficient and stable activity in PS activation than other single-phase manganese oxides including α-, β-, γ-, δ-MnO$_2$, α-Mn$_2$O$_3$, Mn$_3$O$_4$, etc. This is because the unique structure endowed the composite with more effective redox property that promoted electron transfer between different Mn species (Mn$_{IV}$ ↔ Mn$_{III}$) for more efficient generation of ·OH, SO$_4$·$^-$, and ^{1}O$_2$ during the degradation of organic contaminants.[63] Zhang et al.[271] designed two biphased MnO$_2$@MnO$_2$ core–shell nanostructures and applied them for dimethyl ether combustion. Using α-MnO$_2$ nanowires as a matrix, α-MnO$_2$ and γ-MnO$_2$ short nanorods were chemically deposited on the surface of the substrate, forming lavender-like and balsam pear-like morphologies under the acidic or alkaline deposition conditions. The hierarchical porous structures enable the MnO$_2$@MnO$_2$ with the synergic effect between the core and shell, therefore the MnO$_2$@MnO$_2$ display superior activity than pure α-MnO$_2$. Further, comparing with α-MnO$_2$ shell, the formed γ-MnO$_2$ shell enables the nanostructures with higher reducibility, resulting in higher surface oxygen species mobility and a better catalytic activity of α-MnO$_2$@γ-MnO$_2$ than α-MnO$_2$@α-MnO$_2$.

5. Challenge and Opportunities

Redox reactions, such as EC-HER, EC-ORR, EC-OER, EC-OWS, PC-HER, PC-OWS, PEC-OWS, PC-CRR, PC-AOPs, EC-AOPs, PEC-AOPs, and FAOPs, have significant scientific merits in clean energy conversion processes, for example, electrocatalysis, photoelectrocatalysis, and photocatalysis, for producing a broad range of chemicals and fuels and in environmental applications for organic dye decomposition. Much effort has already been made, and many more investigations are being

continued to develop an improved catalytic material to achieve high performance with different processes. Focusing on highly active catalytic materials, SPE—an engineering approach to tune the innate properties and functionalities at the nanoregime, depending on the various constituents and highly anisotropic structures—appears to increase the number of active sites and thereby increase the catalytic intrinsic activity, which is essential for these redox reaction systems. SPE strategies can be used to tune the atomic-level thickness, reduce lateral sizes, direct bandgap, generate sulfur vacancies/defects, perform crystal phase engineering, and so forth. A vast number of materials show phase(s) that are significantly different from one to another in terms of catalytic activity. Of the known phase-based materials, MoS_2 has been studied extensively in numerous redox reactions such as those discussed above owing to an excellent thermodynamic understanding of its hydrogen adsorption energy. Considering the benefits of MoS_2 relative to those of similar materials, most of the studied redox reaction mechanisms have been related to electrochemical applications, while the mechanisms are less understood for photocatalytic applications. Nevertheless, the limitations relating to HER, OER, and ORR, are the sluggish kinetics and overall energy loss phenomena, which influence the overall efficiency of those processes. Using renewable energy as an input, CO_2 reduction in the presence of light not only produces value-added products but also reduces the dependence on fossil fuels—a major advantage in achieving effective energy technologies. This is a multielectron reduction reaction system that involves a number of various surface-bound reaction intermediates that increase the process complexity in practical applications. Given the tremendous achievements regarding the abovementioned redox reactions, there remains plenty of room for progress, where SPE can be envisaged to facilitate major breakthroughs in this field. Further studies are also necessary to demonstrate in-depth details about the electrode–electrolyte interface that remain less understood to date. Studies such as those investigating synthetic methods are also important in the SPE framework, while understanding the kinetics and reaction barriers of key elementary reactions with different phases represents the frontier of current energy conversion processes.

5.1. Phase Engineering in Different Redox Reactions—Laterally Referenceable versus Uniquely Applicable

Throughout this work, we have seen that the 1T and 1T′ phases of MoS_2 are applicable in electrocatalysis, photocatalysis and photoelectrocatalysis processes for energy and environmental applications because of their structural properties. With differing electronic band structures and DOS, their application extends from water splitting to environmental pollutant degradation, while various results have been reported regarding improved catalytic activities. To achieve high-performance electrocatalytic HER, many studies have focused on the preparation of the $1T$-MoS_2 phase from its 2H phase and have compared their activities with those in similar works, even with the bulk material. However, depending on the nature of the analyzed reaction, the functionalized 2H phase of MoS_2 can be more effective than and show superior activity compared to the 1T phase, for example, in pollutant degradation. Apart from such experimental investigations, one may combine preferred phase(s) with preferred nanostructures to improve HER performance. For example, the intercalation of lithium ions into the van der Waals gap of MoS_2 can transform the phase from the semiconducting 2H phase to the metallic 1T phase and may allow construction of vertically aligned MoS_2 nanostructures (nanosheets, nanorods, nanowalls, and so on) to increase the catalytic performance. Another architecture along this line is the formation of the 1T/1T′ phase or 1T/2H phase in appropriate electrocatalysts, which can be tuned with surface functionalization to result in unique physical and chemical properties derived from quantum confinement and surface defects. With SPE strategies, it is significantly important to increase the abundance of active sites in the basal plane of the 1T phase compared with the 2H phase since the basal plane has more exposed surface area, while increasing the abundance edge active sites is equally appealing. Moreover, creating sulfur vacancies with strain engineering can potentially boost HER performance. The use of the 1T phase as a cocatalyst with semiconductor materials is another approach that can enhance the electrochemical activity of HER systems. One promising strategy to boost HER activity is the construction of multimetallic nanomaterials with different phases, for example, 4H/fcc-Au@MoX$_2$ (X = Se and S). We find that such a preparation strategy is unique and applicable for HER in acidic medium. Apart from studies on the HER, very few studies have reported the use of SPE strategies to address the ORR and OER, necessitating much more experimental work with a variety of phase-based materials. The electrocatalytic OWS reaction has just been studied using the 1T phase with a hybrid nanostructure, and further design of multiple heterointerfaces may reveal the intrinsic activities of electrocatalysts to hence improve the OWS efficiency.

In photocatalysis, the obvious problems, for example, charge-carrier recombination, light absorption range, quantum efficiency and so on, still need to be resolved since these issues are more likely related to photocatalytic nanostructural properties. Adding cocatalytic materials to the semiconductor surface could improve the photocatalytic activities, providing more hydrogen reduction sites and reducing the activation energy to ultimately accelerate proton reduction. Designing an intraplane heterojunction with a 2D semiconductor can help reduce charge recombination because the different phases may enable diverse physical and chemical properties in the same plane, improving the HER performance. Additionally, such fabrication through van der Waals interactions minimizes the Schottky barrier or even eliminates the barrier, which is important for charge transfer on the surface. Phase-based perovskite catalytic materials may reveal potential for hydrogen generation under light irradiation.

The study of PC-OWS has been limited to a mixed-phase $γ/β$-Ga_2O_3 system, leaving significant room for improvement with other phase-based materials such as $1T$-MoS_2 or similar materials; of course, combination with a versatile semiconductor could drive the photocatalytic activity in a progressive manner due to the accelerated charge separation at the phase junction. The construction of a phase junction with a

periodic arrangement of various crystal phases along a preferred orientation is uniquely efficient in separating photoinduced charges and contributes to the prolonged lifetime of the photogenerated holes and electrons. The reason is because at the atomic level, the vectorial separation and transfer of the photoinduced charge carriers with periodic phase interfaces leads to improved performance for H_2 formation from PEC-OWS. However, the scarcity of PEC-OWS studies using SPE indicates that there are many opportunities for the scientific community to work more in this field. A potential semiconductor with an appropriate bandgap window is a requirement in a photocatalytic CRR system; additionally, a phase transition can shift the band position from its original point, which can alternatively be seen as a band edge engineering approach, and this is essential for improving CRR efficiency. Proper utilization of the produced hole at the source point is needed since it may increase the charge-carrier recombination rate, resulting in a decreased electron lifetime. The TiO_2 sample fabricated by SPE is laterally applicable in the photodriven CRR because of its three typical phases, namely, anatase, brookite, and rutile, while the scenario for photoelectric activity is more complex over some phases than others, warranting further study. Other phase-based materials, for example, cubic and orthorhombic $NaNbO_3$, have been observed to prolong the lifetime of the electron–hole pair in the mixed-phase junction and hence improve the CRR performance. MnO_2 catalysts, which possess α, β, γ, δ, η, and ε phases, are frequently used in photocatalytic dye degradation due to the diverse d bandgap energies and good adsorption ability toward reactants. While brookite TiO_2 shows lower performance in PC-CRR than do the other phases, its higher photodegradation activity in PEC-AOPs justifies not only the efficacy of its structural properties but also its applicability for other photocatalytic processes. Additionally, different phases of 2D TMD materials with semiconductor materials represent a viable option in this regard, and such advancement will further guide and inform the scientific community with respect to both theory and experiment, which will enable the use of catalysts with near-ideal efficiency and selectivity.

A knowledge of SPE is of great significance to those studying nanomaterials for environmental treatment. As reviewed, the surface properties, thermostability, conductivity, and composition of the single or mixed phases have notable effects on the ultimate properties and catalytic performance of the catalysts. Accordingly, it may be desirable to deliberately improve or inhibit the phase transformation to select the most suitable phase or mixed phase for a given application. Consideration of the mechanisms by which phase transitions are promoted or restricted will, in turn, enable the rational design of regulation strategies (e.g., annealing temperature, foreign ion doping) and help us predict the effects that these strategies are likely to have on the final materials. Such efforts can eventually facilitate optimization of catalysts for efficient environmental treatment.

5.2. Enhancement of Balance between Catalytic Activity, Selectivity, and Stability

To realize a fossil-free route to produce fuels and chemicals utilizing the above redox reactions, high-performance catalytic materials must be designed and architected that exhibit improved activity, selectivity, and durability; moreover, SPE could uncover broader physical properties of the catalytic materials, such as charge-carrier separation and transport in the bulk and on surfaces. For a given reaction system, favorable activity and selectivity of the catalytic materials can be achieved either by improving the structural properties to expose more active sites per unit or by enhancing the intrinsic activity of each active site. These strategies for improving the catalytic activity and selectivity cannot be achieved straightforwardly, but they need to be accounted for simultaneously. Nano-to-atomic structural phase engineering allows manipulating the nanostructure to have a substantial fraction of exposed active edge sites, especially in the case of MoS_2, which is a prerequisite for higher activity and unusual selectivity in a redox system. In contrast to this result, it was also observed that the basal plane of MoS_2 could be more catalytically active than the $1T$-MoS_2 active edge sites. However, the nature of the reaction medium plays a vital role in electrocatalysis; therefore, strategies for improving catalyst activity and selectivity require careful selection from many existing materials and methods. Nevertheless, the extensive crystal-phase engineering of MoS_2-based catalysts over the years has achieved remarkable success in improving the activity and selectivity of the materials, with plenty of room left for further progress. Such developments will include designing materials with a higher fraction of active edge sites while reducing the kinetic energy barrier for the redox system, the latter of which is a criterion for a material to be considered an active catalyst.

In parallel with electrocatalytic processes, the catalytic activity and selectivity in photocatalysis are largely dependent on light harvesting, suitable bandgap materials, and charge-carrier separation and migration, among many other factors. We have seen throughout this work that the SPE approach was used to tune light harvesting phenomena, which is related to bandgap engineering of the materials. In photocatalysis, the phase-dependent surface reaction mechanism is governed by the redox potentials of illuminated charge carriers, which depend on the electronic structure and the ability of the surface atomic rearrangement to adsorb and activate reactant molecules. Such a phase-dependent reaction has one notable shortcoming: the recombination of the charge carriers before reaching the reaction sites. Therefore, increasing the charge transfer and subsequently reducing the charge-carrier recombination could be a promising route to improve the photocatalytic performance. The electronic structures of the different crystal phases of photocatalytic materials significantly affect the charge transfer behaviors and their selectivity for final product formation. As we have seen for $NaNbO_3$ in this study, the photocatalytic H_2 evolution activity and selectivity with the cubic $NaNbO_3$ phase were almost twice those of the orthorhombic $NaNbO_3$ phase. Theoretical studies of the electronic structures revealed that the CB of the orthorhombic $NaNbO_3$ phase was less dispersive than that of the cubic $NaNbO_3$ phase, indicating a smaller effective mass of the illuminated electrons in the cubic $NaNbO_3$ phase, which was responsible for the increased photoactivity and selectivity of the materials. Increasing the electron–hole separation time is an alternative means to boost the photocatalytic activity of the materials. Taking Ga_2O_3 as an example, an

**ADVANCED
SCIENCE NEWS**

www.advancedsciencenews.com

**ADVANCED
MATERIALS**

www.advmat.de

enhanced water-splitting performance was realized by engineering α–β phase junctions on the surface, while the positions of the CB and VB of β-Ga_2O_3 were more positive than those of α-Ga_2O_3. Upon light irradiation, the photoinduced electrons migrate from the α phase to the β phase, while the generated holes tend to move from the β phase to the α phase due to the potential difference. Here, we noticed that photoinduced electrons and holes can be spatially separated and migrate to two different phases, where they eventually accumulate. Adopting this strategy, one can reduce the charge recombination while improving the photocatalytic activity and selectivity in HER and OER. However, there has been misleading information in certain published articles in which simple mixtures of different crystal phases of the materials were identified as phase junctions. In a phase-junction material, a well-defined interface between the different phases is required, which prolongs the electron—hole separation and hence promotes the photocatalytic activity for a given redox reaction.

The duration that a catalytic material can remain active and selective for products within a given reaction system is mainly dependent on the intrinsic activity of that material, which is a direct function of the electronic structure as well as the active site density. We refer to this as stability here—one of the crucial indicators in determining the performance of catalytic materials. In electrocatalysis, understanding the stability of catalytic materials is a longstanding challenge, and much effort needs to be made. The reason is that the reaction medium in electrocatalysis is either an alkaline or acidic environment, resulting in the subsequent dissolution and corrosion of the catalytic materials over the course of the reaction. To prolong the lifetime of catalytic materials, phase-transformation engineering is an option, which can overcome the sluggish reaction kinetics and increase the abundance of the active sites. One study, for example, shows that a 1T–2H-MoS_2 phase junction synthesized by a selective controlled process has much higher electrical conductivity than that of other phases, which is beneficial for obtaining enhanced HER electrocatalytic activity from water splitting during operation for ≈500 d. However, a deeper understanding and application of advanced computational studies and the utilization of sophisticated characterization tools to evaluate the working states of catalytic materials and the nature of their active sites is required to achieve progress in the field of electrocatalysis, especially in the context of stability.

Generally, the stability of photocatalysis and photoelectrocatalysis is somewhat linked with the catalytic materials' ability to absorb light and facilitate charge transfer and migration as well as surface reactions through photocatalyst phase engineering. As long as the photoinduced charge carrier can remain separated from recombination and migrate to the surface where it can bind with the reactant molecule, thereby forming products, the photocatalyst may be recognized as a durable material. To achieve such operating functions for a given photocatalytic material, SPE can be effective in accelerating the charge kinetics because the electronic structure of the material can significantly affect the charge behavior. For example, construction of the 1T′–2H phase junction of MoS_2 significantly boosts the charge-carrier mobility, which increases the photocatalytic and photo-electrocatalytic performance as well as the stability in the water-splitting reaction.

Overall, the development of phase-dependent catalytic materials has achieved much progress to date, but there remain serious challenges to be researched in the future. In heterophase engineering, the phase mixture ratio is still not precisely designed and controlled, while in single-phase engineering, the greatest concern is the stability and purity of the desired phase. The activity of catalysts utilized in environmental treatment is highly influenced by their surface phase structure and chemical properties. Opportunities for improvement in the future involve developing and elucidating innovative methods for phase engineering. In brief, the future study of phase engineering at the nanoscale will focus on the following aspects: 1) developing refined technologies for phase transformation to precisely regulate the band structure and matching degree of the heterojunction energy band; and 2) designing suitable preparation methods to construct multi-, hetero-, or single-phase structures that can expose the desired crystal face to the greatest extent.

5.3. Understanding of Solid/Liquid/Gas Interface Dynamics in the Whole Redox System

Generally, these redox reactions proceed within a system where the solid catalytic materials remain in contact with liquid and gas phases. A rich variety of elementary reaction and energy transfer processes occur at the solid-liquid-gas interface, and such reactions are highly complex and interrelated. Interfacial surface reactions are critical for overall redox reactions, including those with water, hydrogen, and oxygen, in the sense that without having any detailed understanding of the relevant interfacial surface reactions, it may be strenuous work to design and modulate the proper catalytic materials. At the interfacial junction (where the three phases meet), many of the reactive intermediates form and bind as adsorbed species over the course of the reaction. Knowledge of the kinetics and dynamics of the formed reactive intermediates is the key to fabricating materials with enhanced activity. However, an understanding of such reaction mechanisms and how they subsequently explain the catalytic materials remains elusive; for example, reports on the HER evolution mechanism and dynamics over the 1T-MoS_2 electrocatalyst have yielded different opinions and conclusions. The reason for such variability is that MoS_2 is a polymorphic material, and its different phases show different electronic properties and mechanisms as well as different approaches when examining the redox processes. Within this work, we have highlighted that 1T-MoS_2 nanosheets possess improved electrical transport and higher charge transfer kinetics at the interface as well as high reactivity toward surface covalent functionalization. With DFT calculations, it was verified that the chemical treatment of bulk MoS_2 induces a higher tendency of H to bind to the basal plane of 1T-MoS_2 as opposed to 2H-MoS_2. Another aspect of 1T-MoS_2 nanosheets regards the much higher surface area with respect to the edge portion, which is beneficial for functionalization with the adsorbed H atom. For electrocatalysis in an acidic environment, the adsorbed H atom plays a key role in the overall redox reaction. The overall redox reaction rate is largely determined by the atomic hydrogen adsorption free energy on the catalyst surface,

**ADVANCED
SCIENCE NEWS**

www.advancedsciencenews.com

**ADVANCED
MATERIALS**

www.advmat.de

ΔG_H. Depending on the ΔG_H values, the adsorption and desorption processes on the surface may limit the overall reaction rate. Ideally, an active catalyst for HER has ΔG_H values close to zero, indicating that an active catalytic material binds reaction intermediate(s) neither too weakly nor too strongly. Reducing protons into hydrogen by the HER in acidic environments may follow either the Volmer–Heyrovsky or Volmer–Tafel mechanism. The conversion of protons from the acid solution into adsorbed H ($H^+ + e^- \rightarrow H_{ad}$) is referred to as the Volmer reaction, which occurs very quickly. When a solvated proton from the water layer combines with one H_{ad} and forms H_2 ($H_{ad} + H^+ + e^- \rightarrow H_2$), this is known as the Volmer–Heyrovsky mechanism, while when the reaction between two surface H_{ad} species leads to H_2, it is known as the Volmer–Tafel mechanism. It is worth noting here that the Volmer–Tafel mechanism is largely related to the surface hydrogen coverage because there is no charge transfer involved in this process. Theoretical studies show that the HER mechanism follows the Heyrovsky reaction because the adsorption hydrogen energy for the Heyrovsky step is much lower than that for the Tafel reaction. This result indicates that the Heyrovsky reaction proceeds very rapidly over 1T-MoS_2 at an electrode potential of -0.22 V along with 25% hydrogen coverage. As opposed to the Heyrovsky reaction, the Tafel slope is recognized as an intrinsic property of the electrocatalysts—largely determined by the rate-limiting step—and gives hints about the possible reaction mechanism of the HER. Using the same ΔG_H scale, however, some research groups reported that both the edge sites and basal plane of 1T-MoS_2 are effective for HER. Therefore, in future research, one should take care when considering the HER mechanism with phase-dependent catalytic materials and explain them in terms of the reaction products.

The surface reaction dynamics in photocatalysis and photocatalysis are complicated due to the involvement of light, band position of the analyzed materials, redox properties of the photoinduced electrons and holes, and excitons, among many others. The complexity of the surface dynamics for the above processes is further elaborated when one considers crystal phase-dependent photocatalytic materials because different phases have altered surface atomic configurations. In photocatalysis, the catalytic reactions take place first, while charge-carrier separation and migration typically proceed afterwards. The reactant molecules can adsorb on the catalyst surface either molecularly or dissociatively during surface reactions, followed by the addition of photoinduced electrons or holes to undergo the half reduction or half oxidation reaction. Next, the formed products from the surface would desorb and diffuse into the atmosphere. In exceptional cases, the formed reactive intermediate(s) can return to the reaction site again and contribute further to the catalytic reaction. As we noted earlier, the surface atomic arrangement is the key factor in crystal phase-dependent reaction dynamics because such atomic arrangement can control the adsorption, activation of reactant molecules and reaction coordinates. For instance, thermodynamically, the rutile (110) and anatase (101) facets are the most stable surfaces among many TiO_2 single crystals, although other facets with higher surface energy can be realized with controlled thermodynamics and kinetics. It has been established that kinetically, the rutile (110) facet is more active than the anatase (101) facet for water splitting. The surface energy of the rutile (110) facet for O–H bond cleavage was determined to be nearly ≈ 0.2 eV lower than that of the anatase (101) facet. The validated explanation for this observation is the much more favorable local bonding geometry of the surface for the rutile (110) facet. The surface structure of TiO_2 has a significant effect on the reaction pathway because the oxygen atoms in rutile and anatase have different geometries. Compared with rutile, anatase shows low photocatalytic performance in terms of oxygen evolution, with O_2 evolution on the anatase surface followed by two-electron migration pathways, which is less favorable and very different from the single-electron transfer pathway. The surface reaction in photocatalysis may be accelerated by means of defective photocatalysts because defective catalytic materials possess dangling bonds and coordinatively unsaturated atoms at the steps, terraces, adatoms, vacancies, and kinks, which are thermodynamically unstable but provide stimuli for reactant molecule adsorption and activation with the aid of photogenerated electrons or holes. It was reported that the formation of Ti^{3+} sites and surface oxygen vacancies on the surface could activate CO_2 by forming $CO_2\bullet$ intermediates, which remarkably increased the photoreduction of CO_2 with water over defective TiO_2. The defective brookite polymorphs show excellent photoactivity in terms of CH_4 and CO production, which is linked to their relatively lower formation energy of oxygen vacancies and the presence of HCOOH intermediates. As we have pointed out, the surface reactions are largely dependent on the contribution from the reactant source, radicals/intermediates, reaction pathway, diffusion dynamics of the formed products and transformation, while the redox properties of the light-induced electrons and holes also help to activate surface molecules. If the positions of the CB and VB of the given photocatalysts are more negative or positive than the redox potential for reduction or oxidation, then only photogenerated electrons or holes can drive the surface reactions. For future study, understanding the solid/liquid/gas interface dynamics together with the reductive/oxidative properties of the active electrons/holes in the whole redox system represents a challenging but useful research strategy.

All the reviewed results have proven that structural phase engineering offers opportunities to conduct both fundamental and applied environmental treatment research. However, how phase engineering affects the activity of the catalysts for pollutant degradation is still complicated. Specifically, the dynamics of ROS activation occurring at the solid/liquid interface of various phases is unclear. From the perspective of experimental characterization, a detailed understanding of phase transformation is also lacking. In future research, it will be necessary to use powerful in situ and transient technologies (e.g., in situ variable-temperature EPR spectroscopy) to interpret the mechanisms of the actual phase transformations and the corresponding ROS activation processes. In addition, some specific phase structures (e.g., α-MnO_2) show robust efficiency for pollutant degradation under PC-AOPs and FAOPs, and the essential distinction and relation of ROS activation with the same phase under different AOP configurations should be investigated. However, there are so many driving factors that need to be accounted for during photocatalysis because the photocatalytic materials combine various techniques and

parameters, and different reactants may behave differently during adsorption and activation on the photocatalyst surface.

Conflict of Interest

The authors declare no conflict of interest.

[1] M. Chhowalla, H. S. Shin, G. Eda, L.-J. Li, K. P. Loh, H. Zhang, *Nat. Chem.* **2013**, *5*, 263.

[2] J. Zhou, J. Lin, X. Huang, Y. Zhou, Y. Chen, J. Xia, H. Wang, Y. Xie, H. Yu, J. Lei, *Nature* **2018**, *556*, 355.

[3] X. Zhang, Z. Lai, Q. Ma, H. Zhang, *Chem. Soc. Rev.* **2018**, *47*, 3301.

[4] Z. Fan, H. Zhang, *Chem. Soc. Rev.* **2016**, *45*, 63.

[5] L.-D. Zhao, S.-H. Lo, Y. Zhang, H. Sun, G. Tan, C. Uher, C. Wolverton, V. P. Dravid, M. G. Kanatzidis, *Nature* **2014**, *508*, 373.

[6] H. Wang, Z. Lu, S. Xu, D. Kong, J. J. Cha, G. Zheng, P.-C. Hsu, K. Yan, D. Bradshaw, F. B. Prinz, *Proc. Natl. Acad. Sci. USA* **2013**, *110*, 19701.

[7] Z. Zeng, Y. Yu, X. Quan, S. Chen, S. Zhang, *Appl. Catal., B* **2018**, *227*, 153.

[8] Q. Lu, Y. Yu, Q. Ma, B. Chen, H. Zhang, *Adv. Mater.* **2016**, *28*, 1917.

[9] X. Zong, G. Wu, H. Yan, G. Ma, J. Shi, F. Wen, L. Wang, C. Li, *J. Phys. Chem. C* **2010**, *114*, 1963.

[10] S. Karunakaran, S. Pandit, B. Basu, M. De, *J. Am. Chem. Soc.* **2018**, *140*, 12634.

[11] H. Xu, J. Yi, X. She, Q. Liu, L. Song, S. Chen, Y. Yang, Y. Song, R. Vajtai, J. Lou, *Appl. Catal., B* **2018**, *220*, 379.

[12] D. Voiry, H. Yamaguchi, J. Li, R. Silva, D. C. B. Alves, T. Fujita, M. Chen, T. Asefa, V. B. Shenoy, G. Eda, M. Chhowalla, *Nat. Mater.* **2013**, *12*, 850.

[13] W. Wang, M. O. Tade, Z. Shao, *Chem. Soc. Rev.* **2015**, *44*, 5371.

[14] C. A. Martínez-Huitle, M. A. Rodrigo, I. Sirés, O. Scialdone, *Chem. Rev.* **2015**, *115*, 13362.

[15] C. A. Martinez-Huitle, S. Ferro, *Chem. Soc. Rev.* **2006**, *35*, 1324.

[16] B. C. Hodges, E. L. Cates, J. H. Kim, *Nat. Nanotechnol.* **2018**, *13*, 642.

[17] R. Subbaraman, D. Tripkovic, D. Strmcnik, K.-C. Chang, M. Uchimura, A. P. Paulikas, V. Stamenkovic, N. M. Markovic, *Science* **2011**, *334*, 1256.

[18] C. Wei, R. R. Rao, J. Peng, B. Huang, I. E. Stephens, M. Risch, Z. J. Xu, Y. Shao-Horn, *Adv. Mater.* **2019**, *31*, 1806296.

[19] C. Niether, S. Faure, A. Bordet, J. Deseure, M. Chatenet, J. Carrey, B. Chaudret, A. Rouet, *Nat. Energy* **2018**, *3*, 476.

[20] S. Chen, T. Takata, K. Domen, *Nat. Rev. Mater.* **2017**, *2*, 17050.

[21] W. H. Glaze, J.-W. Kang, D. H. Chapin, *Ozone: Sci. Eng.* **1987**, *9*, 335.

[22] K. Sun, Y. Liu, Y. Pan, H. Zhu, J. Zhao, L. Zeng, Z. Liu, C. Liu, *Nano Res.* **2018**, *11*, 4368.

[23] Z. W. Seh, J. Kibsgaard, C. F. Dickens, I. Chorkendorff, J. K. Nørskov, T. F. Jaramillo, *Science* **2017**, *355*, eaad4998.

[24] H. Jin, C. Guo, X. Liu, J. Liu, A. Vasileff, Y. Jiao, Y. Zheng, S.-Z. Qiao, *Chem. Rev.* **2018**, *118*, 6337.

[25] Q. Liu, X. Li, Z. Xiao, Y. Zhou, H. Chen, A. Khalil, T. Xiang, J. Xu, W. Chu, X. Wu, *Adv. Mater.* **2015**, *27*, 4837.

[26] D. Rhodes, D. A. Chenet, B. E. Janicek, C. Nyby, Y. Lin, W. Jin, D. Edelberg, E. Mannebach, N. Finney, A. Antony, T. Schiros, T. Klarr, A. Mazzoni, M. Chin, Y. c. Chiu, W. Zheng, Q. R. Zhang, F. Ernst, J. I. Dadap, X. Tong, J. Ma, R. Lou, S. Wang, T. Qian, H. Ding, R. M. Osgood, D. W. Paley, A. M. Lindenberg, P. Y. Huang, A. N. Pasupathy, M. Dubey, J. Hone, L. Balicas, *Nano Lett.* **2017**, *17*, 1616.

[27] X. Fan, P. Xu, D. Zhou, Y. Sun, Y. C. Li, M. A. T. Nguyen, M. Terrones, T. E. Mallouk, *Nano Lett.* **2015**, *15*, 5956.

[28] K.-A. N. Duerloo, Y. Li, E. J. Reed, *Nat. Commun.* **2014**, *5*, 4214.

[29] S. Cho, S. Kim, J. H. Kim, J. Zhao, J. Seok, D. H. Keum, J. Baik, D.-H. Choe, K. J. Chang, K. Suenaga, *Science* **2015**, *349*, 625.

[30] Y. Wang, J. Xiao, H. Zhu, Y. Li, Y. Alsaid, K. Y. Fong, Y. Zhou, S. Wang, W. Shi, Y. Wang, *Nature* **2017**, *550*, 487.

[31] Y. Kang, S. Najmaei, Z. Liu, Y. Bao, Y. Wang, X. Zhu, N. J. Halas, P. Nordlander, P. M. Ajayan, J. Lou, *Adv. Mater.* **2014**, *26*, 6467.

[32] Q. Li, W. Niu, X. Liu, Y. Chen, X. Wu, X. Wen, Z. Wang, H. Zhang, Z. Quan, *J. Am. Chem. Soc.* **2018**, *140*, 15783.

[33] J. Wang, Y. Wei, H. Li, X. Huang, H. Zhang, *Sci. China: Chem.* **2018**, *61*, 1227.

[34] H. Cheng, N. Yang, Q. Lu, Z. Zhang, H. Zhang, *Adv. Mater.* **2018**, *30*, 1707189.

[35] K. Kusada, H. Kitagawa, *Adv. Mater.* **2016**, *28*, 1129.

[36] X. Huang, S. Tang, X. Mu, Y. Dai, G. Chen, Z. Zhou, F. Ruan, Z. Yang, N. Zheng, *Nat. Nanotechnol.* **2011**, *6*, 28.

[37] X. Huang, S. Li, Y. Huang, S. Wu, X. Zhou, S. Li, C. L. Gan, F. Boey, C. A. Mirkin, H. Zhang, *Nat. Commun.* **2011**, *2*, 292.

[38] R. He, J.-A. Yan, Z. Yin, Z. Ye, G. Ye, J. Cheng, J. Li, C. Lui, *Nano Lett.* **2016**, *16*, 1404.

[39] Y. Ma, X. Wang, Y. Jia, X. Chen, H. Han, C. Li, *Chem. Rev.* **2014**, *114*, 9987.

[40] W. J. Jo, H. J. Kang, K.-J. Kong, Y. S. Lee, H. Park, Y. Lee, T. Buonassisi, K. K. Gleason, J. S. Lee, *Proc. Natl. Acad. Sci. USA* **2015**, *112*, 13774.

[41] D. Lang, Q. Xiang, G. Qiu, X. Feng, F. Liu, *Dalton Trans.* **2014**, *43*, 7245.

[42] D. Wang, Y. Xiao, X. Luo, Z. Wu, Y.-J. Wang, B. Fang, *ACS Sustainable Chem. Eng.* **2017**, *5*, 2509.

[43] S. Wang, D. Zhang, B. Li, C. Zhang, Z. Du, H. Yin, X. Bi, S. Yang, *Adv. Energy Mater.* **2018**, *8*, 1801345.

[44] Y. Yin, Y. Zhang, T. Gao, T. Yao, X. Zhang, J. Han, X. Wang, Z. Zhang, P. Xu, P. Zhang, *Adv. Mater.* **2017**, *29*, 1700311.

[45] K. Chang, X. Hai, H. Pang, H. Zhang, L. Shi, G. Liu, H. Liu, G. Zhao, M. Li, J. Ye, *Adv. Mater.* **2016**, *28*, 10033.

[46] I. H. Kwak, I. S. Kwon, H. G. Abbas, G. Jung, Y. Lee, T. T. Debela, S. J. Yoo, J.-G. Kim, J. Park, H. S. Kang, *Nanoscale* **2018**, *10*, 14726.

[47] M. Naz, T. Hallam, N. C. Berner, N. McEvoy, R. Gatensby, J. B. McManus, Z. Akhter, G. S. Duesberg, *ACS Appl. Mater. Interfaces* **2016**, *8*, 31442.

**ADVANCED
SCIENCE NEWS**

www.advancedsciencenews.com

**ADVANCED
MATERIALS**

www.advmat.de

[48] R. J. Toh, Z. Sofer, J. Luxa, D. Sedmidubský, M. Pumera, *Chem. Commun.* **2017**, *53*, 3054.

[49] P. Zhang, J. Zhang, J. Gong, *Chem. Soc. Rev.* **2014**, *43*, 4395.

[50] M. Acerce, D. Voiry, M. Chhowalla, *Nat. Nanotechnol.* **2015**, *10*, 313.

[51] S. S. Chou, N. Sai, P. Lu, E. N. Coker, S. Liu, K. Artyushkova, T. S. Luk, B. Kaehr, C. J. Brinker, *Nat. Commun.* **2015**, *6*, 8311.

[52] L. Liu, H. Zhao, J. M. Andino, Y. Li, *ACS Catal.* **2012**, *2*, 1817.

[53] P. Du, Y. Zhu, J. Zhang, D. Xu, W. Peng, G. Zhang, F. Zhang, X. Fan, *RSC Adv.* **2016**, *6*, 74394.

[54] A. N. Enyashin, L. Yadgarov, L. Houben, I. Popov, M. Weidenbach, R. Tenne, M. Bar-Sadan, G. Seifert, *J. Phys. Chem. C* **2011**, *115*, 24586.

[55] Y. Cheng, A. Nie, Q. Zhang, L.-Y. Gan, R. Shahbazian-Yassar, U. Schwingenschlogl, *ACS Nano* **2014**, *8*, 11447.

[56] Z. Liu, N. Li, C. Su, H. Zhao, L. Xu, Z. Yin, J. Li, Y. Du, *Nano Energy* **2018**, *50*, 176.

[57] I. Chakraborty, S. N. Shirodkar, S. Gohil, U. V. Waghmare, P. Ayyub, *J. Phys: Condens. Matter* **2013**, *26*, 025402.

[58] J.-H. Ahn, M.-J. Lee, H. Heo, J. H. Sung, K. Kim, H. Hwang, M.-H. Jo, *Nano Lett.* **2015**, *15*, 3703.

[59] Z. Fan, Y. Chen, Y. Zhu, J. Wang, B. Li, Y. Zong, Y. Han, H. Zhang, *Chem. Sci.* **2017**, *8*, 795.

[60] Y. Chen, Z. Fan, Z. Zhang, W. Niu, C. Li, N. Yang, B. Chen, H. Zhang, *Chem. Rev.* **2018**, *118*, 6409.

[61] G. Gao, Y. Jiao, F. Ma, Y. Jiao, E. Waclawik, A. Du, *J. Phys. Chem. C* **2015**, *119*, 13124.

[62] A. Massa, S. Hernández, A. Lamberti, C. Galletti, N. Russo, D. Fino, *Appl. Catal., B* **2017**, *203*, 270.

[63] S. Abaci, U. Tamer, K. Pekmez, A. Yildiz, *Appl. Surf. Sci.* **2005**, *240*, 112.

[64] S. Devaraj, N. Munichandraiah, *J. Phys. Chem. C* **2008**, *112*, 4406.

[65] P. Chen, K. Xu, S. Tao, T. Zhou, Y. Tong, H. Ding, L. Zhang, W. Chu, C. Wu, Y. Xie, *Adv. Mater.* **2016**, *28*, 7527.

[66] T. Zhang, K. Zhao, J. Yu, J. Jin, Y. Qi, H. Li, X. Hou, G. Liu, *Nanoscale* **2013**, *5*, 8375.

[67] Y. Zhu, Q. Ling, Y. Liu, H. Wang, Y. Zhu, *Phys. Chem. Chem. Phys.* **2015**, *17*, 933.

[68] T. Ruttrell, S. Halpegamage, J. Tao, *Sci. Rep.* **2015**, *4*, 4043.

[69] Q. M. Jie Cao, L. Shi, Y. Qian, *J. Mater. Chem.* **2011**, *21*, 16210.

[70] C. A. Martinez-Huitle, M. A. Rodrigo, I. Sires, O. Scialdone, *Chem. Rev.* **2015**, *115*, 13362.

[71] W. Vielstich, H. A. Gasteiger, H. Yokokawa, *Handbook of Fuel Cells: Fundamentals Technology and Applications: Advances in Electrocatalysis, Materials, Diagnostics and Durability*, Vol. *5*, John Wiley & Sons, New York **2009**.

[72] D. Voiry, H. S. Shin, K. P. Loh, M. Chhowalla, *Nat. Rev. Chem.* **2018**, *2*, 0105.

[73] J. Zheng, W. Sheng, Z. Zhuang, B. Xu, Y. Yan, *Sci. Adv.* **2016**, *2*, e1501602.

[74] Z. Zeng, K.-C. Chang, J. Kubal, N. M. Markovic, J. Greeley, *Nat. Energy* **2017**, *2*, 17070.

[75] E. Skúlason, G. S. Karlberg, J. Rossmeisl, T. Bligaard, J. Greeley, H. Jónsson, J. K. Nørskov, *Phys. Chem. Chem. Phys.* **2007**, *9*, 3241.

[76] Q. Tang, D.-E. Jiang, *Chem. Mater.* **2015**, *27*, 3743.

[77] M. A. Lukowski, A. S. Daniel, F. Meng, A. Forticaux, L. Li, S. Jin, *J. Am. Chem. Soc.* **2013**, *135*, 10274.

[78] D. Voiry, M. Salehi, R. Silva, T. Fujita, M. Chen, T. Asefa, V. B. Shenoy, G. Eda, M. Chhowalla, *Nano Lett.* **2013**, *13*, 6222.

[79] J. Yang, K. Wang, J. Zhu, C. Zhang, T. Liu, *ACS Appl. Mater. Interfaces* **2016**, *8*, 31702.

[80] S. M. Tan, A. Ambrosi, Z. Sofer, Š. Huber, D. Sedmidubský, M. Pumera, *Chem. - Eur. J.* **2015**, *21*, 7170.

[81] Y. Wan, Z. Zhang, X. Xu, Z. Zhang, P. Li, X. Fang, K. Zhang, K. Yuan, K. Liu, G. Ran, *Nano Energy* **2018**, *51*, 786.

[82] Y. Yin, J. Han, Y. Zhang, X. Zhang, P. Xu, Q. Yuan, L. Samad, X. Wang, Y. Wang, Z. Zhang, P. Zhang, X. Cao, B. Song, S. Jin, *J. Am. Chem. Soc.* **2016**, *138*, 7965.

[83] D. Li, W. Zhou, Q. Zhou, G. Ye, T. Wang, J. Wu, Y. Chang, J. Xu, *Nanotechnology.* **2017**, *28*, 395401.

[84] Z. Lai, A. Chaturvedi, Y. Wang, T. H. Tran, X. Liu, C. Tan, Z. Luo, B. Chen, Y. Huang, G.-H. Nam, Z. Zhang, Y. Chen, Z. Hu, B. Li, S. Xi, Q. Zhang, Y. Zong, L. Gu, C. Kloc, Y. Du, H. Zhang, *J. Am. Chem. Soc.* **2018**, *140*, 8563.

[85] L. Najafi, S. Bellani, R. Oropesa-Nuñez, A. Ansaldo, M. Prato, A. E. Del Rio Castillo, F. Bonaccorso, *Adv. Energy Mater.* **2018**, *8*, 1703212.

[86] A. Ambrosi, Z. Sofer, M. Pumera, *Chem. Commun.* **2015**, *51*, 8450.

[87] I. H. Kwak, I. S. Kwon, H. G. Abbas, G. Jung, Y. Lee, J. Park, H. S. Kang, *J. Mater. Chem. A* **2018**, *6*, 5613.

[88] D. Wang, X. Zhang, S. Bao, Z. Zhang, H. Fei, Z. Wu, *J. Mater. Chem. A* **2017**, *5*, 2681.

[89] Z. Liu, X. Zhang, Y. Gong, Q. Lu, Z. Zhang, H. Cheng, Q. Ma, J. Chen, M. Zhao, B. Chen, *Nano Res.* **2019**, *12*, 1301.

[90] Z. Fan, Z. Luo, X. Huang, B. Li, Y. Chen, J. Wang, Y. Hu, H. Zhang, *J. Am. Chem. Soc.* **2016**, *138*, 1414.

[91] Z. Zhang, G. Liu, X. Cui, B. Chen, Y. Zhu, Y. Gong, F. Saleem, S. Xi, Y. Du, A. Borgna, *Adv. Mater.* **2018**, *30*, 1801741.

[92] H. Y. He, *Int. J. Hydrogen Energy* **2017**, *42*, 20739.

[93] S. Shi, D. Gao, B. Xia, P. Liu, D. Xue, *J. Mater. Chem. A* **2015**, *3*, 24414.

[94] Z. Liu, Z. Gao, Y. Liu, M. Xia, R. Wang, N. Li, *ACS Appl. Mater. Interfaces* **2017**, *9*, 25291.

[95] L. Cai, W. Cheng, T. Yao, Y. Huang, F. Tang, Q. Liu, W. Liu, Z. Sun, F. Hu, Y. Jiang, *J. Phys. Chem. C* **2017**, *121*, 15071.

[96] Z. Lai, A. Chaturvedi, Y. Wang, T. H. Tran, X. Liu, C. Tan, Z. Luo, B. Chen, Y. Huang, G.-H. Nam, *J. Am. Chem. Soc.* **2018**, *140*, 8563.

[97] W. Chen, J. Gu, Q. Liu, R. Luo, L. Yao, B. Sun, W. Zhang, H. Su, B. Chen, P. Liu, *ACS Nano* **2018**, *12*, 308.

[98] C. K. Chua, A. H. Loo, M. Pumera, *Chem. - Eur. J.* **2016**, *22*, 14336.

[99] N. H. Attanayake, A. C. Thenuwara, A. Patra, Y. V. Aulin, T. M. Tran, H. Chakraborty, E. Borguet, M. L. Klein, J. P. Perdew, D. R. Strongin, *ACS Energy Lett.* **2018**, *3*, 7.

[100] M. Jiang, J. Zhang, M. Wu, W. Jian, H. Xue, T.-W. Ng, C.-S. Lee, J. Xu, *J. Mater. Chem. A* **2016**, *4*, 14949.

[101] C. Tan, Z. Luo, A. Chaturvedi, Y. Cai, Y. Du, Y. Gong, Y. Huang, Z. Lai, X. Zhang, L. Zheng, *Adv. Mater.* **2018**, *30*, 1705509.

[102] S. X. Leong, C. C. Mayorga-Martinez, X. Chia, J. Luxa, Z. k. Sofer, M. Pumera, *ACS Appl. Mater. Interfaces* **2017**, *9*, 26350.

[103] Y. Qu, H. Medina, S. W. Wang, Y. C. Wang, C. W. Chen, T. Y. Su, A. Manikandan, K. Wang, Y. C. Shih, J. W. Chang, *Adv. Mater.* **2016**, *28*, 9831.

[104] T. F. Jaramillo, K. P. Jørgensen, J. Bonde, J. H. Nielsen, S. Horch, I. Chorkendorff, *Science* **2007**, *317*, 100.

[105] T. Fujita, Y. Ito, Y. Tan, H. Yamaguchi, D. Hojo, A. Hirata, D. Voiry, M. Chhowalla, M. Chen, *Nanoscale* **2014**, *6*, 12458.

[106] X. Zhang, Y. Y. Zhang, Y. Zhang, W. J. Jiang, Q. H. Zhang, Y. G. Yang, L. Gu, J. S. Hu, L. J. Wan, *Small Methods* **2018**, *3*, 1800317.

[107] J. K. Nørskov, J. Rossmeisl, A. Logadottir, L. Lindqvist, J. R. Kitchin, T. Bligaard, H. Jonsson, *J. Phys. Chem. B* **2004**, *108*, 17886.

[108] J. Luxa, V. Mazánek, M. Pumera, P. Lazar, D. Sedmidubský, M. Callisti, T. Polcar, Z. Sofer, *Chem. - Eur. J.* **2017**, *23*, 8082.

[109] C. Liu, H. Dong, Y. Ji, T. Hou, Y. Li, *Sci. Rep.* **2018**, *8*, 13292.

[110] T. Hong, T. Zhao, K. Brinkman, F. Chen, C. Xia, *ACS Appl. Mater. Interfaces* **2017**, *9*, 8659.

[111] K. Xu, H. Ding, M. Zhang, M. Chen, Z. Hao, L. Zhang, C. Wu, Y. Xie, *Adv. Mater.* **2017**, *29*, 1606980.

[112] Y. Xie, J. Cai, Y. Wu, Y. Zang, X. Zheng, J. Ye, P. Cui, S. Niu, Y. Liu, J. Zhu, *Adv. Mater.* **2019**, *31*, 1807780.

**ADVANCED
SCIENCE NEWS**

www.advancedsciencenews.com

**ADVANCED
MATERIALS**

www.advmat.de

[113] J. Wu, M. Liu, K. Chatterjee, K. P. Hackenberg, J. Shen, X. Zou, Y. Yan, J. Gu, Y. Yang, J. Lou, *Adv. Mater. Interfaces* **2016**, *3*, 1500669.

[114] Z. Fan, Z. Luo, Y. Chen, J. Wang, B. Li, Y. Zong, H. Zhang, *Small* **2016**, *12*, 3908.

[115] J. W. D. Ng, M. García-Melchor, M. Bajdich, P. Chakthranont, C. Kirk, A. Vojvodic, T. F. Jaramillo, *Nat. Energy* **2016**, *1*, 16053.

[116] C. Bae, T. A. Ho, H. Kim, S. Lee, S. Lim, M. Kim, H. Yoo, J. M. Montero-Moreno, J. H. Park, H. Shin, *Sci. Adv.* **2017**, *3*, e1602215.

[117] B. Zhang, X. Zheng, O. Voznyy, R. Comin, M. Bajdich, M. García-Melchor, L. Han, J. Xu, M. Liu, L. Zheng, *Science* **2016**, *352*, 333.

[118] Y. Liu, C. Xiao, M. Lyu, Y. Lin, W. Cai, P. Huang, W. Tong, Y. Zou, Y. Xie, *Angew. Chem.* **2015**, *127*, 11383.

[119] W. Xu, Z. Lu, P. Wan, Y. Kuang, X. Sun, *Small* **2016**, *12*, 2492.

[120] H. Li, S. Chen, Y. Zhang, Q. Zhang, X. Jia, Q. Zhang, L. Gu, X. Sun, L. Song, X. Wang, *Nat. Commun.* **2018**, *9*, 2452.

[121] H. Li, S. Chen, X. Jia, B. Xu, H. Lin, H. Yang, L. Song, X. Wang, *Nat. Commun.* **2017**, *8*, 15377.

[122] J. Zhang, T. Wang, D. Pohl, B. Rellinghaus, R. Dong, S. Liu, X. Zhuang, X. Feng, *Angew. Chem.* **2016**, *128*, 6814.

[123] I. C. Man, H. Y. Su, F. Calle-Vallejo, H. A. Hansen, J. I. Martínez, N. G. Inoglu, J. Kitchin, T. F. Jaramillo, J. K. Nørskov, J. Rossmeisl, *ChemCatChem* **2011**, *3*, 1159.

[124] X. Chen, S. Shen, L. Guo, S. S. Mao, *Chem. Rev.* **2010**, *110*, 6503.

[125] Z.-C. Zhao, C.-L. Yang, Q.-T. Meng, M.-S. Wang, X.-G. Ma, *Spectrochim. Acta, Part A* **2019**, *211*, 71.

[126] P. Ritterskamp, A. Kuklya, M. A. Wüstkamp, K. Kerpen, C. Weidenthaler, M. Demuth, *Angew. Chem., Int. Ed.* **2007**, *46*, 7770.

[127] Y. Hou, Z. Wen, S. Cui, X. Guo, J. Chen, *Adv. Mater.* **2013**, *25*, 6291.

[128] X. Zong, J. Han, G. Ma, H. Yan, G. Wu, C. Li, *J. Phys. Chem. C* **2011**, *115*, 12202.

[129] J. Low, J. Yu, M. Jaroniec, S. Wageh, A. A. Al-Ghamdi, *Adv. Mater.* **2017**, *29*, 1601694.

[130] Q. Lu, Z. Lu, Y. Lu, L. Lv, Y. Ning, H. Yu, Y. Hou, Y. Yin, *Nano Lett.* **2013**, *13*, 5698.

[131] Y. Yu, W. Yan, X. Wang, P. Li, W. Gao, H. Zou, S. Wu, K. Ding, *Adv. Mater.* **2018**, *30*, 1705060.

[132] X. Huang, Z. Zeng, H. Zhang, *Chem. Soc. Rev.* **2013**, *42*, 1934.

[133] M. Pandey, A. Vojvodic, K. S. Thygesen, K. W. Jacobsen, *J. Phys. Chem. Lett.* **2015**, *6*, 1577.

[134] U. Maitra, U. Gupta, M. De, R. Datta, A. Govindaraj, C. Rao, *Angew. Chem.* **2013**, *125*, 13295.

[135] J. Yi, X. She, Y. Song, M. Mao, K. Xia, Y. Xu, Z. Mo, J. Wu, H. Xu, H. Li, *Chem. Eng. J.* **2018**, *335*, 282.

[136] Q. Liu, X. Li, Q. He, A. Khalil, D. Liu, T. Xiang, X. Wu, L. Song, *Small* **2015**, *11*, 5556.

[137] Q. Liu, Q. Shang, A. Khalil, Q. Fang, S. Chen, Q. He, T. Xiang, D. Liu, Q. Zhang, Y. Luo, *ChemCatChem* **2016**, *8*, 2614.

[138] C. Wu, Q. Fang, Q. Liu, D. Liu, C. Wang, T. Xiang, A. Khalil, S. Chen, L. Song, *Inorg. Chem. Front.* **2017**, *4*, 663.

[139] H. Ou, L. Lin, Y. Zheng, P. Yang, Y. Fang, X. Wang, *Adv. Mater.* **2017**, *29*, 1700008.

[140] J. Liu, W. Fang, Z. Wei, Z. Qin, Z. Jiang, W. Shangguan, *Catal. Sci. Technol.* **2018**, *8*, 1375.

[141] W. Cui, S. Xu, B. Yan, Z. Guo, Q. Xu, B. G. Sumpter, J. Huang, S. Yin, H. Zhao, Y. Wang, *Adv. Electron. Mater.* **2017**, *3*, 1700024.

[142] R. Peng, L. Liang, Z. D. Hood, A. Boulesbaa, A. Puretzky, A. V. Ievlev, J. Come, O. S. Ovchinnikova, H. Wang, C. Ma, M. Chi, B. G. Sumpter, Z. Wu, *ACS Catal.* **2016**, *6*, 6723.

[143] P. Li, S. Ouyang, G. Xi, T. Kako, J. Ye, *J. Phys. Chem. C* **2012**, *116*, 7621.

[144] Y.-Q. Xu, S.-Y. Wu, C.-C. Ding, L.-N. Wu, G.-J. Zhang, *Chem. Phys.* **2018**, *504*, 66.

[145] Z.-X. Chang, W.-H. Zhou, D.-X. Kou, Z.-J. Zhou, S.-X. Wu, *Chem. Commun.* **2014**, *50*, 12726.

[146] S. Bai, L. Wang, X. Chen, J. Du, Y. Xiong, *Nano Res.* **2015**, *8*, 175.

[147] B. Mahler, V. Hoepfner, K. Liao, G. A. Ozin, *J. Am. Chem. Soc.* **2014**, *136*, 14121.

[148] H.-Y. He, H. He, Q. Shen, *J. Colloid Interface Sci.* **2018**, *522*, 136.

[149] H. Xu, S. Ouyang, P. Li, T. Kako, J. Ye, *ACS Appl. Mater. Interfaces* **2013**, *5*, 1348.

[150] L. Yan, J. Zhang, X. Zhou, X. Wu, J. Lan, Y. Wang, G. Liu, J. Yu, L. Zhi, *Int. J. Hydrogen Energy* **2013**, *38*, 3554.

[151] Q. He, Y. Wan, Y. Zhang, H. Jiang, H. Liu, X. Zheng, S. Chen, X. Wu, L. Song, *Sol. RRL* **2018**, *2*, 1800032.

[152] X.-B. Li, Y.-J. Gao, H.-L. Wu, Y. Wang, Q. Guo, M.-Y. Huang, B. Chen, C.-H. Tung, L.-Z. Wu, *Chem. Commun.* **2017**, *53*, 5606.

[153] J.-W. Shi, Y. Zou, D. Ma, Z. Fan, L. Cheng, D. Sun, Z. Wang, C. Niu, L. Wang, *Nanoscale* **2018**, *10*, 9292.

[154] K. Li, M. Han, R. Chen, S. L. Li, S. L. Xie, C. Mao, X. Bu, X. L. Cao, L. Z. Dong, P. Feng, *Adv. Mater.* **2016**, *28*, 8906.

[155] Y. Yang, G. Liu, J. T. Irvine, H. M. Cheng, *Adv. Mater.* **2016**, *28*, 5850.

[156] Y. Sakata, Y. Matsuda, T. Yanagida, K. Hirata, H. Imamura, K. Teramura, *Catal. Lett.* **2008**, *125*, 22.

[157] R. Roy, V. Hill, E. Osborn, *J. Am. Chem. Soc.* **1952**, *74*, 719.

[158] X. Wang, Q. Xu, M. Li, S. Shen, X. Wang, Y. Wang, Z. Feng, J. Shi, H. Han, C. Li, *Angew. Chem.* **2012**, *124*, 13266.

[159] S. Jin, X. Wang, X. Wang, M. Ju, S. Shen, W. Liang, Y. Zhao, Z. Feng, H. Y. Playford, R. I. Walton, C. Li, *J. Phys. Chem. C* **2015**, *119*, 18221.

[160] M.-G. Ju, X. Wang, W. Liang, Y. Zhao, C. Li, *J. Mater. Chem. A* **2014**, *2*, 17005.

[161] X. Li, J. Zhao, J. Yang, *Sci. Rep.* **2013**, *3*, 1858.

[162] Z. Qiao, Q. Xu, J. Jiang, *J. Mater. Chem. A* **2018**, *6*, 18898.

[163] X. Zhang, Z. Zhang, J. Liang, Y. Zhou, Y. Tong, Y. Wang, X. Wang, *J. Mater. Chem. A* **2017**, *5*, 9702.

[164] K. Sayama, H. Arakawa, *J. Phys. Chem.* **1993**, *97*, 531.

[165] R. Li, Y. Weng, X. Zhou, X. Wang, Y. Mi, R. Chong, H. Han, C. Li, *Energy Environ. Sci.* **2015**, *8*, 2377.

[166] M.-P. Crosnier-Lopez, F. Le Berre, J.-L. Fourquet, *J. Mater. Chem.* **2001**, *11*, 1146.

[167] K.-I. Shimizu, S. Itoh, T. Hatamachi, T. Kodama, M. Sato, K. Toda, *Chem. Mater.* **2005**, *17*, 5161.

[168] Y. Li, G. Chen, H. Zhang, Z. Li, J. Sun, *J. Solid State Chem.* **2008**, *181*, 2653.

[169] Z. Zou, J. Ye, K. Sayama, H. Arakawa, *Chem. Phys. Lett.* **2001**, *343*, 303.

[170] S. Bellani, M. R. Antognazza, F. Bonaccorso, *Adv. Mater.* **2019**, *31*, 1801446.

[171] Z. Yin, B. Chen, M. Bosman, X. Cao, J. Chen, B. Zheng, H. Zhang, *Small* **2014**, *10*, 3537.

[172] M. J. Kenney, M. Gong, Y. Li, J. Z. Wu, J. Feng, M. Lanza, H. Dai, *Science* **2013**, *342*, 836.

[173] Y. Pi, Z. Li, D. Xu, J. Liu, Y. Li, F. Zhang, G. Zhang, W. Peng, X. Fan, *ACS Sustainable Chem. Eng.* **2017**, *5*, 5175.

[174] S. N. Lou, R. Amal, J. Scott, Y. H. Ng, *ACS Appl. Energy Mater.* **2018**, *1*, 3955.

[175] W. D. Chemelewski, H.-C. Lee, J.-F. Lin, A. J. Bard, C. B. Mullins, *J. Am. Chem. Soc.* **2014**, *136*, 2843.

[176] F. Cao, J. Xiong, F. Wu, Q. Liu, Z. Shi, Y. Yu, X. Wang, L. Li, *ACS Appl. Mater. Interfaces* **2016**, *8*, 12239.

[177] A. Li, Z. Wang, H. Yin, S. Wang, P. Yan, B. Huang, X. Wang, R. Li, X. Zong, H. Han, *Chem. Sci.* **2016**, *7*, 6076.

[178] M. Liu, D. Jing, Z. Zhou, L. Guo, *Nat. Commun.* **2013**, *4*, 2278.

[179] H. Du, K. Liang, C.-Z. Yuan, H.-L. Guo, X. Zhou, Y.-F. Jiang, A.-W. Xu, *ACS Appl. Mater. Interfaces* **2016**, *8*, 24550.

[180] J. Tang, J. R. Durrant, D. R. Klug, *J. Am. Chem. Soc.* **2008**, *130*, 13885.

[181] I. Shown, S. Samireddi, Y.-C. Chang, R. Putikam, P.-H. Chang, A. Sabbah, F.-Y. Fu, W.-F. Chen, C.-I. Wu, T.-Y. Yu, P.-W. Chung, M. C. Lin, L.-C. Chen, K.-H. Chen, *Nat. Commun.* **2018**, *9*, 169.

[182] C. S. Diercks, Y. Liu, K. E. Cordova, O. M. Yaghi, *Nat. Mater.* **2018**, *17*, 301.

[183] P. V. Kamat, *J. Phys. Chem. Lett.* **2012**, *3*, 663.

[184] V. P. Indrakanti, J. D. Kubicki, H. H. Schobert, *Energy Environ. Sci.* **2009**, *2*, 745.

[185] E. Karamian, S. Sharifnia, *J. CO2 Util.* **2016**, *16*, 194.

[186] J. Tang, A. J. Cowan, J. R. Durrant, D. R. Klug, *J. Phys. Chem. C* **2011**, *115*, 3143.

[187] K. Niu, Y. Xu, H. Wang, R. Ye, H. L. Xin, F. Lin, C. Tian, Y. Lum, K. C. Bustillo, M. M. Doeff, *Sci. Adv.* **2017**, *3*, e1700921.

[188] X. Chang, T. Wang, J. Gong, *Energy Environ. Sci.* **2016**, *9*, 2177.

[189] J. Yu, J. Low, W. Xiao, P. Zhou, M. Jaroniec, *J. Am. Chem. Soc.* **2014**, *136*, 8839.

[190] Z. He, L. Wen, D. Wang, Y. Xue, Q. Lu, C. Wu, J. Chen, S. Song, *Energy Fuels* **2014**, *28*, 3982.

[191] J. Zhang, P. Zhou, J. Liu, J. Yu, *Phys. Chem. Chem. Phys.* **2014**, *16*, 20382.

[192] M. Xu, Y. Gao, E. M. Moreno, M. Kunst, M. Muhler, Y. Wang, H. Idriss, C. Wöll, *Phys. Rev. Lett.* **2011**, *106*, 138302.

[193] P. Maity, O. F. Mohammed, K. Katsiev, H. Idriss, *J. Phys. Chem. C* **2018**, *122*, 8925.

[194] S. Bai, N. Zhang, C. Gao, Y. Xiong, *Nano Energy* **2018**, *53*, 296.

[195] P. Kar, S. Zheng, Y. Zhang, E. Vahidzadeh, A. Manuel, R. Kisslinger, K. Alam, U. Thakur, N. Mahdi, P. Kumar, K. Shankar, *Appl. Catal., B* **2019**, *243*, 522.

[196] J. A. Benavides, C. Trudeau, L. F. Gerlein, S. G. Cloutier, *ACS Appl. Energy Mater.* **2018**, *1*, 3607.

[197] A. Kafizas, X. Wang, S. R. Pendlebury, P. Barnes, M. Ling, C. Sotelo-Vazquez, R. Quesada-Cabrera, C. Li, I. P. Parkin, J. R. Durrant, *J. Phys. Chem. A* **2016**, *120*, 715.

[198] P. Li, S. Ouyang, Y. Zhang, T. Kako, J. Ye, *J. Mater. Chem. A* **2013**, *1*, 1185.

[199] P. Li, H. Xu, L. Liu, T. Kako, N. Umezawa, H. Abe, J. Ye, *J. Mater. Chem. A* **2014**, *2*, 5606.

[200] W. Jiao, L. Wang, G. Liu, G. Q. Lu, H.-M. Cheng, *ACS Catal.* **2012**, *2*, 1854.

[201] B. S. Kwak, K. Vignesh, N.-K. Park, H.-J. Ryu, J.-I. Baek, M. Kang, *Fuel* **2015**, *143*, 570.

[202] M. Tahir, N. S. Amin, *Appl. Catal., B* **2015**, *162*, 98.

[203] P.-Q. Wang, Y. Bai, J.-Y. Liu, Z. Fan, Y.-Q. Hu, *Catal. Commun.* **2012**, *29*, 185.

[204] Y. Liu, B. Huang, Y. Dai, X. Zhang, X. Qin, M. Jiang, M.-H. Whangbo, *Catal. Commun.* **2009**, *11*, 210.

[205] C. A. Martı, S. Ferro, *Chem. Soc. Rev.* **2006**, *35*, 1324.

[206] P. Hu, M. Long, *Appl. Catal., B* **2016**, *181*, 103.

[207] F. Dong, Z. Zhao, T. Xiong, Z. Ni, W. Zhang, Y. Sun, W.-K. Ho, *ACS Appl. Mater. Interfaces* **2013**, *5*, 11392.

[208] Y. Lu, G. Liu, J. Zhang, Z. Feng, C. Li, Z. Li, *Chin. J. Catal.* **2016**, *37*, 349.

[209] Y. Zhang, X. Xiong, Y. Han, X. Zhang, F. Shen, S. Deng, H. Xiao, X. Yang, G. Yang, H. Peng, *Chemosphere* **2012**, *88*, 145.

[210] S. Ansaloni, M. Castellino, A. Massa, S. Hern, N. Russo, D. Fino, *Electrochim. Acta* **2018**, *273*, 53.

[211] H. Habazaki, Y. Hayashi, H. Konno, *Electrochim. Acta* **2002**, *47*, 4181.

[212] M. Q. Yang, M. Gao, M. Hong, G. W. Ho, *Adv. Mater.* **2018**, *30*, 1802894.

[213] Y. Ye, Y. Feng, H. Bruning, D. Yntema, H. H. M. Rijnaarts, *Appl. Catal., B* **2018**, *220*, 171.

[214] Q. Zhu, J. Qian, H. Pan, L. Tu, X. Zhou, *Nanotechnology* **2011**, *22*, 395703.

[215] Y. Zhao, F. Pan, H. Li, D. Zhao, L. Liu, G. Q. Xu, W. Chen, *J. Phys. Chem. C* **2013**, *117*, 21718.

[216] Y. Wang, W. Zhang, Z. Wang, Y. Cao, J. Feng, Z. Wang, Y. Ma, *Chin. J. Catal.* **2018**, *39*, 1500.

[217] Z. Ding, G. Q. Lu, P. F. Greenfield, *J. Phys. Chem. B* **2000**, *104*, 4815.

[218] V. Vapor, P. Hydrolysis, M. Blue, *J. Am. Ceram. Soc.* **2012**, *6*, 1927.

[219] W. Zhou, L. Gai, P. Hu, J. Cui, X. Liu, D. Wang, G. Li, H. Jiang, D. Liu, H. Liu, J. Wang, *CrystEngComm* **2011**, *13*, 6643.

[220] Y. Cao, X. Li, Z. Bian, A. Fuhr, D. Zhang, J. Zhu, *Appl. Catal., B* **2016**, *180*, 551.

[221] Y. Lu, J. Zhang, F. Wang, X. Chen, Z. Feng, C. Li, *ACS Appl. Energy Mater.* **2018**, *1*, 2067.

[222] D. Zeng, K. Yang, C. Yu, F. Chen, X. Li, Z. Wu, H. Liu, *Appl. Catal., B* **2018**, *237*, 449.

[223] L. N. Song, L. Chen, J. He, P. Chen, H. K. Zeng, C. T. Au, S. F. Yin, *Chem. Commun.* **2017**, *53*, 6480.

[224] E. Luévano-Hipólito, A. M. D. L. Cruz, Q. L. Yu, H. J. H. Brouwers, *Appl. Catal., A* **2013**, *468*, 322.

[225] B. Baral, K. H. Reddy, K. M. Parida, *J. Colloid Interface Sci.* **2019**, *554*, 278.

[226] M. Choi, J. Lim, W. Choi, W. Kim, K. Yong, *ACS Appl. Mater.* atsuo, T. Tsubota, T. Ohno, *Catal. Commun.* **2011**, *12*, 341.

[227] N. Murakami, T. Matsuo, T. Tsubota, T. Ohno, *Catal. Commun.* **2011**, *12*, 341.

[228] A. S. Niraj Kumar, K. Rajendran, R. Rameshbabu, J. Ragupathi, H. A. Therese, T. Maiyalagana, *RSC Adv.* **2017**, *7*, 25041.

[229] S. Das, A. Samanta, S. Jana, *ACS Sustainable Chem. Eng.* **2017**, *5*, 9086.

[230] Y. Guo, X. Yang, F. Ma, K. Li, L. Xu, X. Yuan, Y. Guo, *Appl. Surf. Sci.* **2010**, *256*, 2215.

[231] N. J. Cherepy, D. B. Liston, J. A. Lovejoy, H. Deng, J. Z. Zhang, *J. Phys. Chem. B* **1998**, *102*, 770.

[232] J. B. Fei, Y. Cui, X. H. Yan, W. Qi, Y. Yang, K. W. Wang, Q. He, J. B. Li, *Adv. Mater.* **2008**, *20*, 452.

[233] Y. Bai, Y. Zhou, J. Zhang, X. Chen, Y. Zhang, J. Liu, J. Wang, F. Wang, C. Chen, C. Li, R. Li, C. Li, *ACS Catal.* **2019**, *9*, 3242.

[234] a) P. P. N. Shanmugam, *Appl. Phys. A* **2017**, *123*, 586; b) H. Zhang, J. F. Banfield, *J. Mater. Chem.* **1998**, *8*, 2073.

[235] J. Banfield, *J. Mater. Chem.* **1998**, *8*, 2073.

[236] J. M. Macak, M. Zlamal, J. Krysa, P. Schmuki, *Small* **2007**, *3*, 300.

[237] D. O. Scanlon, C. W. Dunnill, J. Buckeridge, S. A. Shevlin, A. J. Logsdail, S. M. Woodley, C. R. A. Catlow, M. J. Powell, R. G. Palgrave, I. P. Parkin, G. W. Watson, T. W. Keal, P. Sherwood, A. Walsh, A. A. Sokol, *Nat. Mater.* **2013**, *12*, 798.

[238] D. C. Hurum, A. G. Agrios, K. A. Gray, T. Rajh, M. C. Thurnauer, *J. Phys. Chem. B* **2003**, *107*, 4545.

[239] T. Ohno, K. Tokieda, S. Higashida, M. Matsumura, *Appl. Catal., A* **2003**, *244*, 383.

[240] R. I. Bickley, T. Gonzalez-carreno, J. S. Lee, L. Palmisano, R. J. D. Tilleyd, *J. Solid State Chem.* **1991**, *92*, 178.

[241] E. Kordouli, K. Bourikas, A. Lycourghiotis, C. Kordulis, *Catal. Today* **2015**, *252*, 128.

[242] R. Su, R. Bechstein, L. Sø, R. T. Vang, M. Sillassen, A. Palmqvist, F. Besenbacher, *J. Phys. Chem. C* **2011**, *115*, 24287.

[243] R. Buonsanti, V. Grillo, E. Carlino, C. Giannini, T. Kipp, R. Cingolani, P. D. Cozzoli, *J. Am. Chem. Soc.* **2008**, *130*, 11223.

[244] H. Lin, L. Li, M. Zhao, X. Huang, X. Chen, G. Li, R. Yu, *J. Am. Chem. Soc.* **2012**, *134*, 8328.

[245] S.-P. Junctions, P. Activity, J. Zhang, Q. Xu, Z. Feng, M. Li, C. Li, *Angew. Chem., Int. Ed.* **2008**, *47*, 1766.

[246] I. M. Szilágyi, J. Madarász, G. Pokol, P. Király, G. Tárkányi, S. Saukko, J. Mizsei, A. L. Tóth, A. Szabó, K. Varga-Josepovits, *Chem. Mater.* **2008**, *20*, 4116.

[247] D. B. Hernandez-uresti, D. Sánchez-martínez, A. M.-d. Cruz, *Ceram. Int.* **2014**, *40*, 4767.

**ADVANCED
SCIENCE NEWS**

www.advancedsciencenews.com

**ADVANCED
MATERIALS**

www.advmat.de

[248] M. R. Saber, G. Khabiri, A. A. Maarouf, M. Ulbricht, A. S. G. Khalil, *RSC Adv.* **2018**, *8*, 26364.

[249] C. Yu, G. Li, S. Kumar, K. Yang, R. Jin, *Adv. Mater.* **2014**, *26*, 892.

[250] J. Zhang, M. Zhang, R.-Q. Sun, X. Wang, *Angew. Chem., Int. Ed.* **2012**, *51*, 10145.

[251] X. Yang, F. Qian, G. Zou, M. Li, J. Lu, Y. Li, M. Bao, *Appl. Catal., B* **2016**, *193*, 22.

[252] Q. Liang, Z. Li, Y. Bai, Z.-H. Huang, F. Kang, Q.-H. Yang, *Small* **2017**, *13*, 1603182.

[253] R. Daghrir, P. Drogui, D. Robert, *J. Photochem. Photobiol., A* **2012**, *238*, 41.

[254] W. H. Leng, W. C. Zhu, J. Ni, Z. Zhang, J. Q. Zhang, C. N. Cao, *Appl. Catal., A* **2006**, *300*, 24.

[255] D. Jiang, H. Zhao, S. Zhang, R. John, *J. Photochem. Photobiol., A* **2006**, *177*, 253.

[256] D. Jiang, S. Zhang, H. Zhao, *Environ. Sci. Technol.* **2007**, *41*, 303.

[257] S. Garcia-Segura, S. Dosta, J. M. Guilemany, E. Brillas, *Appl. Catal., B* **2013**, *132-133*, 142.

[258] T. A. Egerton, M. Janus, A. W. Morawski, *Chemosphere* **2006**, *63*, 1203.

[259] Y.-F. Tu, S.-y. Huang, J.-p. Sang, X.-w. Zou, *J. Alloys Compd.* **2009**, *482*, 382.

[260] K. E. O'Shea, D. D. Dionysiou, *J. Phys. Chem. Lett.* **2012**, *3*, 2112.

[261] X. Duan, H. Sun, S. Wang, *Acc. Chem. Res.* **2018**, *51*, 678.

[262] W. H. Glaze, J. W. Kang, D. H. Chapin, *Ozone: Sci. Eng.* **1987**, *9*, 335.

[263] W. Zhang, Z. Yang, X. Wang, Y. Zhang, X. Wen, S. Yang, *Catal. Commun.* **2006**, *7*, 408.

[264] Y. Dong, H. Yang, K. He, S. Song, A. Zhang, *Appl. Catal., B* **2009**, *85*, 155.

[265] E. Saputra, S. Muhammad, H. Sun, H. M. Ang, M. O. Tade, S. Wang, *Environ. Sci. Technol.* **2013**, *47*, 5882.

[266] E. Saputra, S. Muhammad, H. Sun, H. M. Ang, M. O. Tadé, S. Wang, *Appl. Catal., B* **2013**, *142-143*, 729.

[267] Y. Wang, H. Sun, H. M. Ang, M. O. Tadé, S. Wang, *Appl. Catal., B* **2015**, *164*, 159.

[268] G. Cao, L. Su, X. Zhang, H. Li, *Mater. Res. Bull.* **2010**, *45*, 425.

[269] A. K. Sinha, M. Pradhan, T. Pal, *J. Phys. Chem. C* **2013**, *117*, 23976.

[270] P.-Y. Kuang, M.-H. Liang, W.-Y. Kong, Z.-Q. Liu, Y.-P. Guo, H.-J. Wang, N. Li, Y.-Z. Su, S. Chen, *New J. Chem.* **2015**, *39*, 2497.

[271] B. Zhang, G. Cheng, W. Ye, X. Zheng, H. Liu, M. Sun, L. Yu, Y. Zheng, X. Cheng, *Dalton Trans.* **2016**, *45*, 18851.